Shallow and buoyant lithospheric subduction:

causes and implications from thermo-chemical numerical
modeling

Jeroen van Hunen

Shallow and buoyant lithospheric subduction:

causes and implications from thermo-chemical numerical modeling

Ondiepe subductie van gravitationeel stabiele lithosfeer:

oorzaken en implicaties in een thermo-chemische numerieke modelstudie

(met een samenvatting in het Nederlands)

PROEFSCHRIFT

TER VERKRIJGING VAN DE GRAAD VAN DOCTOR
AAN DE UNIVERSITEIT UTRECHT
OP GEZAG VAN DE RECTOR MAGNIFICUS, PROF. DR. W.H. GISPEN,
INGEVOLGE HET BESLUIT VAN HET COLLEGE VOOR PROMOTIES
IN HET OPENBAAR TE VERDEDIGEN
OP MAANDAG 26 NOVEMBER 2001 DES MIDDAGS TE 16:15 UUR

DOOR

Jeroen van Hunen

Geboren op 27 mei 1971, te Rotterdam

Vraag niet: 'Wat zal de dag van morgen brengen?'
Geniet het heden met zijn zonneglans,
zijn jonge liefde en zijn blijde dans!

Nu 's levens bloei nog lang niet zal vergrijzen,
nu is het tijd voor pret en darteling,
voor minnekozen in de schemering.

Horatius, Oden 1.9, regel 13-18
vertaling: A. Rutgers van der Loeff

Voor mijn ouders

Contents

Chapter 1

Introduction

During its 4.6 billion year history, the Earth has shown continuous activity to loose its heat. The heat budget of the Earth determines the vigor of mantle convection, the amount of mantle plume activity, and the type of the tectonic regime. The main heat sources in this system are primordial heat, which is the heat that the Earth obtained during its formation in the early solar system, and heat from radioactive decay. Today, the total global surface heat flow is 4.4×10^{13} W, of which 15% is attributed to radiogenic heat production and 85% to heat loss from the mantle and core (Malamud and Turcotte, 1999). About 60% of the mantle heat is lost by plate tectonics, and the rest by heating the base of the lithospheric plates, predominantly as the result of plume activity. Plate tectonics is therefore regarded as an effective and essential mechanism that contributes significantly in cooling the Earth at present-day. In this mechanism, oceanic plates are formed at the mid-ocean ridge (MOR), spread laterally, and eventually subduct again into the mantle at the trench or subduction zone. These oceanic plates are compositionally layered due to pressure release partial melting and melt segregation at the MOR. This melt forms the basaltic oceanic crust, which today is about 7 km thick. The residual matrix of the melting process forms a harzburgitic layer below the crust.

Since the inertial forces are negligible, the sum of forces that act on the plates must be zero. In general, two types of forces are believed to drive plate tectonics internally: ridge push and slab pull (Vlaar, 1975; Wortel et al., 1991). Ridge push originates from the cooling and contraction of the oceanic lithosphere with age, and is calculated by integrating the resulting horizontal pressure gradient over the plate. Slab pull is the down-dip component of the gravitational body force acting on the dense subducted slab (McKenzie, 1969). The slab pull is estimated to be an order of magnitude larger than the ridge push for most subducting oceanic plates (Forsyth and Uyeda, 1975). Resistance against plate motion originates from friction at the plate boundaries, mantle drag, internal resistance against deformation, and compositional buoyancy within the slab. The friction between plates becomes evident through shallow earthquakes. Internal deformation by bending and unbending of the plate at the subduction zone dissipates a considerable amount of the available potential energy (Conrad and Hager, 1999a). Both the basaltic crust and the un-

11

derlying harzburgitic layer are less dense than undepleted mantle material under the same circumstances. At depth, the resulting compositional buoyancy is removed by the basalt-to-eclogite phase transition, since the buoyancy terms from the eclogite and harzburgite layer more or less compensate each other. Slow kinetics of this transition may increase the total compositional buoyancy significantly (Hacker, 1996). Also the major mantle phase transitions at 400 and 670 km depth significantly influence the slab geometry. Especially the 670-km transition deflects most slabs towards the horizontal and (temporarily) keeps some slabs from penetrating into the lower mantle, as shown by numerical model studies (Christensen and Yuen, 1985), and tomographic images (van der Hilst, 1995; Bijwaard et al., 1998).

The relation between mantle convection and plate tectonics has been subject to debate. Do plates drive convection? Or does convection contribute significantly to the plate motion? Or are plates and underlying mantle almost decoupled? In a common view, plates and slabs are regarded as the upper and downgoing limbs of a convection cell. But the large variations in the size of the plates and intricate geometry of the plate boundaries contradict such simple picture. Also features like MOR-subduction do not fit into such model. Davies (1998) concludes from MOR topography studies that the mantle under the plates is relatively passive. Furthermore, the presence of a pronounced weak asthenosphere (Sigmundsson, 1991; Fjeldskaar, 1994) allows for a weak coupling between plates and underlying mantle. All together, some coupling between plate and mantle is likely to exist, but plates seem to be able to move rather independently from the underlying mantle.

1.1   Subduction angle of lithospheric slabs

Since the slab pull acts vertically downward, we could expect all slabs to end up hanging vertically in the mantle. This, however, is not the case. All slabs have dip angles smaller than 90 degrees at any depth (Jarrard, 1986). One cause is the internal resistance against deformation which will prohibit the slabs from rapidly adopting a large dip angle, but additional factors are necessary to explain the large variation in slab geometries: some slabs seem to descend straight into the lower mantle, while others are, at least temporarily, flattened in the transition zone (van der Hilst, 1995). An even more puzzling phenomenon is the shallow flattening of some parts of the Nazca slab, right below the depth of the overriding continent of South-America at about 100 km depth, while other parts of this slab subduct more steeply (Barazangi and Isacks, 1976). Several correlations with subduction parameters are suggested to explain the dip angle of a subducting slab. Younger slabs seem, in general, to dip at a smaller angle (Vlaar and Wortel, 1976; Wortel and Vlaar, 1978). Very low-angle subduction does, indeed, not occur for old oceanic slabs, but dip angles less than 45 degrees are observed for slabs of almost any age (Jarrard, 1986). Absolute motion of the overlying plate towards the trench is suggested to lower the subduction dip angle (Cross and Pilger, 1978). Trench roll-back is the oceanward motion of the trench, caused by an old and gravitationally unstable subducting oceanic plate. This mechanism causes a lowered dip angle in case of old and dense oceanic plates and determines the ability of the slab to penetrate the 670-km phase transition (van der Hilst

and Seno, 1993; Griffiths et al., 1995; Christensen, 1996; Olbertz et al., 1997).

One explanation for shallow low-angle subduction of young slabs is active motion of the overriding plate towards the subducting plate by some external force, or 'lithospheric doubling' (Vlaar, 1983). This process may provide a means to subduct buoyant material and may result in shallow subduction with a very low to zero subduction angle, as observed today below parts of the Andes in South-America. A driving force for the westward motion of South-America with respect to the hotspot reference frame (Jarrard, 1986; Gripp and Gordon, 1990; Olbertz, 1997) could be the ridge push of the Atlantic oceanic lithosphere, although stress calculations suggest that the resulting compression is too low to sustain the Andes (Meijer et al., 1997). A deep thermal anomaly could form an additional mechanism to explain the South-American stress regime and drift (Zhong and Gurnis, 1995). Although both trench roll-back and lithospheric doubling involve a trenchward motion and a decreasing dip angle, their resulting stress regimes are opposite. Roll-back results in an extensional regime, which may give rise to back-arc spreading, as observed in South-East Asia, while lithospheric doubling produces compression, with the building of associated mountains, such as the Andes. Also subducting aseismic ridges, oceanic plateaus or seamount chains are proposed to cause lower angle to flat subduction (Cross and Pilger, 1978; McGeary et al., 1985; Gutscher et al., 2000b). Their greater than normal crustal thickness and proportionally thickened harzburgitic layer locally remove the gravitational instability of the slab and therefore reduce the dip angle. This mechanism implicitly assumes the occurrence of metastable basalt in the eclogite stability field, since the equilibrium transition from basalt to the much denser eclogite occurs at 60-70 km depth and would remove the net compositional buoyancy of the slab, regardless of its crustal thickness. Indeed, this metastability can be significant in cold and dry areas (Rubie, 1990; Hacker, 1996; Austrheim, 1998). Other proposed mechanisms for shallow flat subduction originate from several kinds of cohesion forces. Hydrostatic suction (Jischke, 1975) and non-lithostatic pressure forces (Stevenson and Turner, 1977; Tovish et al., 1978) tend to pull the subducting plate towards the overriding plate. Also friction between the converging plates could form a torque that tends to keep the two plates attached.

Large-scale flat subduction (with zero dip angle) has been proposed during the Laramide orogeny, about 65 Ma ago below western North-America and could have been responsible for the formation of the Rocky Mountains (Dickinson and Snyder, 1978; Bird, 1988, 1998). Subduction is usually associated with arc volcanism as a result of slab dehydration. The part closest to the trench, the so called volcanic front, is consistently located at about 110 km above the subducting slab (Tatsumi and Eggins, 1995). As a result of a dip angle decrease, arc volcanism tends to migrate inland, since the slab reaches the dehydration depth farther away from the trench. A migrating pattern of magmatism suggests that flat subduction started around 70 Ma, reached its maximum extent up to 1500 km inland at around 60 Ma, after which the slab steepened again (Spencer, 1996). As North America moved westward with approximately 5 cm/yr during this period (Engebretson et al., 1985), lithospheric doubling is invoked as the responsible mechanism behind this feature.

The most well-known and best-studied examples of modern flat subduction are below Peru and Central Chile in South America. Slab locations are clearly marked by earthquake
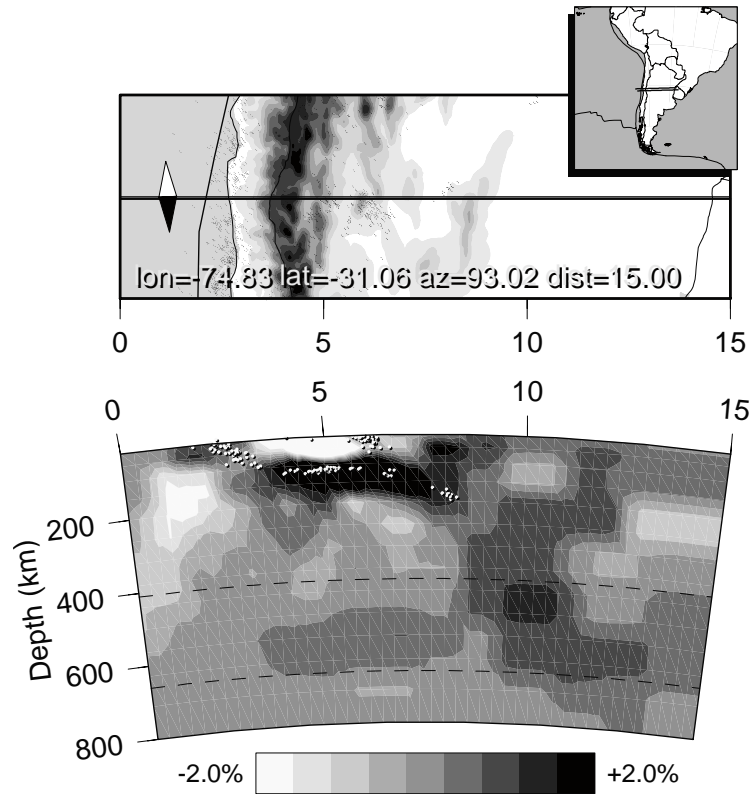
Figure 1.1: Tomography and earthquake hypocenter results of the flat slab segment below Central Chile from the non-linear P-wave tomography inversion by Bijwaard and Spakman (2000).

hypocenters (Barazangi and Isacks, 1976; Wortel and Vlaar, 1978; Hasegawa and Sacks, 1981), by the absence of arc volcanism (McGeary et al., 1985) and by tomographic images (Gutscher et al., 2000b). In Figure 1.1, tomographic images and earthquake hypocenter locations from the P-wave tomography model in (Bijwaard and Spakman, 2000) show the presence of shallow horizontal subduction below Central Chile. The tomography model shows a similar slab geometry below Central and South Peru. The underlying plate seems to be forced to subduct as deep as the mechanical root of the continent, at about 100 km depth. At that depth, subduction can continue horizontally to form a flat slab segment. Several mechanisms have been proposed to explain this slab geometry. A westward movement of the overlying South-American continent (Gordon and Jurdy, 1986; Gripp and Gordon, 1990) would overthrust the subducting plate. Also the subduction of parts of the Nazca plate with an thickened crust (The Inca Plateau, the Nazca ridge, and

the Juan Fernandez seamount chain) has been proposed to be responsible for the local flattening of the subducting slab (Cross and Pilger, 1978; McGeary et al., 1985; Gutscher et al., 1999a,b, 2000b).

Other areas of flat subduction are reported, mostly based on the location of the Wadati-Benioff zone. Gutscher et al. (2000b) even state that 10% of the modern subduction zones show flat subduction. Unfortunately, examination of all these regions is usually more difficult due to the tectonic complexity of the area or lack of seismicity data. Low-angle subduction of the Pacific oceanic plate occurs below the underthrusted Yacutat terrane at South-Alaska (Brocher et al., 1994). This terrane may have accreted to the subducting plate to result in a thickened crust, and the associated increased compositional buoyancy might postpone steep subduction. At Cascadia and Central Mexico, the young Juan de Fuca plate and a very young segment of the Cocos plate subduct at a very low angle, respectively (Crosson and Owens, 1987; Defant and Drummond, 1993; Suarez et al., 1990). In these zones, the age of the slabs seems to have been dominating the slab dip. At Columbia, the Caribbean oceanic plateau subducts very slowly at a low-angle from the north below the South-American continent, while simultaneously, the NW part of South-America shows a northward movement (van der Hilst and Mann, 1994). At the Nankai Trough, near South Honshu in SW Japan, the Philippine Sea plate subducts horizontally below the Eurasian plate (Sacks, 1983). The Philippine Sea plate is relatively young, but also the thickened crust of the Palau-Kyushu Ridge and Izu Bonin Arc could have caused the shallow flat subduction (Hirahara, 1981; Gutscher and Lallemand, 1999). Finally, the thickened crust of the Euripik Rise is suggested to be responsible for the observed 35-Ma-old low-angle subduction below New Guinea (McGeary et al., 1985).

Although some oceanic plates 'voluntarily' subduct at their arrival at the trench, the observations above suggest that other plates are (partly) too buoyant to sink into the mantle, because the compositional buoyancy of the crust and the harzburgitic layer exceeds the negative thermal buoyancy. Either the slab is very young and the negative thermal buoyancy is still small, or the crust and harzburgite layer are locally thickened, which also increases the gravitational stability of the plate. The only reason that oceanic crust is recycled back into the mantle is its attachment to the much denser underlying mantle lithosphere. It is, in fact, remarkable that only a few parts of the oceanic crust older than 200 Ma are preserved. Several observations, however, suggest that the oceanic crust is not always dragged along with the slab to the deep mantle, and that crustal recycling is a complicated and partly unsolved subject of research. The presence of ophiolites, for example, indicate that the subduction of oceanic crust is not always smooth, most likely because of the crustal buoyancy (Vlaar and Cloetingh, 1984). Subduction of young lithosphere (Defant and Drummond, 1990) or flat subduction (Gutscher et al., 2000a) may give rise to melting of the oceanic crust and associated adakatic arc volcanism, which is clearly distinct from normal arc volcanism. Between the 670-km transition and 800 km depth, the oceanic crust is again buoyant, and delamination at this depth is proposed (Anderson, 1979; Irifune and Ringwood, 1993; Ringwood, 1994; van Keken et al., 1996; Karato, 1997). This would confine the region of crustal recycling to the upper mantle. Kimberlites or diamond pipes indicate explosive eruptions of a mix of harzburgite, lherzolite, eclogite, and incompatible elements and volatiles, which suggest an oceanic crustal origin

(Vlaar, 1983). The source of the erupted material must be deep and partly much cooler
($< 600^{o}$C) than the ambient mantle temperature at that depth. Since kimberlites are lo-
cated in continental platforms and cratons, and not exclusively near (ancient) subduction
zones, a possible explanation for their occurrence could be horizontal subduction, shal-
lowly below the continent. It provides a mechanism to transport hydrated oceanic crust
under low temperature conditions to the intracontinental source regions of kimberlites.

1.2   Plate tectonics in a younger Earth

The different thermal state of the early Earth gave rise to ideas about a different tectonic
regime. The mantle potential temperature was higher than today, maybe even a few hun-
dreds of degrees. This has been subject to considerable debate (see Vlaar et al., 1994). A
larger volume of partially melted mantle material resulted in a thicker-than-today oceanic
crust (30-50 km)(Vlaar, 1986b). Such an oceanic lithosphere would have been positively
buoyant, regardless of its age, and would have only become gravitationally unstable by
eclogitisation of the crust. Furthermore, the higher mantle temperature would have re-
sulted in lower overall viscosities. These considerations have questioned the presence of
plate tectonics in the Archean, the earliest period in the Earth's history. Some studies are
suggesting geological observations of modern style plate tectonics since the early Protero-
zoic or even the late Archean by indicating that the Earth was not much hotter than today
(de Wit, 1998). Kusky et al. (2001) give geological evidence for a 2.5 Ga old plate tectonic
setting. Others reject this idea, and argue that the geologic observations of the Archean
magmatic and tectonic development would have no modern analogue (Hamilton, 1998).
In a hotter Earth, the base of the thicker oceanic crust was probably ductile, so that the
mechanical coherency with the underlying mantle lithosphere may not have been present
(Hoffman and Ranalli, 1988; Vlaar and van den Berg, 1991). The buoyant crust could
have shown internal convection and delamination from the underlying mantle part of the
lithosphere. This would allow only the mantle part of the lithosphere to 'subduct' and
would give rise to a different tectonic mechanism. Even if oceanic lower crust was strong
enough to create a mechanical coherent plate, these plates would be positively buoyant for
all ages, and plate tectonics may not be able to effectively cool the Earth (Vlaar, 1986a;
Vlaar and van den Berg, 1991; Davies, 1992). Therefore, alternative or additional mecha-
nisms are proposed to have been active. Eclogitisation, delamination and re-melting of the
lower part of the oceanic crust could have been an effective mechanism to cool the early
Earth, and may have resulted in small-scale layered convection (Hoffman and Ranalli,
1988; Vlaar et al., 1994). The mechanism of lithospheric doubling has been suggested
to enable subduction of buoyant plates in a Proterozoic Earth from the time that plates
have reached internal mechanical coherency (Vlaar, 1986a). To explain the geochemical
signatures of the felsic rocks of the tonalite-trondhjemite-granodiorite (TTG) series, flat
subduction or underthrusting of an Archean oceanic lithosphere has also been suggested
as a possible mechanism (Smithies, 2000).

    A still unanswered question is how far back in time the modern-style subduction pro-
cess was already active. Did plate tectonics suddenly appear? If so, at what time became

subduction initiation first feasible, and how did the Earth look like just prior to this event? The lower viscosities in the hotter Earth might have decreased energy dissipation during the plate tectonic process. Subduction conditions are most likely to depend on the eclogitisation rate, which partly solves the above-mentioned buoyancy problem. Another limitation may come from the ridigity of the plates: subduction requires a plate which is strong enough to pass stresses from slab pull and ridge push forces. Crustal material is weaker than mantle material, so a thick crust weakens the plate. Alternatively, the Earth could have slowly changed from some previous regime to the modern plate tectonic regime. Lithospheric doubling could have been the transient mechanism to enable subduction of plates, which already show some plate-like behavior, but are still to weak or buoyant to actively subduct under their own weight.

1.3   Numerical modeling

Since we cannot directly measure physical parameters inside the Earth and observe the ongoing processes, we have to rely on indirect measurements, like geological observations, geochemical signatures from volcanism, and geophysical tools, such as tomography. These observations provide information about one moment in time, but do not give much insight into the dynamical processes. A numerical model is a useful tool to simulate processes to obtain dynamical information. Here, we use a finite element model to study the plate tectonic mechanism, including the motion of the mantle and the coupling between plates and mantle, and the time-dependent distribution of materials. The common name for such model is thermo-chemical convection model. It deals with (a part of) the Earth as a viscous fluid, in which the rheological properties of mantle and crustal materials are translated to an effective viscosity. It solves for the velocity, distribution, and thermal state of the material in the Earth, and uses the information about physical properties, as provided by laboratory measurements, analytical calculations or previous numerical calculations as input. The material flow is driven partly by boundary conditions and partly internally by thermal and compositional density variations. Such model provides a means to study the dynamical aspects of processes inside the Earth. The simulation is used to determine possible links between physical processes and the observed geological, geochemical, and geophysical signatures, and parameter studies are performed to determine the sensitivity of the model response to changes in the physical parameters.

1.4   Outline of this thesis

In this thesis, the main focus is on the viability of several mechanisms to explain the subduction of buoyant lithosphere and shallow flat subduction, and on the determination of the required physical circumstances. Chapter 2 deals with the governing equations of the subduction process. It describes the applied rheology and the incorporation of the mantle and crustal phase transitions. Furthermore, the applied boundary conditions are discussed. In Chapter 3, the numerical methods are explained: the time integration and

the solution methods for the governing equations are given. In Chapter 4, the viability of flat subduction of young oceanic lithosphere below a trenchward moving overriding continent is investigated. The effects of varying interplate coupling, crustal and mantle strength, and overriding plate velocity on the subduction process are determined. Chapter 5 determines the role of the major mantle phase transitions at 400 and 670 km depth in the process of shallow flat subduction. In particular, the effect of latent heat production is investigated. In Chapter 6, the impact of an oceanic plateau on flat subduction is discussed. In Chapter 7, the numerical model is applied in a parameter study to investigate the relative importance of some proposed mechanisms which may apply to the flat slab region in the Andean subduction zone below Peru. In Chapter 8, results are presented of a modeling study to the effects on the plate tectonic mechanism of changing thermal circumstances by secular cooling of the Earth during its thermal evolution.

Chapter 2

Model formulation

2.1 Buoyancy forces in the model

In general, one of the driving forces in a thermo-chemical convection model is buoyancy as a result of density variations. In the presented model, these density variations have three different origins: thermal, compositional and due to phase transitions. These are described by the following equation of state:

$$\Delta\rho(T, C, \Gamma_k) = \rho_0 \left[\sum_k \frac{\delta\rho_k}{\rho_0}\Gamma_k + \frac{\Delta\rho_c}{\rho_0} - \alpha(T - T_s) \right] \qquad (2.1)$$

Symbols and values are given in Table 2.1. The uniform reference density ρ_0 is in line with the Boussinesq assumption given in Section 2.3. It applies to undepleted upper mantle material (lherzolite) at the temperature $T_s = 273$ K. Each of the k phase transitions transforms descending mantle material into a denser phase, described by the density increase $\delta\rho_k$. Thermal expansion causes the density of the material to decrease with increasing temperature. Finally, the model distinguishes between three different compositions (or materials): lherzolite (undepleted mantle material), harzburgite (depleted mantle material) and oceanic crust, each with their own intrinsic density.

2.2 Rheological model: data and implementation

2.2.1 Mantle rheology

The strength of mantle material is, to a large extent, controlled by the rheological properties of olivine. Its basic deformation behavior is known from high pressure and temperature laboratory studies, and results have been translated into flow laws. A general simplified flow law for a single solid-state creep process in the mantle is (Karato and Wu,

1993)

$$\dot{\epsilon} = A\tau^n d^{-m} \exp\left[-\frac{E^* + pV^*}{RT}\right] \tag{2.2}$$

Recent summaries of experimental data on olivine creep parameters A, n, m, E^* and V^* are given in (Ranalli, 1998, Table 1) and (Drury and Fitz Gerald, 1998, Table 11.2) for diffusion and dislocation creep under wet and dry conditions. These material properties are determined under laboratory conditions and need to be extrapolated to much lower deformation rates. Derivation of the mantle strength further requires the temperature and hydration conditions in the mantle. For the determination of the dislocation and diffusion creep strength, we further need information about the strainrate and grain size, respectively. For a single deformation mechanism i, a suitable definition of the viscosity is $\eta_i = \tau/\dot{\epsilon}$. Eq. 2.2 is then rewritten to

$$\eta_i = A^{-1/n}\dot{\epsilon}^{(1-n)/n}d^{m/n}\exp\left[\frac{E^* + pV^*}{nRT}\right] \tag{2.3}$$

A composite rheology model describes the effective viscosity η_{eff} of a combination of flow laws (van den Berg et al., 1993)

$$\eta_{\text{eff}} = \left(\sum_i (\eta_i)^{-1}\right)^{-1} \tag{2.4}$$

Figure 2.1 shows the vertical effective upper mantle viscosity profile $\eta_{\text{eff}}(z)$ for the parameter set from (Karato and Wu, 1993) (using $\dot{\epsilon} = 10^{-15}\text{s}^{-1}$, $\mu = 80$ GPa, $b = 0.5$ nm, $d = 1$ mm, and values from their Table 1) for both wet and dry mantle conditions. These profiles are calculated for a mantle temperature profile of a 40-Ma old oceanic lithosphere, which cooled from an adiabatic profile with a 1300^oC potential temperature.

Postglacial rebound models and geoid inversions are used to invert surface observations directly into mantle viscosity. These methods do not require information about the temperature field, degree of hydration, or other physical conditions, and provide an independent tool to determine the effective mantle viscosity. They are based on data from relative sea level changes due to glacial unloading since the last Ice Age. In general, the resolution of the method allows for a rheological description in a limited numbers of radially stratified layers (three to five). Based on rebound data from Northwestern Europe, Lambeck and Johnston (1998) and Lambeck et al. (1998) suggest an upper and lower mantle viscosity $\eta = 3.6 \pm 1 \times 10^{20}$ Pa s and $4 \times 10^{21} < \eta < 3 \times 10^{22}$ Pa s, respectively. These ranges are given in Figure 2.1 as grey areas. The viscosity contrast between upper and lower mantle appears to be a robust feature.

Geoid anomalies depict both density deviations from a radially layered Earth and boundary deformation induced by flow in the Earth's interior. This method provides only relative viscosity profiles and combinations with other observations are necessary to determine the absolute values of mantle viscosity. Combination with true polar wander data suggests an upper mantle viscosity, which is slightly over 10^{20} Pa s and a lower mantle viscosity of 1-5 $\times 10^{21}$ Pa s (Vermeersen et al., 1998)

For the model calculations in this thesis, a set of rheological parameters is modified from an original set of creep parameters for dry conditions in (Karato and Wu, 1993), and applied to the whole mantle. As activation volumes are relatively poorly constrained, the dislocation creep value is replaced by the one from (Karato and Rubie, 1997). The one for diffusion creep is lowered to obtain a lower mantle viscosity in agreement with (Lambeck et al., 1998). Values of the prefactor A from Equation 2.2 for diffusion and dislocation creep are both modified from the Karato-and-Wu values by an equal amount to obtain an effective upper mantle viscosity in agreement with post-glacial rebound results. Figure 2.1 shows a vertical effective oceanic mantle viscosity profile from a typical model calculation. In addition, a profile is shown with the same rheological parameters, but with a constant strainrate $\dot{\epsilon} = 10^{-15}$ s^{-1}. The latter profile can be compared to the wet and dry profiles from Karato and Wu, also shown.

2.2.2   Rheology of the oceanic crust

The oceanic crust consists of mafic rocks with grain sizes ranging from very small (basalt) to mm-size (gabbro). Diabase or dolerite are often used as nonspecific names. Creep properties of this material are not as well studied as those of olivine. Shelton and Tullis (1981), Caristan (1982) and Mackwell et al. (1998) report dislocation creep flow parameters for diabase, based on the same general Arrhenius parameterization as for mantle material (Eq. 2.2). All studied rock samples are partly or even completely dried, as steady state experimental tests with hydrous samples are difficult to accomplish due to possible partial melting and dehydration effects (Mackwell et al., 1998). In this thesis, the creep parameters from the Maryland diabase samples from (Shelton and Tullis, 1981) are used to define the relationship between crustal strength and ambient temperature and strainrate. As also these samples were partly dried, their strength can be regarded as an upper limit of the oceanic crustal strength, and the prefactor A is adapted to lower the effective viscosity of the crust. Only dislocation creep flow laws are reported for diabase. Therefore, crustal diffusion creep is not considered in the model calculations. No activation volume data are available for crustal material. Therefore, a modest value for $V^* = 10$ cm^3/mol is applied in the models.

During the subduction process, the oceanic crust transforms into eclogite (see also section 2.4.2). The strength of eclogite is even less well determined. Eclogite mainly consists of garnet and omphacite (Hacker, 1996). The garnets have a significantly larger viscosity than mantle material (Karato, 1996). Using theoretical calculations of flow laws for polyphase rocks from flow laws of their constituent phases, Ji and Zhao (1994) predict the strength of eclogite from flow laws for garnet and diopside (as a rheological equivalent for omphacite). They conclude that eclogite is considerably stronger (about one order of magnitude) than mantle material under the same circumstances. Stöckhert and Renner (1998), however, argue that diopside is much stronger than omphacite and suggest the strength of jadeite as a better alternative. As they find that jadeite can be even weaker than quartz for temperatures over 600^oC, they conclude that eclogite must be much weaker than previously thought. As a compromise, the strength of eclogite is taken to be equal to that of diabase in all model calculations.

2.2.3 Strength of the lithosphere and slabs

Application of a composite rheology of solely diffusion and dislocation creep leads to an effective viscosity of the cold areas of the lithosphere and slabs that is much larger than suggested by Kohlstedt et al. (1995). Near the surface, brittle failure of the lithospheric rocks is the dominant stress limiting mechanism. In the transition from brittle to plastic deformation, semi-brittle deformation is recognized (Kohlstedt et al., 1995; Bos and Spiers, 2001). At larger depth, low-temperature plasticity or Peierl's mechanism is proposed as stress-limiting deformation mechanism (Kameyama et al., 1999; Karato et al., 2001). In the numerical models of this thesis, the strength of the cold interiors of the lithosphere and slabs are limited by either an upper limit of the effective viscosity η_{max} or by a stress-limiting mechanism, added to the set of deformation mechanisms in Equation 2.4. In a formulation of a stress-limiting deformation mechanism, the resulting strainrate dependent 'yield viscosity' is defined as:

$$\eta_y = \tau_y \dot{\epsilon}_y^{-1/n_y} \dot{\epsilon}^{1/n_y - 1} \tag{2.5}$$

to limit the strength of the material to approximately the yield stress τ_y. The powerlaw index n_y defines the brittleness of the stress limited material, ranging from $n_y = 1$ (in which case $\eta_y = \eta_{max}$) to $n_y \to \infty$ for a strainrate-independent brittle failure. In this thesis, $n_y = 1$, $n_y = 5$, or $n_y \to \infty$ was taken. Applied values for η_{max} or σ_y are given in the model descriptions of Chapters 4 to 8.

2.3   Governing equations

The velocity field of the mantle and lithospheric plates in the Earth is described with a viscous flow model, and the extended Boussinesq approximations (EBA) are applied (Ita and King, 1994). These imply the approximations of a divergence-free velocity field, and a constant density ρ_0, except for in the buoyancy term of the momentum conservation equations.

   Mass is conserved with a divergence-free velocity field:

$$\partial_j u_j = 0 \tag{2.6}$$

and conservation of momentum is described with the Stokes equation:

$$\partial_j(\eta \dot{\epsilon}_{ij}) - \partial_i \Delta P = \Delta \rho g_i \tag{2.7}$$

where the right-hand side gives the total density variation as described in Eq. 2.1. All symbols are given in Table 2.1. The temperature distribution is described by energy conservation in the following equation:

$$\rho c_p \left(\frac{\partial T}{\partial t} + u_j \partial_j T \right) - \alpha T \frac{dP}{dT} - \sum_k \rho_0 T \Delta S \frac{d\Gamma_k}{dt} - \partial_j(k \partial_j T)$$
$$= \tau_{ij} \partial_j u_i + \rho_0 H \tag{2.8}$$
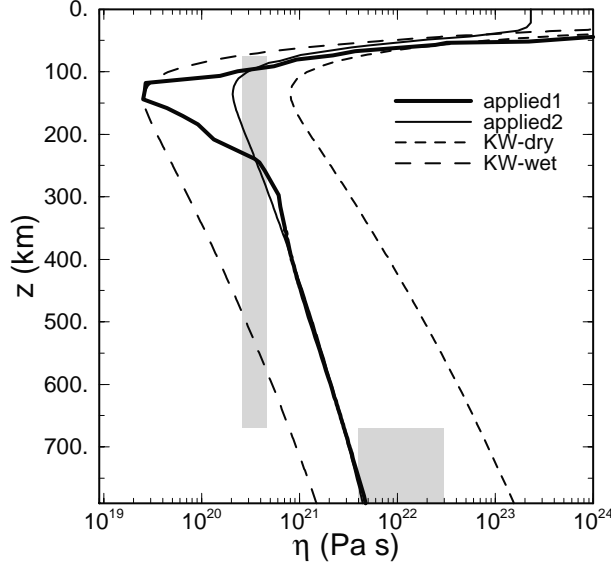
Figure 2.1: *Compilation of vertical viscosity profiles through a 40-Ma old oceanic litho-sphere in a mantle with a $1300^\circ C$ potential temperature. The thick solid line is a typical profile example from model calculations (applied1). Using the same rheological param-eters, the thin solid line gives a profile in case of a constant strainrate $\dot{\epsilon} = 10^{-15}$ s^{-1} (applied2). Dashed lines represent the wet (KW-wet) and dry (KW-dry) profiles for rheo-logical parameters from (Karato and Wu, 1993)(using $\mu = 80$ GPa, $b = 0.5$ nm, $d = 1$ mm and $m = 2.5$) for $\dot{\epsilon} = 10^{-15}$s^{-1}. The grey areas give the effective viscosity, as proposed by Lambeck et al. (1998) from post-glacial rebound results.*

In words, the equation describes the temperature change in time of a fixed point in the model (1st term on the left) due to heat advection (2nd term), (latent) heating or cool-ing due to adiabatic (de)compression (3rd term), latent heat from the major mantle phase transitions (4th term, see section 2.4.1) and diffusion of heat (5th term). Heat sources, in-corporated in the model are viscous heating (1st term on the right) and radiogenic heating (2nd term). Due to a negligible compositional diffusion and assumed absence of chemical reactions between the different compositions (materials) in the model, the composition conservation is described by a purely advective transport equation:

$$\frac{\partial C}{\partial t} + u_j \partial_j C = 0 \tag{2.9}$$

This set of equations is non-dimensionalised with the following scaling scheme:

$$\vec{x} = \vec{x}'h, \quad t = t'h^2/\kappa, \quad \vec{u} = \vec{u}'\kappa/h, \quad T = T_s + T'\Delta T = \Delta T(T' + T_0)$$

For the variable viscosity, an arbitrary scale value $\eta_0 = 10^{21}$ Pa s is taken, which approximates the average viscosity in the model. Removal of accents gives the following set of non-dimensionalised governing model equations:

$$\partial_j u_j = 0 \qquad (2.10)$$

$$\partial_j(\eta\dot{\epsilon}_{ij}) - \partial_i \Delta P = (RaT - \sum_k Rb_k\Gamma_k + RcC)\delta_{iz} \qquad (2.11)$$

$$\frac{\partial T}{\partial t} + u_j\partial_j T - Di(T + T_0)w - \sum_k \gamma_k\frac{Rb_k}{Ra}Di(T + T_0)\frac{d\Gamma_k}{dt} - \partial_j\partial_j T$$

$$= \frac{Di}{Ra}\Phi + H \qquad (2.12)$$

$$\frac{\partial C}{\partial t} + u_j\partial_j C = 0 \qquad (2.13)$$

2.4   Phase transitions

2.4.1   The major mantle phase transitions

The two most important phase transitions in the mantle are the transition from olivine to spinel at approximately 400 km depth, and the one from spinel to post-spinel (perovskite plus magnesiowüstite) at about 670 km depth. The depth of each transition varies with the ambient temperature, and the relation between the depth and temperature deviation from their reference values is given by the Clapeyron slope $\gamma_k = \frac{dP}{dT}$. Latent heat release or absorption during the transition is described by Christensen and Yuen (1985):

$$Q_{L,k} = \gamma_k\delta\rho_k T/\rho_0^2 \qquad (2.14)$$

Depression or uplift of an equilibrium phase boundary in combination with the density contrast $\delta\rho_k$ across the phase transition defines the phase buoyancy in Eq. 2.1. We parameterize a di-variant phase transition with phase function Γ_k varying from 0 to 1 with the following functional description:

$$\Gamma_k = \frac{1}{2}\left(1 + \sin(\pi\frac{z - z_0(T)}{d_{ph}})\right) \qquad (2.15)$$

where d_{ph} defines the width of the transition, and $z_0(T)$ the temperature dependent transition depth. The metastability of the olivine $\rightarrow$ spinel reaction may have important effects on the phase buoyancy inside cold descending slabs (Sung and Burns, 1976; Rubie and Ross II, 1994; Kirby et al., 1996b). In this thesis, however, the effect of olivine metastability has not been included, because all subducting slabs are relatively young (< 60 Ma) and therefore too warm for olivine meta-stability to be significant (Schmeling et al., 1999). The effects of the major mantle phase transitions are included in the models in Chapters 5 to 8 in this thesis. The parameters used are given in Table 2.1 .

2.4.2   Crustal metamorphism

When the oceanic plate subducts into the mantle, its crust eventually transforms into eclogite through a series of intermediate phases in a process called metamorphism. A detailed description of this metamorphic process as a function of pressure and temperature is given by Peacock (1993). The density increases stepwise with about $600 \ \mathrm{kg/m^3}$ from the basalt to the eclogite stability field.

The kinetics of the basalt-to-eclogite transitions are not always so fast that we may assume equilibrium. Geological observations show the occurrence of suppressed eclogitisation in the eclogite stability field (Hacker, 1996; Austrheim, 1998). Temperature plays an important role in the reaction rates, and disequilibrium phases occur less often for high peak metamorphic temperatures. This is, however, not the only controlling parameter, as complete transformation at $250^{o}C$ and incomplete transformation at $800^{o}C$ have been observed (Hacker, 1996). Grainsize, and the amount of hydration and deformation are also very important (Rubie, 1990). Ahrens and Schubert (1975) already reported large delay times for dry conditions in laboratory eclogitisation experiments.

Because the crustal buoyancy and therefore the eclogitisation process is of crucial importance for the subduction process in some of the presented models, the possibility of a kinetically delayed transformation has been included in those models. For time-dependent pressure and temperature conditions, a general description of a kinetically delayed phase transition can be parameterized by a phase function $\Gamma(P, T)$ with values between 0 and 1 similar to the phase functions Γ_k, introduced for solid-state phase transitions of olivine and spinel,

$$\frac{d\Gamma}{dt} = \Theta \tag{2.16}$$

for a transformation reaction rate Θ of the transition from basalt to eclogite. The kinetics of a phase transition are usually described with a nucleation and growth theory (Riedel and Karato, 1996). This theory describes the formation of the new phase as the simultaneous nucleation of crystals of the new phase, and growth of the newly formed crystals. These processes are parameterized through dimensionless nucleation rate I and a growth rate Y of the grains of the new phase, and accurate solutions of the theory involve multiple time integrations (Kirkpatrick, 1976). Riedel and Karato (1996) and Däßler et al. (1996) describe a numerical solution method by means of a system of ordinary differential equations. Simpler parameterizations of the problem are proposed in (Giunchi and Ricard, 1999) and in (Schmeling et al., 1999). For the implementation of kinetic hindrance in the presented models, I have adopted the method by Giunchi and Ricard (1999). Because of the various uncertainties in the parameters that describe the nucleation and growth of the eclogitisation process, this formulation uses the same pressure and temperature dependence in the nucleation function I and growth function Y, and has the following expression for the reaction rate:

$$\Theta = 4Y\left((\Gamma(1 - \Gamma))^{\frac{3}{4}} + \epsilon\right) \tag{2.17}$$

with $\epsilon = 10^{-3}$ a small constant to start the reaction. The growth function Y is given by

$$Y = A_{kin}T \exp\left(\frac{-E_{kin}}{RT}\right)\left[1 - \exp\left(\frac{\Delta G}{RT}\right)\right] \quad \text{for } \Delta G < 0$$
$$Y = 0 \quad \text{for } \Delta G > 0 \tag{2.18}$$

with A_{kin} a prefactor for the growth of the nuclei of the new phase and ΔG the pressure and temperature dependent Gibbs free energy difference between the old and the new phase. The kinetic activation energy E_{kin} relates the reaction rate Θ to the temperature T, once the material has well entered the eclogite stability field (in which case $\Delta G \ll 0$), and determines the kinetic hindrance of the phase transition. The effect of hydration on the kinetics is not explicitly modeled, but incorporated implicitly through variation of this kinetic activation energy E_{kin}. As in (Giunchi and Ricard, 1999), we substituted the detailed pressure-temperature diagram from Peacock (1993) by the following simple uni-variant phase transition:

albite $\rightarrow$ jadeite + quartz
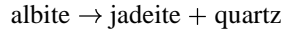
for which ΔG is accurately determined (Putnis, 1992).

$$\Delta G = (p - p_{eq})\Delta V - (T - T_{eq})\Delta S \tag{2.19}$$

with $p_{eq} = 1.975$ GPa and $T_{eq} = 1000$ K describing an arbitrary equilibrium point. The molar volume difference $\Delta V = -1.701 \times 10^{-5}$ J/Pa and the entropy difference $\Delta S = -44.7$ J/K between the old and new phase are taken pressure and temperature independent, which gives a linearized parameterization around the equilibrium point, and a constant Clapeyron slope γ.

2.5 Model geometry and boundary conditions

The subduction zone calculations are all performed in a Cartesian model domain with a depth of 2000 km and a horizontal extent ranging from 2600 km to 5200 km. One of the main issues of this thesis is the importance of several different driving mechanisms in producing shallow flat subduction at Andean-type subduction zones. Several mechanisms are explicitly incorporated in the numerical model to examine their influence on the subduction process.

One of these mechanisms is lithospheric doubling, which describes shallow flattening of a subducting oceanic plate below a oceanward moving overlying plate, relative to the deep mantle. All model calculations have a fixed and prescribed overlying plate motion, relative to the deep mantle. This implies that the forces, responsible for the overriding plate motion, are external to the model and not explicitly modeled. For numerical reasons, it is convenient to keep the trench in a fixed position in the model domain. This is achieved by choosing a reference frame which is fixed to the overlying plate. The horizontal relative motion $\vec{v} = \vec{v}_{ov}$ of the continent with respect to the deep mantle is modeled with a no-slip condition ($\vec{v} = 0$) at the surface of the continent and a velocity boundary condition

$\vec{v} = -\vec{v}_{ov}$ at the left hand side and bottom boundary. An appropriate right-hand side boundary condition is a 'developed flow' boundary condition, i.e. horizontal flow and a lithostatic pressure ($\sigma_{xx} = -p$). A free-slip boundary condition is imposed on the oceanic surface. This ensures a convergence rate that is consistent with the mantle flow field below and allows for the usage of the subduction rate as a model diagnostic.

An alternatively proposed mechanism for the occurrence of flat slabs is the subduction of buoyant oceanic lithosphere within an oceanic plateau, aseismic ridge or seamount chain. These features all have a thickened crust. In this case different boundary conditions are required, since without lithospheric doubling, the overlying plate velocity $\vec{v}_0$ is zero with respect to the deep mantle. Furthermore, a free-slip boundary condition would be inappropriate, because subduction would stop as soon as the buoyant feature enters the subduction zone. This is a consequence of the two-dimensionality of the model. In a three-dimensional setting, the plateaus only form a small part of the subducting plate. The majority of the plate does not have an overthickened crust and will provide sufficient slab pull to drive the subduction, even when parts of the plate contain a modestly overthickened, buoyant crust. Therefore, it is assumed in this model that the plateau subduction does not significantly influence the total convergence rate. This is achieved by imposing a constant velocity at the surface of the subducting plate. Thermal boundary conditions for all models are a surface temperature $T = 0^o$C, a prescribed temperature corresponding to a mantle adiabat, characterized by a specific potential temperature T_{pot}, at the bottom and left-hand side boundary, and zero diffusional heat flux through the right-hand side boundary. The compositional field is advanced by means of a tracer particle method in a Lagrangian framework (see Chapter 3). Due to absence of diffusion, only an initial condition, and no boundary conditions are required for the compositional field.

Plates are characterized by a strong rigid interior with little deformation and large localized strain zones at the edges (van den Berg et al., 1991; King et al., 1992). Coupling between the plates should be very low to avoid the formation of a stagnant lid (Zhong and Gurnis, 1992; Kincaid and Sacks, 1997). Near the surface, strain between the converging plates is accommodated through earthquakes on major faults by frictional sliding (Kohlstedt et al., 1995) or shear localization (Jin et al., 1998). To model these features in a narrow region between the converging plates, a fault was implemented, down to a depth of 100 km. In a general application, faults should be advected by the flow components normal to the fault (Zhong and Gurnis, 1994; Zhong et al., 1998). Within the geologically short time intervals of the presented model calculations, the geometry of the subduction zone is mainly determined by the shape of the overlying lithosphere. The fault is modeled with an arc-shaped static geometry. This is a good approximation of the generally observed subduction geometry (van den Beukel and Wortel, 1988). The dip angle increases from 0° at the surface to 23° at a depth of 100 km, which is in agreement with observed dip angles (Jarrard, 1986). The fault is modeled as two boundaries with exactly the same geometry, location and finite element node distribution. At the tip of the fault, the two boundaries are physically connected with one common nodal point. The fault plane is implemented as part of the external boundary of the computational domain, and therefore boundary conditions have to be specified (Barr and Houseman, 1996). For the energy equation, pairs of nodes on either side of the fault are connected, similar to periodical

boundary conditions. For the momentum equation, the slip over the fault Δv_T (i.e. the difference between tangential velocities on either side of the fault) is coupled to the shear stress τ on each side of the fault in a modified mixed boundary condition, using the fault stiffness definition from (Toth and Gurnis, 1998):

$$\tau = S\Delta v_T \tag{2.20}$$

$$S = S_0 \left(1 + \frac{1}{2}\tanh\left(\frac{z - z_L}{d_L}\right) \right) \tag{2.21}$$

in which the fault locking depth z_L and locking smoothness d_L control the stiffness coefficient S. A zero normal fault velocity boundary condition precludes flow through the fault.

Symbol	Meaning	Value used	Dimension
$A_{k,i}$	Pre-exponential flow law parameter	—	$\mathrm{Pa^{-n}\ s^{-1}}$
A_{kin}	Kinetic pre-exponent	10^{-6}	$\mathrm{K^{-1}\ s^{-1}}$
C	Composition parameter	—	—
c_p	specific heat	1250	$\mathrm{J\ kg^{-1}\ K^{-1}}$
Di	Dissipation number $= \alpha g h / c_p$	0.47	—
d	grain size	—	m
d_L	Locking smoothness of the stiffness coefficient S	1000	m
d_{ph}	width of the solid-state phase transitions	20	km
$E_{k,i}^*$	rheological activation energy	—	$\mathrm{J\ mol^{-1}}$
E_{kin}^*	kinetic activation energy	—	$\mathrm{J\ mol^{-1}}$
H	radiogenic heat production	—	$\mathrm{W\ m^{-3}}$
k	thermal conductivity	4.27	$\mathrm{W\ m^{-1}\ K^{-1}}$
i	deformation mechanism index	—	—
$m_{k,i}$	grain size exponent	—	—
$n_{k,i}$	viscosity stress exponent	—	—
n_y	yield stress exponent	5	—
Q_L	Latent heat release across a phase transition	—	$\mathrm{J\ kg^{-1}}$
R	gas constant	8.3143	$\mathrm{J\ K^{-1}\ m^{-3}}$
Ra	Thermal Rayleigh number $\rho_0 \alpha \Delta T h^3 / \eta_0 \kappa$	1.8×10^7	—
Rb	Phase Rayleigh number $\delta \rho_0 g h^3 / \eta_0 \kappa$	2.4×10^7	—
Rc	Compositional Rayleigh number $\Delta \rho_0 g h^3 / \eta_0 \kappa$	2.4×10^7	—
r	subduction to overriding velocity ratio	—	—
S	Stiffness of the fault $= S_0(1 + \tanh((z - z_L)/d_L))$	—	$\mathrm{Pa\ s\ m^{-1}}$
S_0	Maximum stiffness of the fault	10^{19}	$\mathrm{Pa\ s\ m^{-1}}$
T	temperature	—	$^\circ$C
T_0	non-dimensional surface temperature $T_s / \Delta T$	0.119	—
T_s	dimensional surface temperature	273	K
t	time	—	s
t_{tr}	transition time for the eclogitisation reaction	10	Ma
$\vec{u}$	velocity $\vec{u} = (v, w)^T$	—	$\mathrm{m\ s^{-1}}$
$V_{k,i}^*$	activation volume	—	$\mathrm{m^3\ mol^{-1}}$
v_{ov}	overriding velocity	—	$\mathrm{cm\ yr^{-1}}$

Table 2.1: *Notations*

Symbol	Meaning	Value used	Dimension
v_{subd}	subduction velocity	–	cm yr^{-1}
Y	growth function of the eclogitisation reaction	–	s^{-1}
z_0	transition depth of the solid-state phase transitions	–	m
z_L	fault locking depth	–	m
α	thermal expansion coefficient	3×10^{-5}	K^{-1}
Γ	phase function for the basalt-to eclogite transition	–	–
Γ_k	phase functions for all k mantle phase transitions	–	–
γ_k	Clapeyron slope of the k-th phase transition		
	400 km phase transition	3	MPa K^{-1}
	670 km phase transition	-2.5	MPa K^{-1}
ΔG	Gibbs free energy between basalt and eclogite	–	J mol^{-1}
ΔP	non-dimensional hydrodynamic pressure	–	–
ΔS	entropy difference between basalt and eclogite	-44.7	J K^{-1}
ΔT	vertical temperature contrast across model domain	2300	K
$\Delta \rho$	total density variation with respect to ρ_0		kg m^{-3}
$\Delta \rho_c$	compositional density relative to mantle material		
	basalt	-400	kg m^{-3}
	harzburgite	-77	kg m^{-3}
δT	temperature increase due to latent heat release	–	K
ΔV	molar volume difference between basalt and eclogite	-1.701×10^{-5}	J Pa^{-1}
Δv_T	slip over fault plane	–	m s^{-1}
δz	phase transition deflection	–	m
$\delta \rho_k$	density difference across the k-th phase transition		
	400-km phase transition	273	kg m^{-3}
	670-km phase transition	342	kg m^{-3}
$\dot{\epsilon}_{ij}$	$\dot{\epsilon}_{ij} = \partial_j u_i + \partial_i u_j$ = strainrate tensor	–	s^{-1}
$\dot{\epsilon}$	2nd invariant of the strainrate	–	s^{-1}
$\dot{\epsilon}_y$	reference strainrate in yield strength determination	10×10^{-15}	s^{-1}
η	viscosity	–	Pa s
η_0	reference viscosity	10^{21}	Pa s
Θ	eclogitisation rate	–	s^{-1}
κ	thermal diffusivity	10^{-6}	m^2 s^{-1}
ρ_0	mantle density	3416	kg m^{-3}
τ_y	yield stress	–	Pa
τ_{ij}	deviatoric stress tensor	–	Pa
τ	2nd invariant of the stress tensor τ_{ij}	–	Pa
τ_y	yield stress for strainrate $\dot{\epsilon}_y$	–	Pa
Φ	viscous dissipation	–	W m^{-3}

Table 2.1: *Notations (continued)*

Chapter 3

Numerical methods

The conservation Equations 2.10 to 2.13 are solved with two different numerical techniques. Conservation equations for mass, momentum and energy are solved with an Eulerian finite element technique, while the transport of composition is performed with a Lagrangian tracer particle method. The finite element method is one of the most commonly used methods to solve partial differential equations (PDEs), such as described in Chapter 2. Principally, it provides a method to transform a PDE into a system of algebraic equations (Cuvelier et al., 1986). Advantages of the method are the arbitrary shape of the model domain and the flexibility in mesh refinement. Tracer methods found early applications in plasma physics and astronomy (Hockney and Eastwood, 1988; Birdsall and Langdon, 1991). They have been used in geodynamical modelling in the 1980's in the study of mixing problems (e.g. Gurnis and Davies, 1986), but its usage for the transport of non-diffusive properties have become significant in the last decade (Weinberg and Schmeling, 1992; Christensen and Hofmann, 1994). The set of coupled equations are integrated in time with a predictor-corrector scheme. All calculations are performed with a code that is based on the finite element package SEPRAN (Segal and Praagman, 2000). This chapter discusses the solution techniques for the time integration, the time-dependent energy equation and the combined solution of the continuity and Stokes equations. The code has been tested for numerical accuracy with numerical benchmarks for thermal convection (Blankenbach et al., 1989) and Rayleigh-Taylor instabilities (van Keken et al., 1997).

3.1 Time integration scheme

In the set of equations from Chapter 2, the time-dependence is introduced through the energy and composition transport equations, and, in some models, through the kinetics of the basalt-to-eclogite phase transition. Since inertial forces can be neglected and the assumption of an incompressible fluid is made, the conservation equations for mass and momentum (Equation 2.10 and 2.11) contain no explicit time dependence. The nonlinear,

time-dependent system of Equations 2.10 to 2.13 is solved with a Predictor-Corrector (PC) scheme (van den Berg et al., 1993; van Keken, 1993; de Smet, 1999). The structure of the PC-scheme is shown in Figure 3.1. For each integration time step, a prediction

$$
\begin{array}{llll}
\text{Predictor:} & T_C^n,\ C_C^n,\ v_C^n & \text{IE} & \to T_P^{n+1} \\
 & v_C^n & \text{RK2} & \to C_P^{n+1} \\
 & T_P^{n+1},\ C_P^{n+1} & & \to v_P^{n+1} \\[1em]
\text{Corrector:}\quad T_C^n,\ T_P^{n+1},\ C_C^n,\ C_P^{n+1},\ v_C^n,\ v_P^{n+1} & & \text{CN} & \to T_C^{n+1} \\
 & v_C^n,\ v_P^{n+1} & \text{RK4} & \to C_C^{n+1} \\
 & T_C^{n+1},\ C_C^{n+1} & & \to v_C^{n+1}
\end{array}
$$

Figure 3.1: *Predictor-Corrector scheme for the time integration of the set of Equations 2.10 to 2.13 and applied integration schemes: IE=Implicit Euler, RK2= 2nd order Runge-Kutta, CN=Crank-Nicholson, and RK4= 4th order Runge-Kutta. The superscripts give the time step number, while subscripts refer to the predictor (P) or corrector (C) solution within that time step.*

of temperature, compositional distribution, and velocity field is first made for time step $n+1$, using the results from time step n. Then, results are updated in a corrector step, using the information from the predictor step. In the third step of both the predictor and the corrector step, the discretized non-linear Stokes equation is solved using Picard (sub-)iterations (van den Berg et al., 1993).

   The integration time step is mainly controlled by the time CFL-criterion (Vreugdenhil, 1989; van den Berg et al., 1993):

$$\Delta t = f \Delta t_{CFL} \tag{3.1}$$

where Δt_{CFL} is the maximum time step according to the CFL-criterion, and f some multiplication factor. Values for f from 0.5 to 2 are applied and tested for the resultant accuracy. A second constraint on the time step is based on a maximum relative temperature change over the predictor time step, using the sup-norm:

$$\frac{||T_P^{n+1} - T_C^n||_\infty}{||T_C^n||_\infty} < \epsilon_T \tag{3.2}$$

where $\epsilon_T = 0.02$ is taken in all calculations. For a too large temperature change, the predictor calculation of the temperature field is repeated with a smaller time step, before continuing with the corrector step.

3.2   The solution of the energy, continuity and Stokes equation

Using the standard Galerkin approach, the energy conservation Equation 2.12 is written in the weak formulation, and discretized to form a system of ordinary differential equations (Segal, 1993):

$$M\dot{T} + ST = F \tag{3.3}$$

where M is the mass or heat capacity matrix, S the stiffness matrix that combines effects of diffusion, advection and adiabatic compression, and the dot denotes the time derivative. Equation 3.3 is solved with a modified first-order accurate implicit Euler scheme in the predictor (van den Berg et al., 1993):

$$[M + \Delta t S_C^n] T_P^{n+1} = MT_C^n + \Delta t F_C^n \tag{3.4}$$

Note that S_P^{n+1} and F_P^{n+1} from the original implicit Euler scheme are replaced by S_C^n and F_C^n, respectively, as coefficients for the calculation of S and F for the new time step $n + 1$ are not yet available in the predictor. In the corrector, Equation 3.3 is solved with a second order accurate Crank-Nicholson scheme (van den Berg et al., 1993):

$$\left[M + \frac{\Delta t}{2} S_P^{n+1}\right] T_C^{n+1} = \left[M - \frac{\Delta t}{2} S_C^n\right] + \frac{\Delta t}{2} \left[F_P^{n+1} + F_C^n\right] \tag{3.5}$$

Now, S^{n+1} and F^{n+1} are calculated from the predictor solutions. Both Equations 3.4 and 3.5 are solved with a direct solution method.

The combination of the continuity and Stokes equations (Equations 2.10 and 2.11, respectively) are solved simultaneously using a penalty function method (Cuvelier et al., 1986). This set of equations is solved on a quadratic, triangular element (the Crouzeix-Raviart element, with velocity unknowns in 7 nodes, and a pressure unknown with two derivatives in the baricenter). The number of unknowns in the system is reduced by eliminating the pressure derivatives and the velocity unknowns in the baricenter, which results in the modified $P_2^+ - P_1$ Crouzeix-Raviart element (Cuvelier et al., 1986). In the penalty function method, the right-hand side of Equation 2.10 is slightly modified with the pressure times a small constant (the penalty parameter), after which the pressure can be eliminated from the set of equations (Cuvelier et al., 1986; van Keken, 1993; Segal and Praagman, 2000).

The temperature field is solved on linear triangular element mesh with the same nodal points distribution as for the extended quadratic element mesh. This is achieved by subdividing each quadratic element into four linear (sub)elements (van den Berg et al., 1993; van Keken, 1993).

3.3   The tracer method

The absence of diffusion in Equation 2.13 for composition conservation makes it numerically difficult to solve this equation using a standard Galerkin method (Segal, 1993), as

applied in the solution for the energy conservation Equation 2.12. Therefore, Equation 2.13 is solved with a tracer technique. In this method, a large number of particles (or tracers) carry the compositional information, which is distributed over (a part of) the model domain. The particles are transported with the velocity field from Equation 2.11, using Runge-Kutta schemes. These schemes represent socalled explicit integration methods, implying that they do not require the solution of a large system of equations. Each particle is transported with an explicit second or fourth order Runge-Kutta time integration scheme (Press et al., 1992). Data exchange between tracer solutions and finite element solutions is necessary to solve the coupled system of equations from Chapter 2. This is performed through interpolation of the tracer solutions to the finite element nodal points or gaussian points, and vice versa. The finite element shape functions are used to interpolate from the mesh to the particles. For the particle-to-mesh interpolation, two methods are implemented: a Particle-In-Cell (PIC) interpolation (Hockney and Eastwood, 1988; Birdsall and Langdon, 1991) and a Shepard method (Shepard, 1968). On average, approximately 5×10^5 tracers are used in each calculation. Appendix A describes the transportation and interpolation schemes of the tracer method in more detail.

$$
\begin{aligned}
\text{in Predictor:} \quad \frac{d\Gamma_P^{n+1}}{dt} &= \Theta(T_P^{n+1}, \vec{x}_P^{n+1}, \Gamma_C^n) \\
\Gamma_P^{n+1} &= \Gamma_C^n + \frac{\Delta t}{2}\left(\frac{d\Gamma_C^n}{dt} + \frac{d\Gamma_P^{n+1}}{dt}\right) \\
\text{in Corrector:} \quad \frac{d\Gamma_C^{n+1}}{dt} &= \Theta(T_C^{n+1}, \vec{x}_C^{n+1}, \Gamma_P^{n+1}) \\
\Gamma_C^{n+1} &= \Gamma_C^n + \frac{\Delta t}{2}\left(\frac{d\Gamma_C^n}{dt} + \frac{d\Gamma_C^{n+1}}{dt}\right)
\end{aligned}
$$

Figure 3.2: *Time integration scheme for basalt-to-eclogite phase change kinetics. See Fig. 3.1 for sub- and superscript descriptions.*

The simplest application of the tracer technique is the advection of constant non-diffusive quantities. In this thesis, the composition field (or material field, distinguishing lherzolitic and harzburgitic mantle material and basaltic oceanic crust) is transported in time through the model domain. The resulting time-dependent composition distribution over the model domain is interpolated to the finite element mesh to determine material-dependent properties, such as density and viscosity. In this application, the composition value of each particle is constant through time. Another, more advanced application of the tracer method in this thesis is in the phase change kinetics of the basalt-to-eclogite phase transition. Equations 2.16 and 2.17 are solved numerically after the transport of the tracers in the PC-scheme (section 3.1) with a Crank-Nicholson trapezium rule integration. Figure

3.2 schematically shows the time integration procedure. To calculate the eclogitisation rate Θ, this scheme requires the temperature field to be interpolated (linearly) from the finite element mesh to the particle coordinates.

Chapter 4

A thermo-mechanical model of horizontal subduction below an overriding plate

Abstract

Subduction of young oceanic lithosphere, cannot be explained by the gravitational driving mechanisms of slab pull and ridge push. This deficiency of driving forces can be overcome by obduction of an actively overriding plate, which forces the young plate either to subduct or to collide. This mechanism leads to shallow flattening of the slab as observed today under parts of the west coast of North and South America.

   Here this process is examined by means of numerical modeling. The convergence velocity between oceanic and continental lithospheric plates is computed from the modeling results, and the ratio of the subduction velocity over the overriding velocity is used as a diagnostic of the efficiency of the ongoing subduction process. We have investigated several factors influencing the mechanical resistance working against the subduction process. In particular, we have studied the effect of a preexisting lithospheric fault with a depth dependent shear resistance, partly decoupling the oceanic lithosphere from the overriding continent. We also investigated the lubricating effect of a seven km thick basaltic crustal layer on the efficiency of the subduction process and found a log-linear relation between convergence rate and viscosity prefactor characterizing the strength of the oceanic crust, for a range of parameter values including values for basaltic rocks, derived from empirical data. A strong mantle fixes the subducting slab while being overridden and prevents the slab from further subduction in a Benioff style. Viscous heating lowers the coupling strength of the crustal interface between the converging plates with about half an order

of magnitude and therefore contributes significantly to the subduction process. Finally, when varying the overriding velocity from 2.5 to 10 cm/yr, we found a non-linear increase of the subduction velocity due to the presence of non-linear mantle rheology. These results indicate that active obduction of oceanic lithosphere by an overriding continental lithosphere is a viable mechanism for shallow flat subduction over a wide range of model parameters.

4.1   Introduction

Gravitational instability forces such as slab pull and ridge push mainly drive Benioff type of subduction, while the most important resistance comes from internal friction and friction or drag from the overriding plate and mantle below. The dominance of slab pull and ridge push over the resisting forces makes subduction an active process: the net driving force is internally created. For young oceanic plates, however, resisting forces would dominate in this setup, since oceanic plates younger than about 30 Ma are gravitationally stable due to the buoyant lithosphere. In this case, other driving forces are necessary for subduction to occur. Vlaar (1983) proposed the lithospheric doubling scenario as a possible mechanism: in this scenario a continent overrides a young oceanic plate (obduction) and this plate subducts rather passively along with the mantle underneath. Reconstructions of absolute plate motion show an overriding velocity at subduction zones along the western Americas in the past and present (Engebretson et al., 1985; Gordon and Jurdy, 1986; Gripp and Gordon, 1990; Doglioni, 1990). Lithospheric doubling would result in shallow flattening of the subducted slab and could therefore be an explanation for the flat slab segments which have been observed using various geological and geophysical methods. A similar effect could be expected from an eastward moving mantle as suggested in (Doglioni, 1990). Vlaar and Wortel (1976) investigated dip angles of subducting plates defined by means of earthquake hypocenters. They suggested a correlation might be present between the lithospheric age and the dip angle of the subducting slab. Cross and Pilger (1982) suggested a correlation between the dip angle and the absolute overriding plate motion, convergence rate, slab age and the subduction of aseismic ridges. Flat subduction probably occurred around 65 Ma ago below the Western USA and may have caused the Laramide orogeny and related tectonic features (Bird, 1988; Spencer, 1996; van der Lee and Nolet, 1997). This has been concluded from seismic data, heat flow measurements, migrating patterns of magmatism, tectonic reconstructions and tomographic images. Present-day horizontal subduction occurs at the west coast of Mexico and Central Chile (Vlaar and Wortel, 1976; Wortel and Vlaar, 1978; Sacks, 1983; Gutscher et al., 1999a).

Other mechanisms for flat lying subduction have previously been proposed. The 670-km discontinuity phase change can easily result in flat lying slabs in case of sufficient roll-back (Zhong and Gurnis, 1995; Christensen, 1996; Olbertz, 1997). However, this occurs in the transition zone and not at shallow depth, directly below the overriding plate. Furthermore, the trench roll-back is a result of the pulling force which is generated by an old and heavy slab and not by young and gravitationally stable slabs. Buoyant plateaus

may give an explanation for shallow flattening of the subducting plates (Gutscher et al., 1999a), but do not form a driving mechanism for this type of subduction. With adherence to the overriding plate by a non-hydrostatic pressure force (Jischke, 1975) or a slab suction force (Stevenson and Turner, 1977; Tovish et al., 1978), a deflection of the subducting slab towards the horizontal can be explained. These models, however, do not propose a driving force for flat subduction, but merely a mechanism to flatten an already subducting plate.

Plate tectonics are characterized by strain concentration within the plate margins. Large strains are accommodated by faults systems between the converging plates. The importance of such faults in the dynamics of the subduction process has been shown in (Zhong and Gurnis, 1995; Zhong et al., 1998). Localized ductile deformation is observed in models using highly nonlinear stress weakening rheologies (van den Berg et al., 1991; Zhong et al., 1998; Trompert and Hansen, 1998). Other mechanisms are provided by compositionally defined lubricants, such as a hydrated oceanic crust (Lenardic and Kaula, 1994), or by viscous heating (Yuen et al., 1978; Schott et al., 1999). Here, we investigate the relative importance of faults, crustal strength and mantle strength in the process of lithospheric doubling by means of numerical modeling. First, we present the numerical model, including the implementation of a lithospheric fault and tracking of compositional differences. Next, we examine the influence on the subduction dynamics of various model parameters systematically. Finally, we discuss the applications of the results for the Earth.

4.2   model description

4.2.1   governing equations

We assume an incompressible medium with infinite Prandtl number and we apply the extended Boussinesq approximation (Ita and King, 1994). We use the same non-dimensionalization scheme as in (van den Berg et al., 1993). The non-dimensional continuity and momentum equation are respectively:

$$\partial_j u_j = 0 \tag{4.1}$$

$$\partial_j(\eta \dot{\epsilon}_{ij}) - \partial_i \Delta P = (RaT + RcC)\delta_{iz} \tag{4.2}$$

in which both thermal and compositional buoyancy are accounted for in the right hand side of Equation (4.2). Symbols used are defined in Table 4.1. A compositional (crust-mantle) layering for the subducting oceanic lithosphere is defined through a bi-valued composition distribution $C(\mathbf{x})$ which is advected with the flow. The non-diffusive transport equation for the composition,

$$\frac{\partial C}{\partial t} + u_j \partial_j C = 0 \tag{4.3}$$

is solved using a Lagrangian particle tracer method (see section 4.3). Both buoyancy and effective viscosity are defined to be dependent on the composition. This way, we have

used different rheological flow laws for the basaltic oceanic crust and underlying mantle. Conservation of energy is described by the non-dimensional heat equation:

$$\frac{\partial T}{\partial t} + u_j \partial_j T - Di(T + T_0)w - \partial_j \partial_j T = \frac{Di}{Ra}\Phi + H \tag{4.4}$$

where adiabatic (de)compression and thermal diffusion correspond to the third and fourth term in the left hand side, respectively. Viscous dissipation and radiogenic heating are included through the first and second right hand terms, respectively.

Parameter	Meaning	Value used	Dimension
A	Pre-exponential flow law parameter	—	$Pa^{-n}s^{-1}$
ΔA	Variation of A relative to values in Table 4.2	—	—
B	Viscosity prefactor $= A^{-1/n}$	—	$Pa\,s^{1/n}$
C	Composition parameter	—	—
d_L	Smoothness of the stiffness variation	1000	m
Di	Dissipation number $= \alpha g h / c_p$	0.47	—
E^*	activation energy	—	$J\,mol^{-1}$
H	non-dimensional radiogenic heat production	—	—
n	viscosity stress exponent	—	—
r	subduction to overriding velocity ratio	—	—
R	gas constant	8.3143	$J\,K^{-1}\,m^{-3}$
Ra	Rayleigh number $=\rho \alpha \Delta T h^3 / \eta \kappa$	1.8×10^7	—
Rc	Compositional Rayleigh number $\Delta \rho_c g h^3 / \eta \kappa$	2.4×10^7	—
S	Stiffness of the fault $= S_0(1 + \tanh((z - z_L)/d_L))$	—	$Pa\,s\,m^{-1}$
S_0	Maximum stiffness of the fault	10^{19}	$Pa\,s\,m^{-1}$
T	non-dimensional temperature	—	—
T_0	non-dimensional surface temperature	$273/\Delta T$	—
ΔP	non-dimensional hydrodynamic pressure	—	—
ΔT	temperature contrast across model domain	2300	K
t	non-dimensional time	—	—
$\mathbf{u}$	non-dimensional velocity $\mathbf{u} = (v, w)^T$	—	—
V^*	activation volume	—	$m^3 mol^{-1}$
v_{ov}	overriding velocity	—	$cm\,yr^{-1}$
v_{subd}	subduction velocity	—	$cm\,yr^{-1}$
z_L	locking depth in stiffness definition	—	m
$\dot{\epsilon}_{ij}$	$\dot{\epsilon}_{ij} = \partial_j u_i + \partial_i u_j =$ strainrate tensor	—	s^{-1}
$\dot{\epsilon}$	2nd invariant of the strain rate tensor $\dot{\epsilon}_{ij}$	—	s^{-1}
η	non-dimensional viscosity	—	—
Φ	non-dimensional viscous dissipation	—	—
ρ_c	crustal density	3116	$kg\,m^{-3}$
ρ_m	mantle density	3416	$kg\,m^{-3}$
τ_{ij}	deviatoric stress tensor	—	Pa
τ	2nd invariant of the stress tensor τ_{ij}	—	Pa

Table 4.1: *Notations*

4.2.2   Boundary and initial conditions

The subduction process is modeled in a 2-D Cartesian box of 2000 km deep and 2600 km wide. High lower mantle viscosity in this model results in a shallow concentration of the shear, which makes the results relatively insensitive to the depth of the model truncation boundary. Boundary and initial conditions are shown schematically in Figure 4.1.
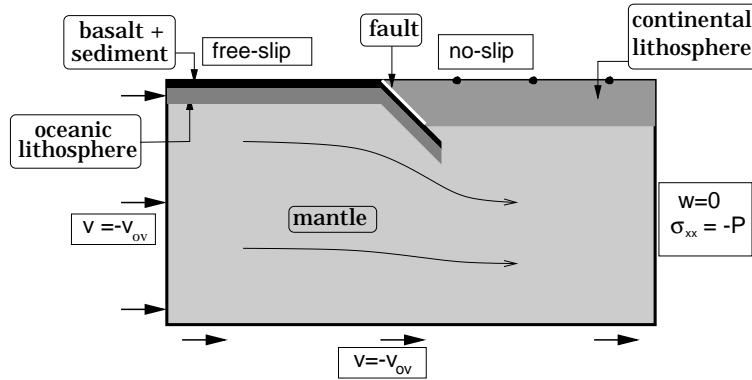

Figure 4.1: *Description of the mechanical boundary conditions: relative motion between continent and mantle (at left hand vertical and and bottom boundary) is imposed. Free-slip and fully developed horizontal flow ($\sigma_{xx} = -P$) conditions are used for the oceanic surface and right hand boundary, respectively.*

Initially the shallow part of the model is divided into an oceanic and a continental lithosphere. The geotherm of the oceanic lithosphere and mantle is based on the cooling of an initially adiabatic temperature distribution with a 1300^oC potential temperature. The initial geotherm of the continent is defined as a steady state temperature profile using crustal radiogenic heat production values according to (Chapman, 1986), corresponding to a $60 \mathrm{~mW/m^2}$ surface heatflow. Oceanic radiogenic heat production is neglected in the models. To avoid the special case of initiation of subduction, we defined an already developed subduction zone: an oceanic plate without a leading slab was thermally and compositionally defined with a five-cm-per-year half spreading rate. This plate was subducted with a fixed five-cm-per-year subduction velocity for 8 Ma to create the initial condition for further model calculations, with a subducted slab just entering the asthenosphere. We define this moment as time $t = 0$, from which the oceanic surface boundary condition becomes free-slip and the convergence rate becomes a free, rather than a fixed parameter. We use this initial condition for all model calculations. The oceanic plate has an age of 8 Ma at the trench. We study the subduction below an actively overriding continent with an ocean-ward velocity $\mathbf{v_{ov}} = (v_{ov}, 0)$ with respect to the deep mantle. Although the reference frame in subduction models is usually fixed to the deep mantle, we choose a 'continental reference frame' here, which is fixed to the top surface of the

overriding continental lithosphere, for reasons of computational convenience. To this end, we use a simple galilean coordinate transformation: a no-slip boundary condition is imposed on the continental surface while at the bottom and inflow boundary, a velocity $-\vec{v}_{ov}$ is imposed, describing again the relative motion between continent and deep mantle. The oceanic surface is modeled as a free slip impermeable boundary, which enables the subduction velocity to develop in a self-consistent way. A horizontal flow and hydrostatic pressure are prescribed on the vertical left-hand side boundary. These define the flow to be 'developed', i.e. with a zero horizontal velocity gradient, as in one-dimensional channel flow. Thermal boundary conditions are: 0° C along the top surface $z = 0$, 2300^oC at the bottom surface, a continental geotherm at the right hand side boundary and a mantle adiabat at the left hand side boundary $x = 0$, corresponding to an adiabatic gradient of 0.5 K/km and a potential temperature of 1300^oC to represent the mid-ocean ridge.

4.2.3   rheological model

The applied mantle rheology is based on a composite rheological model combining both Newtonian and non-Newtonian flow, corresponding to diffusion and dislocation creep respectively (Karato and Wu, 1993; van den Berg et al., 1993; Zhong and Gurnis, 1995; van den Berg and Yuen, 1998). We use an Arrhenius relation for each of the flow components for both mantle and crustal materials:

$$\dot{\epsilon}_{ij} = A\tau^{n-1}\tau_{ij} \exp\left[-\frac{E^* + PV^*}{RT}\right] \tag{4.5}$$

where two sets of values for A, n, E^* and V^* are used for the two creep components. Symbols used are explained in Table 4.1. Each set of parameters is implemented in the model utilizing the bi-valued composition distribution C. These parameter sets are taken from the literature on experimentally determined flow laws for both upper mantle material and crustal material. Using the second invariants $\dot{\epsilon}$ and τ of strainrate and stress, respectively, the definition of the viscosity, $\eta = \tau/\dot{\epsilon}$ and a viscosity prefactor $B = A^{-1/n}$, we define the effective viscosity for each of the two creep components as:

$$\eta = B\dot{\epsilon}^{\frac{1-n}{n}} \exp\left[\frac{E^* + PV^*}{nRT}\right] \tag{4.6}$$

and define the effective viscosity as the geometric mean value of the two components (van den Berg et al., 1993). We truncated the effective viscosity at the high end to a value that increases linearly from 10^{20} Pa s to 10^{23} Pa s over the upper 40 km and a constant value of 10^{23} Pa s below this depth. This limits the strength of the cold lithosphere to reasonable values as indicated in, for example, (Kohlstedt et al., 1995). It essentially substitutes for other, not implemented deformation mechanisms, such as brittle failure or the Peierl's mechanism (Kameyama et al., 1999).

Activation parameters E^* and strain rate prefactors A for mantle material are adopted from values given in (Karato and Wu, 1993), as listed in Table 4.2. Comparison of the flow laws for the composite rheology with viscosity estimates from layered post-glacial

rebound models (Lambeck and Johnston, 1998; Lambeck et al., 1998) and geoid inversions (Hager, 1991) suggests a somewhat weaker mantle, although such a comparison is dependent on, for example, chosen geotherm and model dynamics. In order to achieve reasonable viscosity values for the deeper mantle, we define the activation volume for mantle diffusion creep to be $4.5\,\mathrm{cm^3/mol}$ and for mantle dislocation creep to $14\,\mathrm{cm^3/mol}$ (Karato and Rubie, 1997). We increased the prefactors A for both diffusion and dislocation creep with respect to (Karato and Wu, 1993) with half an order of magnitude to define an appropriate mantle strength for our reference model. This results in a reduction of the viscosity.

rock/mineral	$A(\mathrm{Pa^{-n}/s})$	n	$E^*(\mathrm{J/mol})$	reference
ST: Maryland diabase	8.8×10^{-25}	3.4	260×10^3	(Shelton and Tullis, 1981)
KW: dry diff. olivine	1.92×10^{-11}	1.0	300×10^3	(Karato and Wu, 1993)
KW: dry disl. olivine	2.42×10^{-16}	3.5	540×10^3	(Karato and Wu, 1993)

Table 4.2: *Rheology parameters*

The strength of the seven-km-thick basaltic oceanic crust is less accurately determined than the strength of olivine, and fewer data are available. Moreover, water plays an important role in the strength determination of crustal materials (Kohlstedt et al., 1995), but amounts of water in subducting oceanic crust are not well-known. We use the crustal flow law data from (Shelton and Tullis, 1981), to which we added a roughly estimated activation volume of $10\,\mathrm{cm^3/mol}$, and from which we increased the prefactor A from Equation 4.5 with two orders of magnitude to define a suitable crustal strength description for the crust in our reference model. Basalt is known to transform into denser and stronger eclogite during subduction. The depth range of this transition in subduction zones is not well-known due to poorly known kinetics of the phase transition as a function of inter-plate contact length, slab temperature and water content (Ahrens and Schubert, 1975; Vlaar, 1983; Sacks, 1983; Hacker, 1996; Iwamori, 1998). In this model we use a simple approach, in which we assume the crust to have properties intermediate between basalt and eclogite. Taking an intermediate value of -300 $\mathrm{kg/m^3}$ for the relative crustal density compensates for the absence of a light depleted harzburgitic layer beneath the crust. A more detailed study of the buoyancy effects of the subducting slab and the rheological implications of the basalt-to-eclogite transition is subject of future research.

4.2.4   Implementation of a lithospheric fault

The dynamics of plate convergence is best described by faulted plate interfaces (Zhong and Gurnis, 1995). To account for the effects of frictional sliding (Kohlstedt et al., 1995) and mylonitic shear localization behavior (Jin et al., 1998) in the upper part of the subduction zone, we implemented a static fault, with an arc-shaped geometry, as a reasonable approximation of the actual subduction geometry (van den Beukel and Wortel, 1988). In general, the fault has to be mobile and advected as in (Zhong and Gurnis, 1995; Toth and Gurnis, 1998) in order to adjust to the stress and flow field. The rather rigid overlying continent and relatively short time scales of the presented processes, however, justify the

assumption of a rigid fault. The dip angle of the fault increases from zero (horizontal) at the surface to 23 degrees at its deepest part at 100 km depth. Flow across the fault is not allowed and fault friction is defined using a fault stiffness definition, as described in (Toth and Gurnis, 1998). This way, the slip across a fault plane is coupled to the resisting shear force using $\tau = -Sv$, in which τ is the component of the stress, tangential to the fault and v the slip velocity tangential to the fault. S is the stiffness coefficient, parameterized as a hyperbolic tangent:

$$S = S_0(1 + 1/2\tanh(\frac{z - z_L}{d_L})) \tag{4.7}$$

in which z_L and d_L control the depth and smoothness of the fault locking zone. All experiments have $d_L = 1$ km, which results in a sharply determined locking depth.

4.3   Numerical techniques

In order to solve Equations (2.10), (2.11) and (2.12), we use the finite element package SEPRAN (Segal and Praagman, 2000). A penalty function method is used to solve the momentum equation, while the energy equation is integrated in time using a predictor-corrector scheme (van den Berg et al., 1993). A Lagrangian tracer particle method is used to solve Equation (2.13). 200,000 tracers are placed in and around the oceanic crustal layer. Each tracer corresponds to a particular parameter value C which is used to define the type of material, crust or mantle at the current tracer position. These tracer values are interpolated to the finite element mesh in the computation of the coefficients of the finite element equations. Tracers are advected with the flow field, using the 4th order Runge-Kutta scheme. Modeling of the relatively small-scale crust requires strong local mesh refinement and the usage of a locally high tracer density.

4.4   Results

We investigated the efficiency of subduction of an oceanic lithosphere below an overriding lithosphere. Different factors in our numerical model can influence the subduction of the oceanic lithosphere below the overriding plate. Of these, we examined in particular 1) the depth at which the subduction fault locks, 2) the viscosity of the basaltic crust, 3) the strength of the mantle, 4) viscous dissipation and 5) the overriding plate velocity. Table 4.3 lists the complete series of modeling experiments, where model A is used as a reference model.   Viscosity prefactors are defined relative to the flow laws from Table 4.2. Physical parameters are defined in Table 4.1. Figure 4.2 illustrates typical modeling results of the ongoing subduction process for model A. Shown are three snapshots of different times of the effective viscosity (Figure 4.2a,b,c) and temperature (Figure 4.2d,e,f). The outlines of the subducting slab are revealed by the dark areas, indicating low temperature and high viscosity. In the viscosity plots, the stiff oceanic and continental lithosphere is shown in black. In between, the much weaker oceanic crust is present. In both the

Model	A_{mantle}	A_{crust}	z_L (km)	v_{ov} (cm/yr)	Φ on/off	v_{subd} (cm/yr)	r	power (kW/m)
A	$10^{+0.5}KW$	10^{-2} ST	100	5	on	3.49	0.698	14.0
B	$10^{+0.5}KW$	10^{-2} ST	100	5	off	2.81	0.562	12.9
C1	$10^{-0.5}KW$	10^{-2} ST	100	5	on	3.86	0.772	23.8
C2	KW	10^{-2} ST	100	5	on	3.68	0.736	17.4
C3	$10^{+1}KW$	10^{-2} ST	100	5	on	3.29	0.658	28.7
D1	$10^{+0.5}KW$	10^{-2} ST	40	5	on	0.84	0.168	9.8
D2	$10^{+0.5}KW$	10^{-2} ST	60	5	on	1.31	0.262	10.1
D3	$10^{+0.5}KW$	10^{-2} ST	80	5	on	2.14	0.428	11.9
E1	$10^{+0.5}KW$	ST	100	5	on	1.88	0.376	11.0
E2	$10^{+0.5}KW$	10^{-1} ST	100	5	on	2.53	0.506	11.9
E3	$10^{+0.5}KW$	10^{-3} ST	100	5	on	4.42	0.884	19.8
E4	$10^{+0.5}KW$	10^{-4} ST	100	5	on	5.33	1.066	17.9
F1	$10^{+0.5}KW$	10^{-2} ST	100	2.5	on	2.87	1.148	9.2
F2	$10^{+0.5}KW$	10^{-2} ST	100	7.5	on	3.83	0.510	20.8
F3	$10^{+0.5}KW$	10^{-2} ST	100	10	on	4.16	0.416	29.1

Table 4.3: *Model parameters*

viscosity and the temperature plots, an eventually horizontally subducted slab is clearly recognized. The subduction velocity gradually lowers from 5 to 3 cm/yr within the first 20 Ma due to increasing friction along the increasing plate contact zone. Time averaged values of the different models for the first 20 Ma are presented in Table 4.3 to quantify the subduction velocity. These subduction velocities are computed as horizontal velocities of the stiff oceanic plate just before subduction.

4.4.1 The influence of the fault locking depth on subduction

The mechanical coupling on the lithospheric fault is defined by a relation between the local slip velocity along the fault and the local fault shear stress, resisting the slip on the contact plane. The coupling behavior is controlled by the spatially variable stiffness S, as defined in Equation (4.7). We set the fault locking depth to 40, 60, 80 or 100 kms depth. Table 4.3 gives the time averaged subduction velocities for each of the experiments, listed as cases D1 to D3 and model A, respectively. In Figure 4.3a, the resulting subduction rates are plotted against fault locking depth. At depths larger than the locking depth, the deformation is taken over by the crustal layer, which is relatively weak and acts as a lubricant. When the unlocked part of the fault is shortened, the length of the crustal shear zone increases. This increases the total resistance against subduction and decreases the subduction velocity. Figure 4.3b shows vertical cross sections of several physical
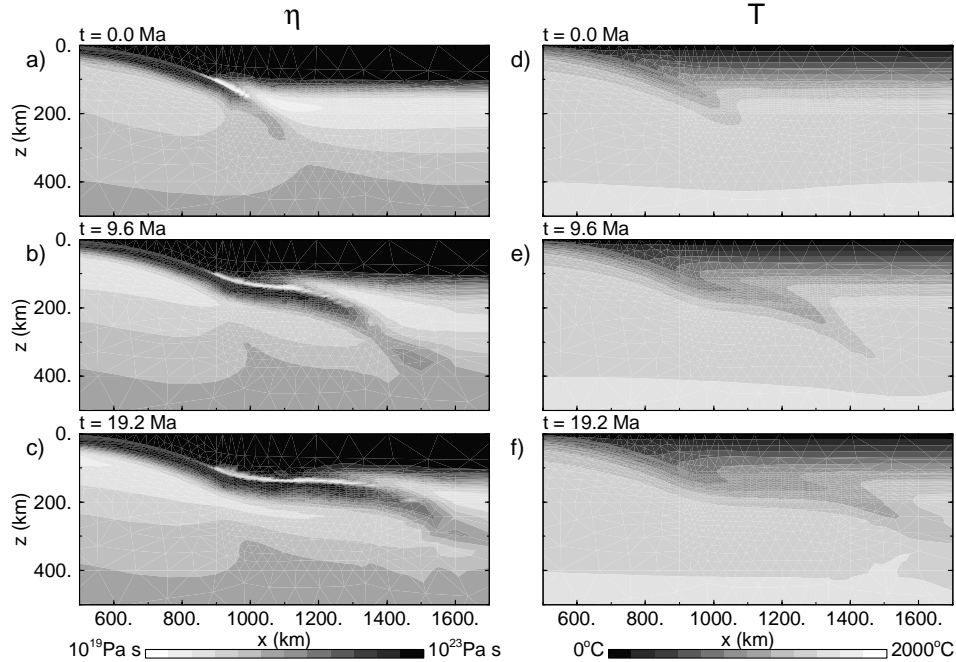
Figure 4.2: *Viscosity (logarithmic contours) and temperature of reference model A. Three time snapshots at t=0 (top panel), 9.6 and 19.2 Ma (bottom panel) since the onset of obduction are shown. The oceanic plate subducts horizontally, creating a doubled lithosphere of increasing horizontal length.*

quantities at $x = 800$ km (through the subduction zone) and $t = 9.6$ Ma, which clarify the effects of changing the fault depth. Figure 4.3b1 shows that for shallow fault locking depths, the velocity increase from continent to slab mainly occurs gradually within the 7 km thick oceanic crust. The models with deeper fault locking depth, however, have the total velocity jump concentrated at the fault above the crust. This fault coupling depth influences the effective viscosity of the crust, as shown in Figure 4.3b3.

4.4.2   The influence of the crustal strength on subduction

In further experiments, the fault coupling depth z_L is kept constant at 100 km depth. The influence of the intrinsic crustal strength was investigated by varying the prefactor A in Equation (4.5), relatively to the value from Table 4.2. Different model calculations are listed as cases E1 to E4 and case A in Table 4.3. The crustal viscosity is approximately proportional to $\Delta B = \Delta A^{-1/n}$. Figures 4.4a and 4.4b1 show that the subduction rate strongly depends on the viscosity of the crustal layer. Variation of A of four orders of magnitude, used in this experiment, can be related to the variations in degree of hydration
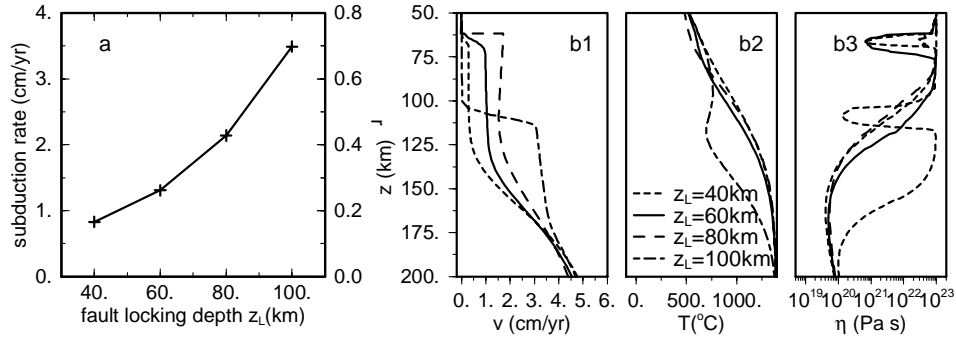
Figure 4.3: *a) Subduction rate changes and ratio r are plotted for a variation in the fault locking depth. b) Vertical profiles at $x = 800$ km (in the middle of the subduction zone) at $t = 9.6$ Ma show the effect of the changing fault depth on b1) the horizontal velocity component v, b2) the temperature field T and b3) the effective viscosity η.*

of the subducting oceanic crust. A measure of the effectiveness of obduction is defined through the ratio of the subduction rate and the overriding plate velocity $r = v_{\mathrm{subd}}/v_{ov}$. Corresponding values of r are given in Figures 4.3a and 4.4a and in Table 4.3.

4.4.3   The influence of the mantle rheology on subduction

The mantle rheology is probably not known more accurate than order-of-magnitude precision. It is therefore worthwhile to examine the influence of variations in the mantle strength on the subduction behavior. We varied the mantle viscosity in cases C1 to C3 and case A from Table 4.3 through changes in the prefactors A of both diffusion and dislocation creep laws in equation (4.5), relatively to the values from Table 4.2. Resulting subduction rates, temperature profiles and effective viscosity are shown in Figure 4.5. Subduction rates increase moderately with increasing mantle strength. For the strongest mantle, the subducting lithosphere couples best to the mantle below since the asthenosphere is then least pronounced. This prevents the subducting plate from colliding and being pushed along with the overriding plate and therefore results in the highest subduction rates. The drag of the oceanic plate with the mantle below in these models is therefore necessary for subduction to occur. This is opposite to the situation in Benioff subduction, in which the mantle drag usually is thought to resist the subduction process. For the reference model A, the ratio of diffusion creep viscosity over dislocation creep viscosity is shown in Figure 4.6. The high values of the ratio in the strong lithosphere and surrounding (including the asthenosphere) are indicative of local predominance of dislocation creep flow over the diffusion creep component. This indicates that the change in dislocation creep strength is most important here. Diffusion creep governs the mantle strength at greater depths, which is in line with (Karato and Wu, 1993). Another feature that is at least partly controlled by mantle strength is the ability of the overriding plate to
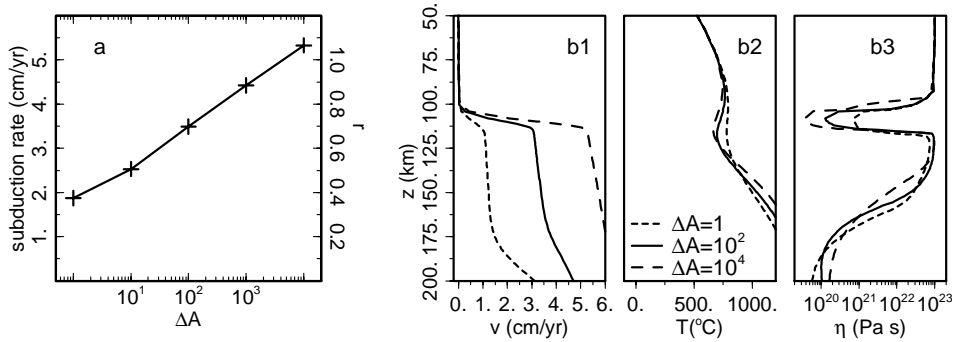
Figure 4.4: *a) Subduction rates and velocity ratio r are plotted for different values of the crustal viscosity prefactor ΔA relative to the prefactor from Table 4.2. b) Vertical profiles behind the subduction zone ($x = 920$ km) at $t = 9.6$ Ma show the effect of a changing crustal flow law prefactor on b1) the horizontal velocity component v, b2) the temperature field T and b3) the effective viscosity η.*
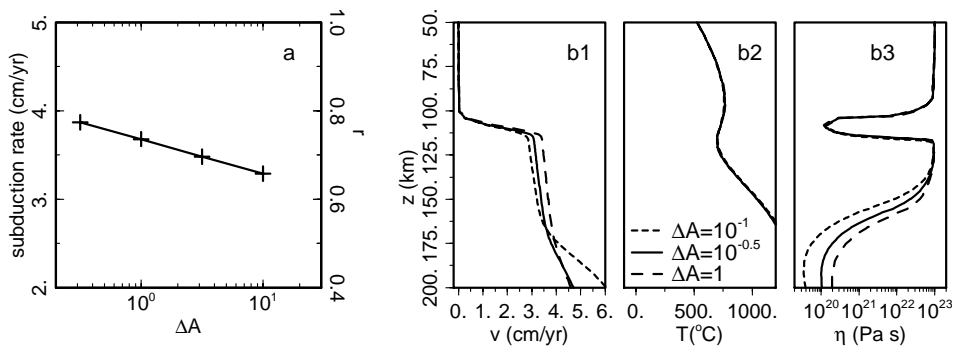
Figure 4.5: *Similar to Figure 4.4 for different values of the mantle viscosity prefactor ΔA, relative to the prefactors for diffusion and dislocation creep from Table 4.2.*

avoid the slab from subducting further to the deep mantle (Benioff type of subduction). The mantle will be able to support the (small) weight of the young slab only when it has enough strength to resist the necessary deformation involved. If not, the slab will subduct further, once asthenospheric material is able to penetrate in between the two lithospheres. Such an event occurred in model C3 with a relatively weak mantle and is shown in Figure 4.7. Non-linear rheology, in combination with viscous heating weakened the slab during bending and caused slab detachment.

Figure 4.6: *The logarithmic ratio of diffusion creep viscosity over dislocation creep viscosity for the reference model A at $t = 9.6$ Ma indicates that dislocation creep is the main deformation mechanism in and near the lithospheres, while at deeper levels, diffusion creep becomes dominant.*

4.4.4 The role of viscous heating in the subduction process

We compared the results from two models, listed as cases A and B in Table 4.3, for calculations with and without viscous heating, respectively. The time av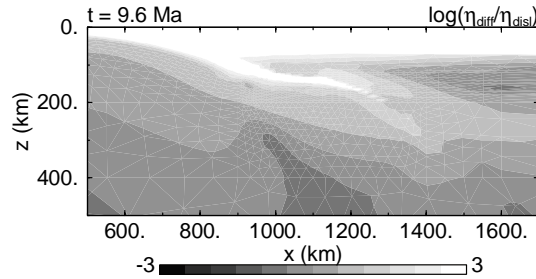eraged subduction velocity is 2.81 cm/yr for model B and increases to 3.49 cm/yr for model A. Figure 4.8 shows vertical cross sections of the relevant physical quantities for both models A and B, again at $x = 920$ km for $t = 9.6$ Ma. Viscous dissipation heats the crustal layer, as shown in Figure 4.8b, where most of the shear deformation occurs. This results in a decrease of effective crustal viscosity of half an order of magnitude, as shown in Figure 4.8c, due to both the temperature and the strainrate dependence of the viscosity. These effects enhance mechanical decoupling resulting in an increase of the subduction rate.

4.4.5 Relation between subduction velocity and overriding plate velocity

In the previous experiments, a constant velocity of the overriding plate $v_{ov} = 5$ cm/yr was used. In models F1 to F3 (Table 4.3), we varied the overriding velocity between 2.5 and 10 cm/yr to examine its effect on the subduction behavior. Figure 4.9 indicates a convergence rate increasing with increasing overriding plate velocity. This relation is non-linear: an increasing overriding velocity leads to a larger shear, which in turn results in lower dislocation creep strength and more shear heating. This causes a more pronounced asthenosphere with less coupling between the mantle and subducting plate and a less effective obduction, as indicated through the lower velocity ratio r in Table 4.3.
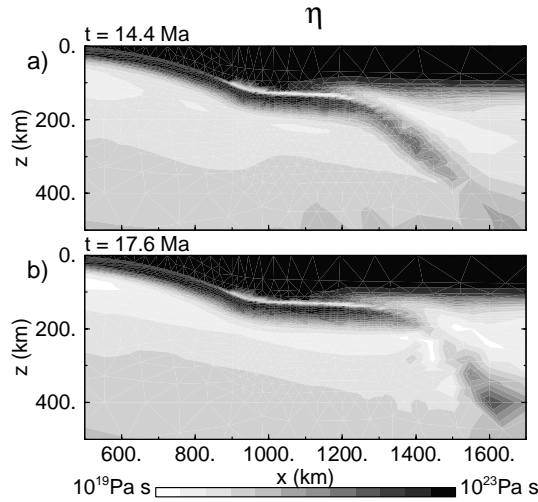
Figure 4.7: *Viscosity plot for model C3 for time $t = 14.4$ and $t = 17.6$ Ma, in which the subduction of the slab through a relatively weak mantle is shown. Non-linear rheology and viscous heating lead to the detachment of slab in the bending area.*

4.5   Discussion

In our model, the overriding plate provides a driving mechanism for young oceanic plates to subduct, thereby constantly performing work on the system. In our model, the corresponding work per unit time, or power, is introduced through the velocity boundary conditions that describe the relative motion between continent and deep mantle. Validation of the model by an estimate of this additional work is necessary (Han and Gurnis, 1999). We make an estimate of this power input by assuming that the dissipated energy of the model is provided mainly by the imposed boundary conditions (external energy source), since the potential energy release is small for a young oceanic plate that subducts only to a depth of about 120 km, as is the case in our models. The time averaged generated power of viscous heating of the reference model is 14.1×10^3 W/m. In case Benioff subduction occurs (as in model C3, table 4.3), this value becomes larger, because in that case the release of potential energy by the sinking slab becomes significant. In case of a stronger mantle (models C1 and C2, table 4.3), this value increases as well: the asthenosphere is less pronounced and the involved overriding shear stress increases. This suggests that the estimated work done by the overriding continent per unit time puts a constraint on the mantle strength in this model. If we assume the overriding continent to be driven by forces of the same order of magnitude as ridge push ($\approx 2 \times 10^{12}$ N/m), a corresponding estimate of the amount of work per unit of time done by a five-cm-per-year overriding continent on the system is $3 - 4 \times 10^3$ W/m. These values, however may be larger when besides young subduction also older slabs subduct at the same subduction zone in a 3-D
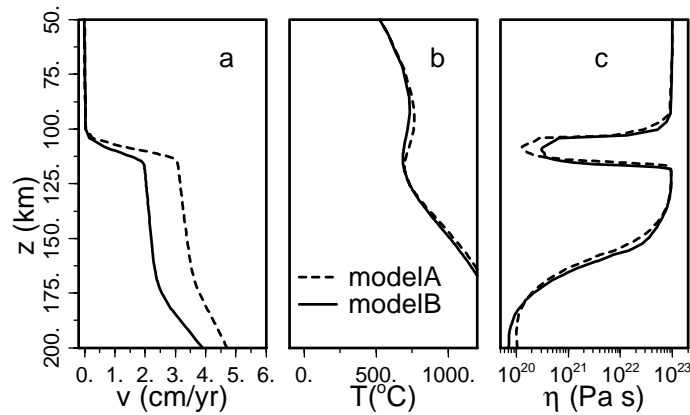
Figure 4.8: *Vertical profiles at $x = 920$ km for $t = 9.6$ Ma for a model with viscous dissipation (A) and without (B). Shown are horizontal velocity, temperature and effective viscosity.*

configuration, in which case the pulling force of slab roll back may contribute considerably. This may for example be the case at the west coast of South America (Gutscher et al., 1999a). These estimates show, that the power, introduced by the velocity boundary conditions are probably of the correct order of magnitude.

Although here the emphasis is put on the significance of the rheology for shallow flat subduction, another important model parameter is the buoyancy of the slab. A heavy slab will be able to subduct steeply more easily than a buoyant one. The buoyancy of the slab is influenced by the age of the slab, the stratigraphy of the oceanic plate and the series of phase transitions from basalt to eclogite (Hacker, 1996). These aspects of the subduction process are subject of further research.

4.6   Concluding remarks

We have performed numerical model experiments for a passive oceanic lithosphere that is overridden by a continent. We varied the physical parameters that influence the friction between the two converging plates. This influence is clearly expressed in the ratio of the subduction velocity over the overriding plate velocity. We modeled a subduction fault that partly decouples the plates, as well as a crustal layer with a rheology that is significantly weaker than the mantle rheology. Both the crustal strength and locking depth of the fault influence the subduction rate significantly. The mantle strength must be large enough to fix the overridden oceanic plate to the underlying mantle and to prevent steep Benioff type subduction to develop. However, the mantle cannot be too viscous in view of the limited driving force of the overriding plate. In the model calculations, viscous heating turned out to be a significant factor facilitating subduction. Non-linear dislocation creep
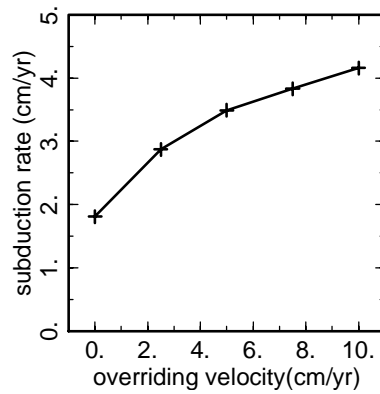
Figure 4.9: *The relation between the overriding and subduction velocities. The relation is non-linear, due to the non-linear dislocation creep strength: a larger strainrate leads to a lower viscosity in the asthenosphere.*

included in our composite rheological model appears to be important in weakening the shallow subducting crust and mantle, whereas in the deeper parts linear diffusion creep is dominant, in line with predictions from (Karato and Wu, 1993). The ratio of subduction and overriding velocity was shown to depend non-linearly on the overriding velocity due to the presence of mantle powerlaw creep. In conclusion: from numerical experiments, we have found active obduction of oceanic lithosphere by an overriding continent to be a viable mechanism for shallow flat subduction over a wide range of parameters.

Chapter 5

Latent heat effects of the major mantle phase transitions on low-angle subduction

Abstract

Very low to zero shallow dip angles are observed at several moderately young subduction zones with an active trenchward moving overriding plate. We have investigated the effects of latent heat for this situation, where mantle material is pushed through the major mantle phase transitions during shallow low-angle subduction below the overriding plate. The significance of the buoyancy forces, arising from the latent heat effects, on the dynamics of the shallowly subducting slab is examined by numerical modeling. When a 32-Ma old slab is overridden with 2.5 cm/yr by a continent, flat subduction occurs with a 4 to 5 cm/yr convergence rate. When latent heat is included in the model, forced downwellings cause a thermal anomaly and consequently thermal and phase buoyancy forces. Under these circumstances, the flat slab segment subducts horizontally about 350 km further and for about 11 Ma longer than in the case without latent heat, before it breaks through the 400-km phase transition. The style of subduction strongly depends on the mantle rheology: increasing the mantle viscosity by one order of magnitude can change the style of subduction from steep to shallow. Similarly, an overriding velocity of less than 1 cm/yr leads to steep subduction, which gradually changes to flat subduction when increasing the overriding velocity. However, these model parameters do not change the aforementioned effect of the latent heat, provided that low-angle subduction occurs. In all models latent heat resulted in a substantial increase of the flat slab length by 300 to 400 km. Varying the olivine-spinel transition Clapeyron slope γ from 1 to 6 MPa/K reveals a roughly linear

relation between γ and the horizontal length of the slab. Based on these results, we conclude that buoyancy forces due to latent heat of phase transitions play an important role in low-angle subduction below an overriding plate.

5.1   Introduction

It has long been recognized that the major mantle phase transitions influence the dynamics of subducting slabs (Turcotte and Schubert, 1982; Christensen and Yuen, 1985; Tackley et al., 1994; Riedel and Karato, 1997; Schmeling et al., 1999). Due to opposing signs of the Clapeyron slopes, cold slabs are accelerated through the 410-km transition, but are retarded or even trapped at the 670-km transition. Latent heat due to these phase transitions gives only a second-order effect, because the cold thermal anomaly of the slab overshadows the temperature change from latent heat release or absorption. During shallow flat subduction, a cold slab does not (initially) penetrate the phase transitions, but instead travels (sub)horizontally. Flat subduction of relatively young oceanic (< 50 Ma) lithosphere is observed in about 10% of the modern subduction zones and is, for example, observed today below the Peru and Central Chile (Wortel and Vlaar, 1978; Gutscher et al., 2000b). In case of shallow flat subduction below a trenchward moving overriding continent (Vlaar, 1983; van Hunen et al., 2000), relatively warm mantle material below the subducting plate is pushed through the phase transitions. In such case, latent heat forms a first order effect of the phase transition, because of the absence of a cold thermal anomaly at the depth of the phase transition. Latent heat release at the 400-km transition results in a temperature rise, which depresses the phase plane to greater depth. The resulting thermal and phase buoyancy will resist further downward motion of mantle material. In this paper, we examine the effects of latent heat under such circumstances. Relevant model parameters are varied to test the robustness of the observed features.

5.2   Effects of latent heat

When a steeply subducting slab passes the 400-km phase transition, latent heat is released, which heats up the cold slab and reduces its gravitational instability. In general, the temperature rise due to this latent heat release is small: the slab still remains relatively cold (Figure 5.1a). However, when material with a very small or absent thermal anomaly passes the phase transition, latent heat results in a first order buoyancy effect, which may be decisive in maintaining marginal stability in systems with flat subduction. Since the material at the depth of the phase transition is not gravitationally instable, it must be forced to pass the transition. This is the case when a continent overrides a subducting oceanic plate, by which mechanism the oceanic plate is brought to a depth of at least 100 to 150 km. This subducting plate, in turn, pushes underlying mantle material down through the phase transitions at greater depth. At the 400-km transition, the released latent heat results in both a thermal buoyancy force and a *depression* of the equilibrium position of the phase transition, which results in a positive phase buoyancy contribution (Figure 5.1b). These
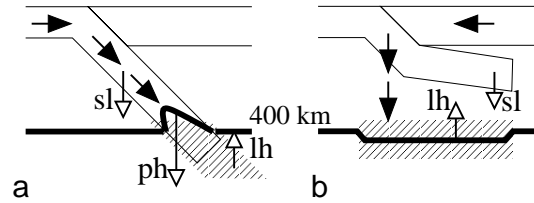
Figure 5.1: *Schematic representation of the buoyancy effects of latent heat release around 400-km depth during subduction. In the shaded area, the release or advection of latent heat affects the temperature. The thick solid line schematically represents the depth of the 400 km phase transition. Solid arrows denote the flow field, open arrows represent the local buoyancy forces: sl= slab thermal buoyancy, ph= slab phase buoyancy, lh= total latent heat buoyancy. a) During steep Benioff subduction, the thermal anomaly of the cold slab eclipses the latent heat effect. b) In case of low-angle subduction below a trenchward moving overriding plate, latent heat release gives a first-order buoyancy effect of the phase transition.*

buoyancy contributions can influence the dynamics above the transition, since they tend to resist further downwellings. We can make a rough estimation of these effects. The latent heat release per unit mass of mantle material equals (Christensen, 1998)

$$Q_L = \gamma \delta \rho T / \rho^2 \qquad\qquad (5.1)$$

where parameters are defined in Table 5.1.

Symbol	Meaning	Value used	Dimension
A	Pre-exponential flow law parameter		
	crustal dislocation creep value	8.8×10^{-25}	$\mathrm{Pa^{-n}\,s^{-1}}$
	reference mantle diffusion creep value[a]	1.92×10^{-11}	$\mathrm{Pa^{-n}\,s^{-1}}$
	reference mantle dislocation creep value[a]	2.42×10^{-16}	$\mathrm{Pa^{-n}\,s^{-1}}$
C	Composition parameter	—	—
c_p	specific heat	1250	$\mathrm{Jkg^{-1}K^{-1}}$
Di	Dissipation number $= \alpha g h / c_p$	0.47	—
E^*	activation energy		
	crustal dislocation creep value[b]	260×10^3	$\mathrm{J\,mol^{-1}}$
	reference mantle diffusion creep value[a]	300×10^3	$\mathrm{J\,mol^{-1}}$
	reference mantle dislocation creep value[a]	540×10^3	$\mathrm{J\,mol^{-1}}$
H	non-dimensional radiogenic heat production	—	—
n	viscosity stress exponent		
	crustal dislocation creep value[b]	3.4	—
	reference mantle diffusion creep value[a]	1.0	—
	reference mantle dislocation creep value[a]	3.5	—
Q_L	Latent heat release across a phase transition	—	$\mathrm{J\,kg^{-1}}$
R	gas constant	8.3143	$\mathrm{J\,K^{-1}\,m^{-3}}$

Table 5.1: *Notations*

Sources: [a]*(Karato and Wu, 1993);* [b]*(Shelton and Tullis, 1981);* [c]*(Karato and Rubie, 1997);* [d]*(Bina and Helffrich, 1994);* [e]*(Steinbach and Yuen, 1995)*

Symbol	Meaning	Value used	Dimension
Ra	Thermal Rayleigh number $\rho\alpha\Delta T h^3/\eta\kappa$	1.8×10^7	—
Rb	Phase Rayleigh number $\delta\rho g h^3/\eta\kappa$		
	400-km phase transition	2.1×10^7	—
	670-km phase transition	2.4×10^7	—
Rc	Compositional Rayleigh number $\Delta\rho_c g h^3/\eta\kappa$		
	basalt	3.1×10^7	—
	harzburgite	6.0×10^6	—
T	non-dimensional temperature	—	—
T_0	non-dimensional surface temperature	$273/\Delta T$	—
ΔP	non-dimensional hydrodynamic pressure	—	—
ΔT	temperature contrast across model domain	2300	K
t	non-dimensional time	—	—
$\mathbf{u}$	non-dimensional velocity $\mathbf{u} = (v, w)^T$	—	—
w	downward vertical velocity component	—	—
V^*	activation volume		
	crustal dislocation creep value	10×10^{-6}	$\mathrm{m^3 mol^{-1}}$
	reference mantle diffusion creep value	4.5×10^{-6}	$\mathrm{m^3 mol^{-1}}$
	reference mantle dislocation creep value[c]	14×10^{-6}	$\mathrm{m^3 mol^{-1}}$
v_0	overriding velocity (reference model value)	2.5	$\mathrm{cm\, yr^{-1}}$
α	thermal expansion coefficient	3×10^{-5}	$\mathrm{K^{-1}}$
Γ_k	harmonic phase functions for all k mantle phase transitions	—	—
γ_{400}	Clapeyron slope 400 km phase transition[d]	3	$\mathrm{MPaK^{-1}}$
γ_{670}	Clapeyron slope 670 km phase transition[d]	-2.5	$\mathrm{MPaK^{-1}}$
$\Delta\rho_c$	compositional density relative to mantle material		
	basalt	-400	$\mathrm{kg\, m^{-3}}$
	harzburgite	-77	$\mathrm{kg\, m^{-3}}$
δT	temperature increase due to latent heat release	—	K
δz	phase transition deflection due to latent heat release	—	m
$\delta\rho_{400}$	density difference across the 400 km phase transition[e]	273	$\mathrm{kg\, m^{-3}}$
$\delta\rho_{670}$	density difference across the 670 km phase transition[e]	342	$\mathrm{kg\, m^{-3}}$
$\dot\epsilon_{ij}$	$\dot\epsilon_{ij} = \partial_j u_i + \partial_i u_j$ = strainrate tensor	—	$\mathrm{s^{-1}}$
η	non-dimensional viscosity	—	—
Φ	non-dimensional viscous dissipation	—	—
ρ	mantle density	3416	$\mathrm{kg\, m^{-3}}$
τ_{ij}	deviatoric stress tensor	—	Pa
τ	2nd invariant of the stress tensor τ_{ij}	—	Pa

Table 5.1: *Notations (continued)*

Clapeyron slopes are taken from (Bina and Helffrich, 1994). Neglecting thermal diffusion, an estimate of the resulting temperature rise is given by $\delta T = Q_L/c_p$, while the

phase change equilibrium depression is described by:

$$\delta z = \gamma \delta T / \rho g \qquad (5.2)$$

For a mantle temperature $T = 1728$ K at 400 km depth and parameter values as in Table 5.1, we obtain a temperature rise $\delta T = 100$ K due to latent heat release. Such a temperature rise would depress the phase transition by approximately $\delta z = 9$ km. We assume a depth increase of all mantle material of 100 km due to the overriding effect of a continent of such thickness. Forcing a 100 km thick vertical column of mantle material with unit cross section through the 400-km transition would reduce its weight relative to a column without vertical movement and would approximately result in a latent heat buoyancy force $F_{lh,400} = 3.4 \times 10^7 \text{N/m}^2$ due to both thermal and phase buoyancy effects of the latent heat release. This estimate of the latent heat effect represents an upper bound for two reasons. First, resistance of mantle downwellings because of the latent heat forces will have a negative feedback on these forces, since less latent heat is released. Second, thermal diffusion will spread the (local) temperature increase, which will diminish the depression of the phase transition.

For comparison, we estimated the thermal and phase buoyancy for a 32-Ma-old slab, before and during the breakthrough at the 400-km transition. We assume a cooling half-space description of the oceanic lithosphere and vertically integrate the resulting density profile with respect to the mantle adiabat (Turcotte and Schubert, 1982) to obtain the negative thermal slab buoyancy F_{sl} of a lithospheric plate just prior to subduction. Assuming the model parameters from Table 5.1, we obtain $F_{sl} = -4.7 \times 10^7 \text{N/m}^2$, where the minus-sign indicates a downward force. F_{sl} diminishes as the slab heats up during the (sub)horizontal subduction process. If the slab finally reaches the 400 km transition, the negative phase buoyancy of the uplifted transition within the cold slab will start to contribute. Using $\Delta T = -700$ K in the cold interior of the slab, Equation 5.2 would give an uplift of the phase transition of 63 km, and with the parameters from Table 5.1 this gives a negative phase buoyancy force $F_{ph} = -16.8 \times 10^7 \text{N/m}^2$.

Latent heat is absorbed when material is pushed down through the 670 km phase transition, which gives a negative thermal buoyancy. The phase transition's equilibrium depth, however, is depressed and this gives again a positive phase buoyancy. Thermal and phase buoyancy counteract each-other for this phase transition and the total buoyancy effect of this phase transition will be smaller than that for the 400-km phase transition, but still positive, since the phase buoyancy will be dominant. Applying the same method as for the 400 km phase transition and using a mantle temperature $T = 1908$ K at 670 km depth and parameter values as in Table 5.1 results in a total positive latent heat buoyancy force $F_{lh,670} = 1.8 \times 10^7$ N. Comparison of the combined effects of the positive $F_{lh,400}$ and $F_{lh,670}$ with the negative F_{sl} shows that during low-angle subduction below a trenchward moving continent, the total buoyancy effect of the latent heat is of similar magnitude as the negative thermal slab buoyancy. Only if the slab eventually reaches the 400-km transition, the negative F_{ph} will start to dominate the other buoyancy forces, which may result in a flushing event and steeper subduction. How the latent heat would affect the path of the (sub)horizontal slab above the transition is not easily estimated. Vertical motion of the shallow slab and the deeper mantle material around the phase transitions are indirectly

coupled by the viscous deformation of intermediate mantle material. Due to the larger distance between slab and transition, the effects of latent heat on shallow flat subduction will be smaller for the 670-km phase transition than for the 400-km phase transition. In order to assess these effects quantitatively, we use numerical modeling and vary the controlling parameters.

5.3   Model description

The subduction model is based on the extended Boussinesq formulation for an incompressible fluid of infinite Prandtl number (Ita and King, 1994). We give a brief description of the governing equations and applied rheology. A more elaborate description is given in (van Hunen et al., 2000). We solve the continuity and momentum equation to obtain the motion of the slab through the mantle below an overriding continent:

$$\partial_j u_j = 0 \tag{5.3}$$

$$\partial_j(\eta \dot{\epsilon}_{ij}) - \partial_i \Delta P = (RaT - \sum_k Rb_k \Gamma_k + RcC)\delta_{iz} \tag{5.4}$$

Thermal, compositional, and phase buoyancy, as well as temperature dependent rheology are accounted for through coupling with the conservation equations for energy and composition:

$$\frac{\partial T}{\partial t} + u_j \partial_j T - Di(T + T_0)w - \sum_k \gamma_k \frac{Rb_k}{Ra} Di(T + T_0)\frac{d\Gamma_k}{dt} - \partial_j \partial_j T$$

$$= \frac{Di}{Ra}\Phi + H \tag{5.5}$$

$$\frac{\partial C}{\partial t} + u_j \partial_j C = 0 \tag{5.6}$$

Symbols are defined in Table 5.1. The buoyancy and latent heat effects of the mantle phase transitions are described by the terms with Γ_k in Equations 5.4 and 5.5, respectively (Ita and King, 1994), in a summation of the effects of the 400-km and 670-km phase transitions. Here, we model the subduction of a relatively young lithosphere (~ 32 Ma). Based on results from (Kirby et al., 1996b) and (Schmeling et al., 1999), we conclude that olivine meta-stability below the 400-km phase transition is negligible in our model, due to the relatively high slab temperature. Therefore, we do not include olivine metastability in our models. Equations 5.3 to 5.5 are solved with a code that is based on the finite element package Sepran (Segal and Praagman, 2000), which is combined with a Lagrangian tracer particle method to solve Equation 5.6. Compositionally, the model distinguishes between two types of mantle material (undepleted lherzolite and depleted harzburgite) and crustal material and each has its own compositional buoyancy, defined through the compositional Rayleigh number Rc, as defined in Table 5.1. For all mantle material, the same composite rheology is applied, which combines both Newtonian and non-Newtonian creep (van den

Berg et al., 1993; van den Berg and Yuen, 1996). Crustal rheology is described by non-Newtonian creep. Each creep mechanism is prescribed by an Arrhenius relation:

$$\dot{\epsilon}_{ij} = A\tau^{n-1}\tau_{ij} \exp\left[-\frac{E^* + PV^*}{RT}\right] \tag{5.7}$$

Symbol definition and used reference model values are defined in Table 5.1. Besides a constant maximum viscosity $\eta_{max} = 10^{23}$ Pa s, an additional stress limiting rheology is applied here, which assumes that material yield when the second invariant of the stress exceeds a pressure dependent stress limit σ_y (Schott and Schmeling, 1998; Trompert and Hansen, 1998).

We model the subduction process in a Cartesian box of 2000 km deep and 3800 km wide. Our model reference frame is fixed to the overriding continent, such that in this reference frame the subducting plate and underlying mantle move towards this continent. The reference frame of a subduction zone is usually fixed to the deep mantle. For reasons of computational convenience, we model the subduction below a trenchward-moving overriding plate in a reference frame that is fixed to this overriding plate: an overriding plate velocity $(v_0, 0)$ is modeled with a no-slip condition at the earth's surface for the overriding plate and a velocity boundary condition $(-v_0, 0)$ at the left hand side and bottom boundaries are imposed. The subducting plate has a free-slip boundary condition, while horizontal flow and a lithostatic pressure are prescribed on the right hand side boundary. Temperature boundary conditions are a mantle adiabat (potential temperature $T_{pot} = 1300^o$ C) at the left hand side and bottom boundary, $T = 0^o$C at the surface and a continental geotherm on the right hand side boundary. In between the converging plates, a curved free-slip fault extends to a depth of 100 km. For all model calculations, a single initial situation was created by kinematically driving the subduction of a 32 Ma slab for a duration of 8 Ma, such that the tip of the slab just enters the asthenosphere. After this initial stage, the subduction velocity is no longer prescribed, but driven by internal buoyancy forces in combination with the effects of the overriding plate. The initial mantle has an adiabatic temperature profile below the cool lithospheric plates. Model setup, fault implementation and initial conditions are described in more detail in (van Hunen et al., 2000), and the same model parameters are taken, unless explicitly reported.

The effect of a basalt-to-eclogite phase transition in the subducting oceanic crust has been approximated by applying a transition of the compositional buoyancy of crustal material at a depth of 50 km. Temperature dependence of this transition is neglected by setting the Clapeyron slope to zero. Below the 7-km thick oceanic crust, an 18-km thick harzburgitic layer is present. The relative compositional density of basalt and harzburgite with respect to undepleted mantle material in the model are -400 and -77 kg/m^3, respectively. Furthermore, we assume that oceanic compositional buoyancy terms of eclogite and harzburgite cancel eachother with respect to undepleted mantle material within a lithospheric column. Therefore, no net compositional buoyancy is applied in our model below 50 km depth. Within the shallow subduction zone, the converging plates are probably decoupled by a fault gouge and a weak basaltic crust. However, for the decoupling of the deeper parts of the two converging plates, several alternative mechanisms have been proposed: eclogite being equally weak as basalt, decoupling within the subducting

sediment layers, incomplete dehydration or eclogitisation occurring as deep as 250 km (Abers, 2000) or the mantle material overlying the hydrated subducting crust altering to weak serpentinite and talc (Peacock and Hyndman, 1999). To obtain mechanical decoupling between the converging plates, we applied a weak crustal rheology above a depth of 200 km and, for numerical convenience, used the stronger mantle rheology for all materials below this depth. Di-variant mantle phase transitions are included in the model for the 400-km and 670-km discontinuity. These discontinuities are suggested to be as sharp as 4 km (Benz and Vidale, 1993). However, as long as the phase transition width is smaller than about 40 km, our model results show little dependence on this width. For numerical convenience, we used a 20-km wide harmonic parameterization of the phase functions Γ_k for both transitions.

5.4   Numerical results

For the set of experiments in this section, we defined a reference model as discussed in section 5.3 with reference parameter values as given in Table 5.1. The effects of latent heat of the two mantle phase transitions on the subduction are investigated. Figure 5.6 shows snapshots of the model evolution with and without included latent heat. The results of the model without latent heat (Figure 5.6a,b,c) show a slab which subducts with a small angle and reaches the 400-km phase transition after approximately 14 Ma with an average convergence rate of 4.6 cm/yr. Corresponding results for a model including latent heat (Figure 5.6d,e,f) show a dip angle of the slab reaching zero degrees and a slab traveling horizontally over a longer distance. This slab reaches the transition after approximately 25 Ma with an average convergence rate of 4.1 cm/yr. The black arrows show the direction and amplitude of the mantle flow with respect to the overriding plate. These arrows demonstrate that the breakthrough, which occurs when the slab reaches the 400-km transition, is less vigorous in the model with latent heat. This is due to the extra heating of the slab during its longer route from trench to transition, which reduces the transition uplift. The effects of the latent heat release at the 400-km transition are visualized in Figure 5.6g,h,i, showing the area around 400 km depth with a vertical exaggeration. The plot shows the contours of the temperature field, relative to the situation at $t = 0$ Ma and gives a good impression of the latent heat release due to the overriding plate, together with the resulting (vertical exaggeration of the) phase transition depression.

   Figure 5.2 shows the effects of the latent heat release/absorption for both phase transitions from the start of the model at $t = 0$ Ma until the moment when the slab reaches the 400-km transition. Figure 5.2a gives the maximum temperature change around the transitions with respect to the initial situation, while Figure 5.2b shows the corresponding maximum phase equilibrium depressions. Figure 5.2a shows a maximum temperature rise of 70 to 80 K for the 400-km transition, while near the 670-km transition, the temperature drop is only about 20 K. In Figure 5.2b, the resulting shift of the equilibrium depth the transitions show a similar trend: the 400-km transition is depressed by 8 km, while the 670-km transition shifts only 2 to 3 km downwards. As expected, these effects are smaller than the ones obtained from the theoretical estimate in section 5.2. This is due to the ther-
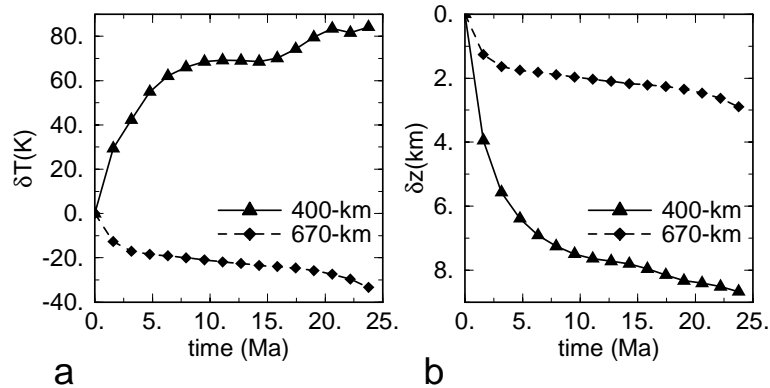
Figure 5.2: *Evolution of maximum temperature change δT (a) and phase transition depression δz (b) for both mantle phase transitions due to latent heat release/absorption of the downward penetrating mantle material. Both effects are roughly four times larger for the 400-km phase transition than for the 670-km one.*

mal diffusion of the latent heat and a reduced vertical flow from the slab to the transitions because of the viscous deformation of the mantle in between. The measured perturbations are stronger at the 400-km transition, because it is situated closer to the subducting plate. Furthermore, the influence of the slab on the 670-km transition is partly shielded off by the 400-km transition, which results in a larger flux of mantle material through the 400-km transition. After 10 to approximately 15 Ma, the maximum temperature rise due to the latent heat release of the 400-km transition remains fairly constant at about 70 K, because latent heat production is in equilibrium with thermal diffusion. After 15 Ma, the slab is attracted by the 400-km transition, neighboring mantle material is accelerated downwards and the effects of latent heat again dominates thermal diffusion. The effects of the accelerating slab motion on the 670-km transition is less direct and not clearly observable in Figure 5.2a, b.

The robustness of the latent heat effects is tested through variation of several model parameters. As an indicator of the latent heat effect, we estimated the length of the flat slab segment below the overriding continent. The horizontal position of the point of penetration of the slab through the 400-km transition was used to quantify this segment length. The importance of trench migration and the mantle viscosity on ability of the slab to penetrate into the lower mantle has been shown by Christensen (1996) and Olbertz et al. (1997). In previous work we have shown that mantle viscosity is also a key parameter for the occurrence of shallow flattening of the slab at a depth of about 100 km (van Hunen et al., 2000): during a trenchward motion of the overriding plate, a strong mantle resists steep Benioff type subduction. Furthermore, viscosity controls the interaction between vertical slab motion and flux of mantle material through the 400-km transition. We varied the effective mantle viscosity through variation of the viscosity prefactors A in

Equation 5.7, around the reference values from Table 5.1, of both the diffusion and dislocation creep components of the composite rheology. The relationship between A and the effective viscosity η is dependent on the local circumstances for a composite rheology (van Hunen et al., 2000): with the rheological parameters from Table 5.1, a one order-of-magnitude *decrease* of A results in an effective viscosity *increase* with a factor between 2 and 10. Figure 5.3 shows the effect of the prefactor variation ΔA with respect to the
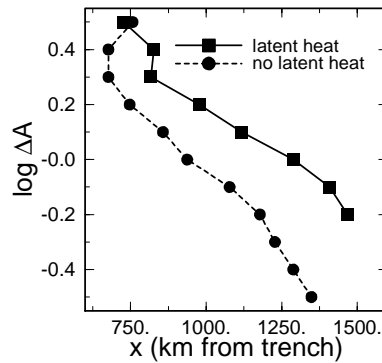

Figure 5.3: *Relation between the length of the flat slab segment and mantle viscosity prefactor A, relative to the reference values in Table 5.1, for models with (solid line) and without (dashed line) latent heat. The prefactor A and the effective mantle viscosity are inversely related (see text). The x-axis displays the horizontal distance between trench and slab breakthrough point. The length of the flat slab segment increases with effective mantle viscosity with approximately 600 km in case without latent heat. The effects of latent heat results in an extra 150 to 300 km of flat-lying slab segment.*

reference model on the horizontal position of the point of slab penetration through the 400-km phase transition. A positive correlation between effective mantle viscosity and the length of the flat slab segment is observed for models with and without latent heat. Latent heat increases the flat slab length by approximately 150 km in a weak mantle, up to 300 km in a stronger mantle. Only the models with the weakest mantle do not show this feature. No real flat slab segment occurs in the models with a low-viscosity mantle, and in this case a reduction of the subduction angle is a better description of the latent heat effect. Besides a buoyancy effect, the thermal anomaly also influences the temperature-dependent mantle viscosity near the phase transitions. Although this weakening may be as large as half an order-of-magnitude just below the 400-km transition, the surface area of this phenomenon is too small to have a significant influence on the dynamics. On the whole, the importance of the mantle viscosity in these models is quite remarkable: the style of subduction changes from steep Benioff type subduction to flat subduction with a flat slab segment length of about 1000 km by changing the mantle viscosity with less than one order of magnitude, which is well within the uncertainty of estimates of effective upper mantle viscosity (Lambeck and Johnston, 1998).

In the scenario of lithospheric doubling, the occurrence of flat subduction is mainly due to the overriding continent (Christensen, 1996; Olbertz et al., 1997; van Hunen et al., 2000). Therefore, we varied the velocity of the overriding continent with respect to the deep mantle. Figure 5.4 illustrates the effect of the varying overriding velocity v_{ov} on
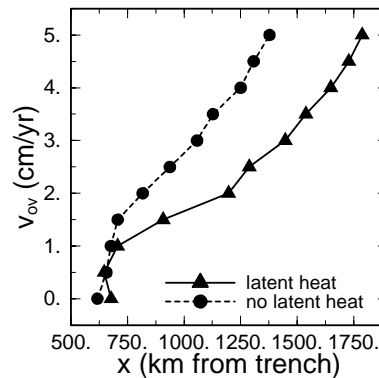

Figure 5.4: *Effect of the overriding velocity on the length of the flat slab segment for models with (solid line) and without (dashed line) latent heat. The horizontal axis shows the horizontal distance between trench and slab breakthrough point. Steep subduction occurs for a low continental overriding velocity ($<$ 1.5 cm/yr). A higher overriding velocity leads to an increasing slab length. Latent heat results in no extension of the flat slab segment for an overriding velocity of 1 cm/yr or less, up to a fairly constant extra flat slab length of about* 400 *km for an overriding velocity of 3 cm/yr or more.*

the lateral position of the breakthrough point. Steep subduction occurs in case of no or a small overriding velocity and latent heat seems to make little difference in these cases. When the overriding velocity exceeds approximately 1.5 cm/yr, the slab starts to flatten: the slab penetrates the 400-km transition further away from the trench. The length of the flat slab segment increases monotonically with increasing overriding velocity. With the flattening, the effect of latent heat release becomes increasingly important. For an overriding velocity of 3 cm/yr or higher, the effect of latent heat release leads to a slightly growing increase of the length of the flat slab segment to a little more than 400 km. This figure shows that the effectiveness of the latent heat release is not directly depending on the overriding velocity, but only indirectly through the style of subduction (high- or low-angle subduction).

Finally, we varied the strength of the 400-km phase transition through variation of the Clapeyron slope between 1 and 6 MPa/K, which affects the amount of latent heat release (Eq. 5.1). As shown in Figure 5.2, the effects of the 670-km transition are relatively small. We kept the parameters of this transition constant during the experiments to extract the influence of the greater impact of the 400-km phase transition. Figure 5.5 shows the effects of varying the Clapeyron slope on the lateral position of the breakthrough point. A
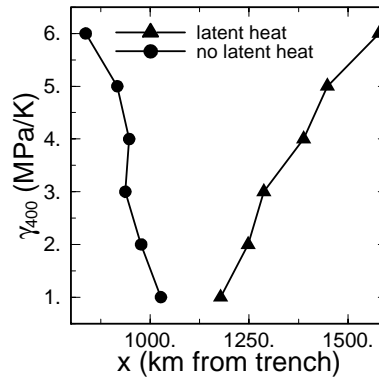
Figure 5.5: *The relation between Clapeyron slope of the 400-km phase transition and the length of the flat slab segment. The horizontal axis shows the horizontal distance between trench and slab breakthrough point. In case of latent heat (triangles), the flat slab grows roughly linearly with increasing Clapeyron slope. Without latent heat (circles), a stronger transition pulls down the slab more firmly, resulting in a shorter flat slab.*

roughly linear relation is present between the Clapeyron slope and the horizontal extent of the flat slab. Changing the Clapeyron slope from 1 to 6 MPa/K results in an extra 400 km flat slab segment. This is the result of two effects: On the one hand, once the slab reaches the vicinity of the phase transition, a strong transition tends to pull the slab more firmly, resulting in a shorter flat slab segment, which is visible from the results of experiments without latent heat. On the other hand, more latent heat release of the stronger transition leads to a stronger resisting buoyancy opposing penetration of the flat slab. The latter effect dominates, as illustrated with the curve of experiments with latent heat.

5.5   Discussion and concluding remarks

Shallow or very low-angle subduction is occurring at about 10% of the modern subduction zones (Gutscher et al., 2000b). As an explanation for this feature, the effect of the trenchward moving overriding plate (Vlaar, 1983; van Hunen et al., 2000) have been proposed. We have investigated the effects of latent heat of the mantle phase transitions at 400 and 670 km depth on the dynamics of low-angle subduction below a trenchward moving overriding continent. In such a situation, an overriding continent forces an oceanic plate to subduct to at least 100 km depth. This, in turn, pushes underlying mantle material down through the phase transitions, where latent heat release or absorption gives rise to positive phase buoyancy. For the 400-km transition, the maximum temperature change and depression are approximately 80 K and 8 km, respectively, while for the 670-km transition these are only 20 K and 2 km, respectively. We examined the significance of these latent heat effects on the dynamics of the slab. A 32-Ma old slab, which is forced
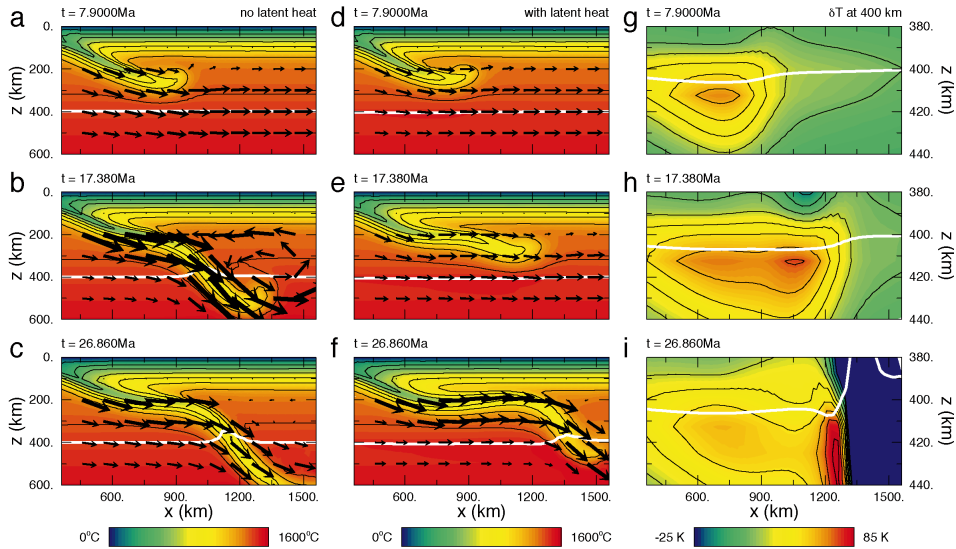
Figure 5.6: *Temperature contour snap shots of the reference model without (left) and with (middle) latent heat at $t = 7.9$ Ma (a,d), $t = 17.38$ Ma (b,e), and $t = 26.86$ Ma (c,f) are shown. The x-axis displays the horizontal distance to the trench. Black arrows visualize the direction and amplitude of the flow relative to the overriding plate. The horizontal slab length is increased by the effects of latent heat. The right panel shows a vertical exaggeration of the area around the 400-km transition with contour lines of the temperature change with respect to the situation at $t = 0$ Ma. White lines display the 400 km phase transition equilibrium position.*

to subduct into a moderately strong mantle below an overriding continent with 2.5 cm/yr, travels horizontally approximately 350 km further and 11 Ma longer if latent heat is included in the model calculations. As shown here, rapid vertical motion through the phase transitions results in a temperature discontinuity across the transition due to latent heat, which diffuses away again with time. Our initial temperature profile assumes no effects of latent heat release. This is a good assumption in case of a trenchward moving overriding plate, which continuously forces a different part of the mantle to sink through the phase transitions.

The style of subduction is strongly dependent on the mantle viscosity: a viscosity increase of only one order of magnitude may change the style of subduction from steep to horizontal. The significance of latent heat does not change much within this range. Variation of the overriding velocity changes the style of subduction from steep, for an overriding velocity of 1 cm/yr or less, to flat subduction, when the overriding velocity exceeds 3 cm/yr. Effects of latent heat are negligible at low overriding velocity, and show a slightly growing flat slab length increase to about 400 km above 3 cm/yr overriding

velocity. The relation between the Clapeyron slope and the length of the flat slab is almost linear. An increase of γ from 1 to 6 MPa/K leads to a 400 km longer flat slab segment. These results indicate that buoyancy effects from latent heat at low-angle subduction below an overriding continent form a robust feature that increases the tendency to flat subduction significantly.

Chapter 6

On the role of subducting oceanic plateaus in the development of shallow flat subduction

Abstract

Oceanic plateaus, aseismic ridges or seamount chains all have a thickened crust and their subduction has been proposed as a possible mechanism to explain the occurrence of flat subduction and related absence of arc magmatism below Peru, Central Chile and at the Nankai Trough (Japan). Its extra compositional buoyancy could prohibit the slab from sinking into the mantle. We investigated this effect using a numerical thermo-chemical convection model, simulating the subduction of an oceanic crust that contains an oceanic crustal plateau of 18 km thickness. With a systematic variation of the important physical parameters, we examined the physical circumstances that are required to obtain shallow flat subduction. Metastability of the basaltic crust in the eclogite stability field is of crucial importance for the slab to remain buoyant throughout the subduction process. The modeling results show that in a 44-Ma old subducting plate, basalt must be able to survive a temperature of $600 - 700^o$C to keep the plate buoyant sufficiently long to cause a flat slab segment. In addition, we found that the maximum yield stress in the slab must be limited to about 600 MPa to allow for the necessary bending to the horizontal. Young slabs show flat subduction for larger parameter ranges than old slabs, since they are less gravitationally unstable and show less resistance against bending. Furthermore, hydrous weakening of the mantle wedge area and lowermost continent are required to allow for the necessary deformation of a change in subduction style from steep to flat. The maximum flat slab extent, found in the models, is about 300 km. This is sufficient to explain the observed shallow flat subduction near the Nankai Trough (Japan), but additional mechanisms, such

as lithospheric doubling, need to be invoked to explain the flat slab segments up to 500 km long below Peru and Central Chile.

6.1   Introduction

The subduction of regions of oceanic lithosphere with overthickened crust (aseismic ridges, oceanic plateaus or seamount chains) seems to coincide spatially and temporally with the absence of arc volcanism (McGeary et al., 1985). In some of these cases, the slab dips more shallow or even horizontal at a depth of approximately 100 km. For example, gaps in recent active volcanism at low-angle subduction below Peru, Central Chile and at the Nankai trough near Japan seem to be related to the subduction of the Nazca Ridge, Juan Fernandez seamount chain and Palau-Kyushu Ridge, respectively (Cross and Pilger, 1982; McGeary et al., 1985). For these areas, a flat slab is observed at 200 km (Nankai) and 700 km (Peru and Chile) from the trench (Sacks, 1983; McGeary et al., 1985). In fact, flat subduction occurs along about 10% of the modern convergent margins, and most of these regions correlate with a subducting plateau or aseismic ridge (Gutscher et al., 2000b). Under such circumstances, absence of arc volcanism is explained by the disappearance of the mantle wedge with decreasing dip angle: contact of the hydrated subducted crust with the hot asthenosphere is absent, which stops partial melting and associated volcanism. Flat subduction of an even larger scale has been proposed to explain the formation of the Rocky Mountains during the Laramide orogeny (Dickinson and Snyder, 1978; Bird, 1988), although for this event no evidence of subducting oceanic plateaus is available.

The correlation between the subduction of oceanic plateaus and the occurrence of flat subduction suggests these plateaus to be anomalously buoyant. The overthickened crust is underlain by a proportionally overthickened harzburgite layer. During subduction, the gabbroic or basaltic crust transforms into eclogite. Eclogite and harzburgite have compositional buoyancies of opposite sign relative to undepleted mantle material (Irifune and Ringwood, 1993), that approximately cancel each other within an oceanic lithosphere. Only before eclogitisation, the subducting slab has a compositional buoyancy, which is dependent on the crustal thickness. If the eclogite formation would occur under near-equilibrium conditions, shallower than 70-80 km depth (Kirby et al., 1996a), slabs would lose their compositional buoyancy at this shallow depth, regardless of their crustal thickness. Only a kinetically hindered reaction from basalt to eclogite would cause the slab to preserve (some of) its compositional buoyancy to greater depth. Therefore, the hypothesis that buoyant plateaus cause flat subduction implicitly assumes a significant kinetic delay of eclogitisation of the crust.

The kinetics of the basalt-to-eclogite transition has been subject to research for several decades. Ahrens and Schubert (1975) report no significant reaction rates under completely dry conditions, but geologically fast reaction rates with the addition of water. More recent experiments (e.g. (Holland, 1980) vs. (Hacker et al., 1993)) do not reach consensus about the metamorphic reaction rates in the oceanic crust under subduction conditions (Hacker, 1996). Geological observations (pT-paths) suggest a wide range of possible reaction rates (Hacker, 1996; Austrheim, 1998): complete transformation at 450°C and in-

complete transformation at 800°C are both recorded. The degree of hydration is probably at least as significant as the ambient temperature and pressure and dry rocks can remain metastable for a long time (Rubie, 1990; Austrheim, 1998). Furthermore, deformation both enhances the reaction rates and facilitates the access of fluids (Saunders et al., 1996). Incomplete reaction to eclogite has also been suggested on the basis of seismological studies (Abers, 2000; Kirby et al., 1996a).

Increased buoyancy of the overthickened crust is not the only proposed mechanism to explain shallow flat subduction of the plateaus. Non-hydrostatic pressure forces (Jischke, 1975) or a slab suction force (Stevenson and Turner, 1977; Tovish et al., 1978) and active overriding of the overlying continent (lithospheric doubling) (Vlaar, 1983; van Hunen et al., 2000) are proposed as alternative mechanisms. In fact, the largest flat slab segments (Central Chile and Peru) occur below the fastest overriding plate motion (Jarrard, 1986). This suggests that lithospheric doubling plays a significant role in the creation of a horizontally subducting slab. However, the striking correlation between the subducting plateau locations and the sites of shallow flat subduction suggests an important influence of these plateaus on the subduction process.

Although several mechanisms have been proposed for the absence of arc volcanism above subducting plateaus, for the preservations of the compositional buoyancy of the plateaus and for the dynamics of the slab flattening, quantitative models are rare or absent. In this paper, we determine the viability and importance of shallow flat slab development as a consequence of a subducting 'buoyant plateau', using numerical modeling.

6.2   Model description

6.2.1   Governing equations and rheology description

To study the dynamics of a thickened crust within a subducting oceanic lithosphere, we have developed a two-dimensional finite element numerical model. We adopt the extended Boussinesq approximation (EBA) (Ita and King, 1994) and use a non-dimensionalization scheme as in (van den Berg et al., 1993). In non-dimensional form, the governing equations are:

$$\partial_j u_j = 0 \qquad (6.1)$$

$$\partial_j(\eta\dot{\epsilon}_{ij}) - \partial_i \Delta P = (RaT - \sum_k Rb_k\Gamma_k + RcC)\delta_{iz} \qquad (6.2)$$

$$\frac{\partial T}{\partial t} + u_j\partial_j T - Di(T+T_0)w - \sum_k \gamma_k \frac{Rb_k}{Ra} Di(T+T_0)\frac{d\Gamma_k}{dt} - \partial_j\partial_j T$$

$$= \frac{Di}{Ra}\Phi + H \qquad (6.3)$$

$$\frac{\partial C}{\partial t} + u_j\partial_j C = 0 \qquad (6.4)$$

Equations 6.1 to 6.4 describe conservation of mass, momentum, energy and composition, respectively. Symbols are explained in Table 6.1.

Symbol	Meaning	Value used	Dimension
$A_{k,m}$	Pre-exponential flow law parameter	—	$\text{Pa}^{-n}\,\text{s}^{-1}$
A_{kin}	Kinetic pre-exponent	10^{-6}	$\text{K}^{-1}\,\text{s}^{-1}$
C	Composition parameter	—	—
c_p	specific heat	1250	$\text{J}\,\text{kg}^{-1}\text{K}^{-1}$
Di	Dissipation number $= \alpha g h / c_p$	0.47	—
$E_{k,m}^*$	activation energy	—	$\text{J}\,\text{mol}^{-1}$
E_{kin}^*	kinetic activation energy	—	$\text{J}\,\text{mol}^{-1}$
H	non-dimensional radiogenic heat production	—	—
k	material index	—	—
m	deformation mechanism index	—	—
$n_{k,m}$	viscosity stress exponent	—	—
n_y	yield stress exponent	5	—
Q_L	Latent heat release across a phase transition	—	$\text{J}\,\text{kg}^{-1}$
R	gas constant	8.3143	$\text{J}\,\text{K}^{-1}\,\text{m}^{-3}$
Ra	Thermal Rayleigh number $\rho\alpha\Delta T h^3/\eta\kappa$	1.8×10^7	—
Rb	Phase Rayleigh number $\delta\rho g h^3/\eta\kappa$	2.4×10^7	—
Rc	Compositional Rayleigh number $\Delta\rho_c g h^3/\eta\kappa$	2.4×10^7	—
T	non-dimensional temperature	—	—
T_0	non-dimensional surface temperature	$273/\Delta T$	—
ΔG	Gibbs free energy between basalt and eclogite	—	$\text{J}\,\text{mol}^{-1}$
ΔP	non-dimensional hydrodynamic pressure	—	—
ΔT	temperature contrast across model domain	2300	K
t	non-dimensional time	—	—
t_{tr}	transition time for the eclogitisation reaction	10	Ma
$\mathbf{u}$	non-dimensional velocity $\mathbf{u} = (v, w)^T$	—	—
$V_{k,m}^*$	activation volume	—	$\text{m}^3\text{mol}^{-1}$
Y	growth function of the eclogitisation reaction	—	—
α	thermal expansion coefficient	3×10^{-5}	K^{-1}
Γ_k	phase functions for all k mantle phase transitions	—	—
γ_{400}	Clapeyron slope 400 km phase transition	3	MPaK^{-1}
γ_{670}	Clapeyron slope 670 km phase transition	-2.5	MPaK^{-1}
ΔG	Gibbs free energy difference between reaction products	—	$\text{J}\,\text{mol}^{-1}$
$\Delta\rho_c$	compositional density relative to mantle material		
	basalt	-400	$\text{kg}\,\text{m}^{-3}$
	harzburgite	-77	$\text{kg}\,\text{m}^{-3}$
δT	temperature increase due to latent heat release	—	K
δz	phase transition deflection	—	m
$\delta\rho_{400}$	density difference across the 400 km phase transition	273	$\text{kg}\,\text{m}^{-3}$
$\delta\rho_{670}$	density difference across the 670 km phase transition	342	$\text{kg}\,\text{m}^{-3}$
$\dot{\epsilon}_{ij}$	$\dot{\epsilon}_{ij} = \partial_j u_i + \partial_i u_j =$ strainrate tensor	—	s^{-1}
$\dot{\epsilon}$	2nd invariant of the strainrate	—	s^{-1}
$\dot{\epsilon}_y$	reference strainrate in yield strength determination	10^{-15}	s^{-1}

Table 6.1: *Notations*

Symbol	Meaning	Value used	Dimension
η	non-dimensional viscosity	–	–
Θ	non-dimensional eclogitisation rate	–	–
Φ	non-dimensional viscous dissipation	–	–
ρ	mantle density	3416	kg m^{-3}
τ_y	yield stress	–	Pa
τ_{ij}	deviatoric stress tensor	–	Pa
τ	2nd invariant of the stress tensor τ_{ij}	–	Pa
τ_y	yield stress for strainrate $\dot{\epsilon}_y$	–	Pa

Table 6.1: *Notations (continued)*

The model distinguishes between crustal and mantle material, where the latter is subdivided into depleted harzburgite and undepleted peridotite. We use a composite rheology combining several deformation mechanisms, for crust and mantle material separately. The effective viscosity is defined as in (van den Berg et al., 1993):

$$\eta_{k,\text{eff}} = \left(\sum_m (\eta_{k,m})^{-1} \right)^{-1} \tag{6.5}$$

where k refers to the material and m to the deformation mechanism. Each $\eta_{k,m}$ defines the viscosity corresponding to a single deformation mechanism in a given material. For two deformation mechanisms, diffusion creep and dislocation creep, an Arrhenius flow law is used:

$$\eta_m = A_m^{-1/n_m} \dot{\epsilon}^{(1-n_m)/n_m} \exp \left(\frac{E_m^* + pV_m^*}{n_m RT} \right) \tag{6.6}$$

where the material subscript k is omitted for clearness. Diffusion creep is not considered for crustal material.

We used a material-independent stress limiting rheology with a yield viscosity

$$\eta_y = \tau_y \dot{\epsilon}_y^{-1/n_y} \dot{\epsilon}^{1/n_y - 1} \tag{6.7}$$

as an additional deformation mechanism in Equation 6.5 to limit the strength of the material to approximately the yield stress τ_y. The powerlaw index n_y defines the 'brittleness' of the stress limited material: the 'Newtonian' limit is $n_y = 1$ for which η_y is independent on stress or strainrate and a 'viscosity limiter' would be a more appropriate term, while the 'brittle' limit of a very large n_y refers to a maximum stress, regardless the strainrate. For intermediate values, the stress limiter behaves like a powerlaw creep mechanism. We applied the value $n_y = 5$ in all models. Such stress limiter effectively replaces other, not implemented deformation mechanisms, such as the Peierl's mechanism (Kameyama et al., 1999).

The used mantle flow laws apply to dry material. However, the area above a subducting slab (i.e. the mantle wedge and lowermost continent) is hydrated (Karato, 2001), most likely by continuous dehydration of the subducting slab and dry flow laws would overestimate the local strength (Mei and Kohlstedt, 2000a,b; Karato and Jung, 2001). Therefore,

in some model calculations, we included in this area a simple parameterization of hydrous weakening, relative to the dry mantle strength. Table 6.2 describes the set of used rheological parameters.

Symbol	Meaning	Value used	Dimension
$A_{k,m}$	Pre-exponential flow law parameter		
	crustal dislocation creep value	7.4×10^{-39}	$\mathrm{Pa}^{-n}\mathrm{s}^{-1}$
	reference mantle diffusion creep value[a]	3.04×10^{-11}	$\mathrm{Pa}^{-n}\mathrm{s}^{-1}$
	reference mantle dislocation creep value[a]	3.84×10^{-16}	$\mathrm{Pa}^{-n}\mathrm{s}^{-1}$
$E_{k,m}^{*}$	activation energy		
	crustal dislocation creep value	0	$\mathrm{J\,mol}^{-1}$
	reference mantle diffusion creep value[a]	300×10^{3}	$\mathrm{J\,mol}^{-1}$
	reference mantle dislocation creep value[a]	540×10^{3}	$\mathrm{J\,mol}^{-1}$
$n_{k,m}$	viscosity stress exponent		
	crustal dislocation creep value[b]	3.4	—
	reference mantle diffusion creep value[a]	1.0	—
	reference mantle dislocation creep value[a]	3.5	—
n_y	yield stress exponent	5	—
$V_{k,m}^{*}$	activation volume		
	crustal dislocation creep value	0	$\mathrm{m}^{3}\mathrm{mol}^{-1}$
	reference mantle diffusion creep value	4.5×10^{-6}	$\mathrm{m}^{3}\mathrm{mol}^{-1}$
	reference mantle dislocation creep value[c]	14×10^{-6}	$\mathrm{m}^{3}\mathrm{mol}^{-1}$
$\dot{\epsilon}_y$	reference 'yield strainrate'	10^{-15}	s^{-1}

Table 6.2: *Rheological parameters.*
Sources: [a]*(Karato and Wu, 1993);* [b]*(Shelton and Tullis, 1981);* [c]*(Karato and Rubie, 1997)*

6.2.2   Model setup

We used a 2000 km deep Cartesian box to model the subduction process. Horizontally, the model is subdivided into a subducting oceanic part on the left and a static continental part on the right, as illustrated in Figure 6.1. The oceanic lithosphere ranges from a mid-ocean ridge (MOR), in the upperleft corner of the model box, to a trench, to the right of which a 2200 km wide continent is positioned.

The large-scale driving mechanism of most subduction processes is dominated by the slab pull. This, however, cannot result in flat subduction, since slab pull acts vertically. If an oceanic plateau is able to support a flat slab, this is a direct indication that its buoyancy force exceeds the slab pull. This implies that the plateau would not subduct at all, if it was not part of a much larger and rather rigid oceanic plate, which determines the subduction velocity. In order to simulate these conditions in our models, we impose a constant trenchward velocity on the plate to be subducted. A 5-cm-per-year subduction velocity is imposed through a trenchward oceanic surface velocity boundary condition in combination with a non-moving continent. The converging plates are decoupled by a free-slip fault extending up to 100 km depth and the rather weak interface of the subducting
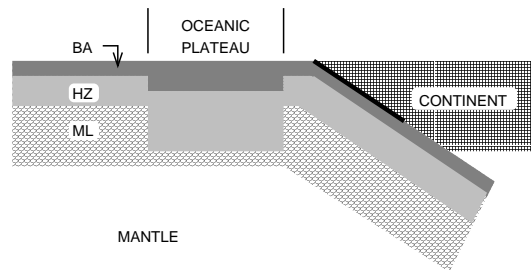
Figure 6.1: *Schematic diagram of the numerical model setup. A layered oceanic litho-sphere contains an oceanic plateau, which is subducted below a continent with 5 cm/yr. BA = basalt, HZ = harzburgite and ML = mantle lithosphere. The solid line represents a free-slip fault to decouple the plates.*

oceanic crust. The model does not contain a forebulge and the dip angle of the curved fault increases from zero (horizontal) to about 23 degrees at 100 km depth. The distance from MOR to trench and the subduction velocity determine the age of the slab near the trench. This age, as well as the prescribed subducting plate velocity and the distance from MOR to trench are kept constant throughout each model calculation.

Thermal initial and boundary conditions, as well as the radiogenic heat production are similar to a previous model, described in (van Hunen et al., 2000). The initial geotherm is defined by an adiabat for the oceanic subsurface and a steady state, 60 mW m^{-2} surface continental heatflow geotherm with radiogenic heat production distribution from (Chapman, 1986). Thermal boundary conditions are a mantle adiabat (potential temperature $T_p = 1300^o$ C) at the left hand side and bottom boundary, $T = 0^o$C at the surface and a continental geotherm on the right hand side boundary. An initial situation of 'unperturbed' Benioff subduction was created by an initial 16-Ma-lasting oceanic subduction process with 5 cm/yr. During this initial stage, the tip of the slab reaches the transition zone. We define model time $t = 0$ at the end of this initial stage. The oceanic lithosphere is stratified with a 7-km-thick crust and a 18-km-thick harzburgite layer on top of undepleted peridotite. If applied, a 400-km-wide oceanic plateau is positioned in front of the trench at $t = 0$, where the crustal and harzburgitic layer are 18 and 46.2 km thick, respectively. The major mantle phase transitions at 400 and 670 km depth are included using a 20-km wide harmonic parameterization of the phase functions Γ_k in Equations 6.2 and 6.3. Relative compositional densities and density changes across the mantle phase transitions are reported in Table 6.1. Both buoyancy effects as a result of phase boundary deflection and latent heat production/consumption (van Hunen et al., 2001) terms are taken into account. We did not include olivine metastability, since, regarding the age of the slabs, it is unlikely to be significant (Kirby et al., 1996b; Schmeling et al., 1999). For a more elaborate description of the implementation, effects and used parameters of the mantle phase transitions, we refer to (van Hunen et al., 2001).

6.2.3   Eclogitisation and reaction kinetics

Basalt/gabbro transforms into eclogite during the subduction process, thereby neutralizing the compositional buoyancy of the subducting slab (Table 6.1). We implemented crustal metamorphism and included the possibility of kinetic hindrance of the metamorphic reaction. Detailed descriptions of phase change kinetics are given in (Kirby et al., 1996b; Riedel and Karato, 1996; Däßler et al., 1996), where it was applied to the well-studied and well-constrained olivine-to-spinel transition. For time-dependent pressure and temperature conditions, a general solution to the kinetic equation is

$$\frac{d\Gamma}{dt} = \Theta \tag{6.8}$$

where Θ is a multiple time integral over the nucleation and growth functions I and Y (Kirkpatrick, 1976; Däßler et al., 1996). Here, we approximate this integral with a simpler description for time-independent nucleation and growth functions, which is not explicitly dependent on time and is known as the Avrami equation:

$$\Gamma = 1 - \exp(-aIY^3t^4) \tag{6.9}$$

A general Arrhenius formulation of the growth function Y is given by (Däßler et al., 1996):

$$Y \sim T \exp\left(\frac{-E_{kin}}{RT}\right)\left[1 - \exp\left(\frac{\Delta G}{RT}\right)\right] \tag{6.10}$$

where E is the activation energy for growth and ΔG the Gibbs free energy difference between the two phases. The basalt-to-eclogite kinetic properties are less well known than those of the olivine-to-spinel transition, partly because crustal materials are less extensively studied than olivine, and partly because the role of hydration is less certain. We decided, therefore, to use the approach from (Giunchi and Ricard, 1999). First, they describe the kinetics of crustal metamorphism in a simplified system, using the reaction

$$\mathrm{albite} \Rightarrow \mathrm{jadeite} + \mathrm{quartz}$$

for which the necessary parameters (Gibbs free energy, Clapeyron slope, etc.) are relatively well known (Putnis, 1992). Second, they assume a nucleation function with a p-T dependence of the same form as the growth function. We assume that because of the large uncertainties in the crustal kinetic parameters, this is a justified approximation. Equation 6.9 then reduces to:

$$\Gamma = 1 - \exp(-A_{kin}Y^4t^4) \tag{6.11}$$

The reaction rate Θ is found by inserting Equation 6.11 into 6.8 and closely resembles the function

$$\Theta = 4A_{kin}Y((\Gamma(1-\Gamma))^{3/4} + \epsilon) \tag{6.12}$$

which is symmetric about $\Gamma = 0.5$, and where $\epsilon = 10^{-3}$ is a small constant to start the reaction. Despite the simplifications, the solution still describes the following main kinetics: (1) a thermal activation barrier hinders the transition at low temperatures; (2) some

oversrepping (i.e. movement from the equilibrium boundary into the eclogite stability field) is necessary for the transition to occur; (3) initially, the reaction rate increases exponentially with time where after it slows down again near the completion of the reaction. The parameters A_{kin} and E_{kin} determine how the reaction rate depends on the ambient temperature. These parameters can be estimated using geological and geophysical observations. Peak temperatures in the p-T-paths of partly eclogitised rocks range from 450 to 800^oC (Austrheim, 1998), although the upper value is mainly observed in essentially dry rocks, an unlikely situation in subduction zones. We can estimate suitable combinations of A_{kin} and E_{kin} from a p-T condition for which the reaction occurs well within the eclogite stability field, so that the term between square brackets in Equation 6.10 is essentially 1. For all experiments, we choose $A_{kin} = 10^{-6} \mathrm{s}^{-1}$. Values for E_{kin} are given in Table 6.3. ΔG is calculated with parameters from (Putnis, 1992).

Model	oceanic plateau present	slab age (Ma)	T_{tr} (^oC)	E_{kin} (kJ/mol)	τ_y (MPa)	relative mantle wedge weakening
REFp	yes	44	700	214	200	0.1
REFnp	no	44	700	214	200	0.1
KIN1	yes	44	400	146	200	0.1
KIN2	yes	44	500	169	200	0.1
KIN3	yes	44	600	192	200	0.1
KIN4	yes	44	800	238	200	0.1
YLD1	yes	44	700	214	100	0.1
YLD2	yes	44	700	214	300	0.1
YLD3	yes	44	700	214	400	0.1
YLD4	yes	44	700	214	500	0.1
YLD5	yes	44	700	214	600	0.1
YLD6	yes	44	700	214	700	0.1
YLD7	yes	44	700	214	800	0.1
YLD8	yes	44	700	214	900	0.1
YLD9	yes	44	700	214	1000	0.1
AGE1	yes	20	700	214	200	0.1
AGE2	yes	32	700	214	200	0.1
AGE3	yes	56	700	214	200	0.1
WMW1	yes	44	700	214	200	1.0
WMW2	yes	44	700	214	200	0.05

Table 6.3: *Definition of the model calculations*

6.3 Results

6.3.1 Buoyancy effect of a subducting plateau

The capacity of an oceanic plateau to flatten a subducting slab is investigated through a series of model calculations. By variation of several model parameters, the robustness of the results were tested. In this section, we will describe the influence of the most domi-

nating parameters. The performed model calculations are listed in Table 6.3. We defined the reference model REFp with an oceanic plateau and its equivalent without a plateau as model REFnp. The model parameters of all calculations are described in Tables 6.1 and 6.3. Figure 6.2 shows a series of temperature snapshot plots for models REFp and REFnp.
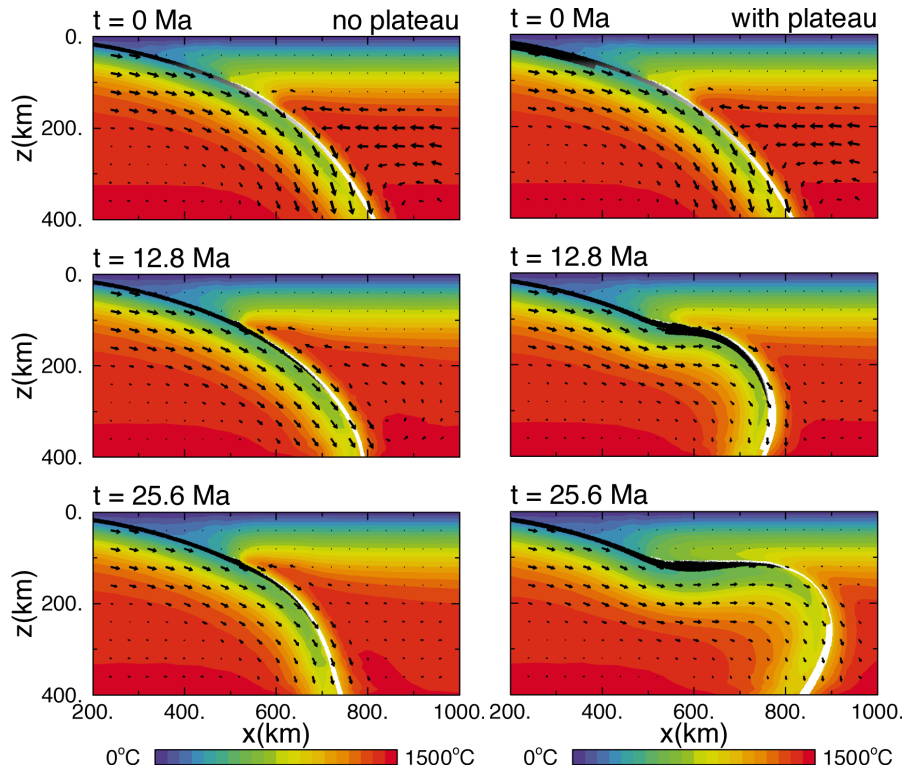

Figure 6.2:   *Temperature contourplot (colors) of the subduction process in time for a subducting oceanic plateau (right, model REFp) in comparison with the subduction of 'normal' oceanic lithosphere (left, model REFnp). Black-and-white area represents the transition from basalt (black) to eclogite (white). Time increases from $t = 0$ Ma at the beginning of the plateau subduction to the final stage of the plateau subduction at 25 Ma. Horizontal axes give the distance to the trench, vertical axes the depth.*

The slab reaches a depth of 100 km at almost 500 km from the trench. This large distance is due to the absence of a forebulge, which causes the slab to enter the trench with a zero dip angle. In model REFp, the subduction of the plateau causes a flat segment, whereas model REFnp shows no flattening. The length of the flat slab segment is a few hundred km, measured from the position where the slab bends to the horizontal to the point where the slab steepens again to subduct further into the mantle. The thickened basaltic plateau

crust and underlying thickened harzburgite layer provide enough buoyancy to support the slab, whereas a normal oceanic slab does not. Basalt transforms into eclogite as the slab warms up at its arrival in the hot asthenosphere. This process is initiated at the top of the crust and later migrates to deeper parts of the crust, approximately along with the isotherms, as can be seen from the gradual thinning of the black crustal area in Figure 6.2. After eclogitisation, the plateau becomes gravitationally unstable and causes further steep subduction or 'resubduction' into the mantle. Only during the horizontal subduction of the plateau, the length of the flat slab segment increases. After resubduction of the plateau, the length of the flat slab remains rather constant in time.

6.3.2 Parameter sensitivity

Influence of the eclogitisation kinetics

The influence of the basalt-to-eclogite transformation rate on the dynamics of the subducting oceanic plateau is examined through variation of the activation energy E^*_{kin} in models REFp and KIN1 to KIN4. We varied E^*_{kin} between 146, 169, 192, 214 and 238 kJ/mol. At these values, 50% of the reaction takes place within the transition time $t_{tr} = 10$ Ma at the temperature of 400, 500, 600, 700, and 800° C, respectively. We define this temperature to be the transition temperature T_{tr}. The transition time t_{tr} is chosen to represent a geologically significant time for the basalt to survive in a metastable phase. Figure 6.3
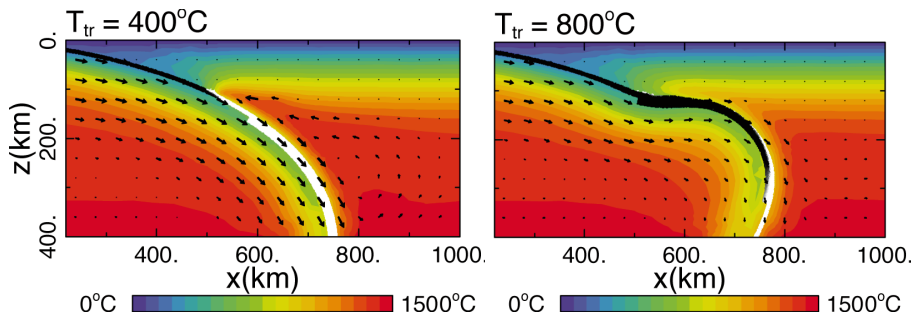

Figure 6.3: *Temperature contourplot of the plateau subduction process at $t = 12.8$ Ma after initiation of plateau subduction a) With a transition temperature $T_{tr} = 400^oC$, the compositional buoyancy is removed before flattening can start. b) With $T_{tr} = 800^oC$, the compositional buoyancy of the plateau is still preserved and flattens the slab.*

shows the resulting slab dynamics at time $t = 12.8$ Ma in case of plateau subduction for both extreme cases. The high-T_{tr} case shows much similarity with the reference model results, shown in Figure 6.2. The low-T_{tr} case, however, shows no sign of flat subduction, eclogite is formed throughout the whole plateau almost with the first asthenospheric contact, and the slab loses its compositional buoyancy before being able to flatten. In Figure 6.4, the pressure-temperature-time-paths (pTt-paths) are shown for models KIN1 (with
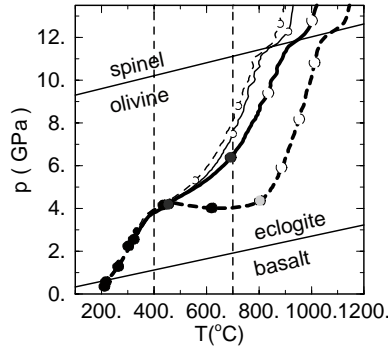
Figure 6.4: *Pressure-temperature-time (pTt) paths of the subduction process for model REFp ($T_{tr} = 700^oC$, thick lines) and KIN1 ($T_{tr} = 400^oC$, thin lines). Each path represents a point which was located 10 km below the surface before subduction (about halfway the basaltic unit of the plateau). Solid and dashed lines represent points the leading and trailing edge of the plateau, respectively. Symbols are plotted every 3.2 Ma and represent the eclogitisation from basalt (black) to eclogite (white). Diagonal lines give the equilibrium position of the basalt-to-eclogite and olivine-to-spinel transitions. Vertical dashed lines show T_{tr} for models KIN1 and REFp, at 400° C and 700° C, respectively.*

$T_{tr} = 400^oC$) and model REFp (with $T_{tr} = 700^oC$) for two monitor points, advected in the subducting slab. These points are positioned at the leading and trailing edge of the subducting plateau, 10 km below the surface of the slab. In model KIN1, the plateau has little influence on the subduction geometry: the leading edge and later the trailing edge of the plateau describe a rather similar pT-path. In model REFp, however, the slab flattens during the plateau subduction: the leading edge still subducts relatively steep, but the trailing edge already subducts horizontally below the continent at about 4 GPa pressure. The slab heats up and eclogitisation becomes significant above $T = 700^oC$. Finally, pressure increase again as the slab 'resubducts' further into the mantle. Figure 6.5a shows the development in time of the flat slab segment due to plateau subduction for several transition temperatures T_{tr}. Flattening of the plateau only occurs if basalt is able to survive a temperature of at least 700° C. The results show a bi-modal distribution in the style of subduction and the transition between steep and flat slabs is remarkably sharp: a flat slab either develops completely or not at all.

Influence of the slab strength

The low temperature of the slab interior results in large resistance against deformation by diffusion creep or dislocation creep. Near the surface, brittle failure limits the strength of lithospheric plates, but at larger depth this mechanism is not effective. To avoid an unrealistically large strength of the subducting slab, an additional yield stress deformation mechanism is applied (see e.g. Ranalli, 1987; Kohlstedt et al., 1995). Section 6.2.1

describes the implementation of this mechanism. This temperature-independent stress-limiting creep mechanism governs the deformation of the slabs, which is consistent with the idea that plate velocities are relatively insensitive to changes in the mantle temperature (Conrad and Hager, 1999b). For the reference model REFp, this yield stress τ_y was quite arbitrarily chosen to be 200 MPa. In models REFp and YLD1 to YLD9, the importance of this yield stress was evaluated by varying it between 100 MPa and 1 GPa. Figure 6.5b combines these results. Up to $\tau_y = 600$ MPa, an increase in the yield stress results in an increased flat slab length: during its horizontal motion, the slab slowly loses its compositional buoyancy due to ongoing eclogitisation, until a point is reached where the slab is dense enough to continue its descent into the mantle. From that point on, the mechanical coherence of the slab mainly determines the dip angle. A weak slab allows immediate resubduction, while a strong slab will resist bending and descending. For $\tau_y > 600$ MPa, the slab is so strong, that even the initial bending phase of the buoyant plateau towards the horizontal is not possible: the available buoyancy force is smaller than the necessary force to bend the slab. In that case, the slab continues its initiated descend at the trench and no flat slab segment is created at all. In addition to this set of experiments, we performed several calculations to investigate the combined effects of the maximum yield strength of the material and the transition temperature of the basalt-to-eclogite transition. The clear distinction between flat and steep subducting slabs suggests the possibility of a different representation of the results, as shown in Figure 6.6. An increasing slab strength requires a slightly increasing transition temperature T_{tr}, up to which basalt remains metastable. The minimum required T_{tr}, however, does not vary much. This implies that the results from Section 6.3.2 are only weakly dependent on the slab strength.

If a buoyant oceanic plateau is the dominant mechanism for the creation of shallow flat subduction, these results have implications for the maximum strength of subducting slabs. On the one hand, model calculations with $\tau_y < 100$ MPa showed too little rigidity for the development of a large flat slab segment. In this case, the dip angle of the slab has very little significance, since plate-like behavior is almost absent. On the other hand, $\tau_y \geq 600$ MPa required basalt metastability to an unrealistically high temperature of 800^oC. This indicates that the maximum slab strength that allows for flat subduction is only about one order of magnitude higher than the minimum strength to maintain mechanical rigidity, and that a reasonable range for the maximum slab strength is rather limited. This would indicate that slabs are some, but not many orders of magnitude stronger than the surrounding mantle material. This is in agreement with the conclusion of Moresi and Gurnis (1996) who favor weak slabs that cannot act as stress guides from the deep mantle to the surface. Based on similar criterions, Houseman and Gubbins (1997) suggest from numerical model simulations, that only a narrow transition between too strong and too weak slabs can explain the slab geometry and stress orientation of the Tonga subduction zone. Conrad and Hager (2001) showed that plates and slabs should be sufficiently viscous (10^{23} Pa s), but their total strength should be limited to produce plate-like surface motions. These results all suggest that a suitable range for the maximum strength of the slab is quite limited, and reasonably well constrained.
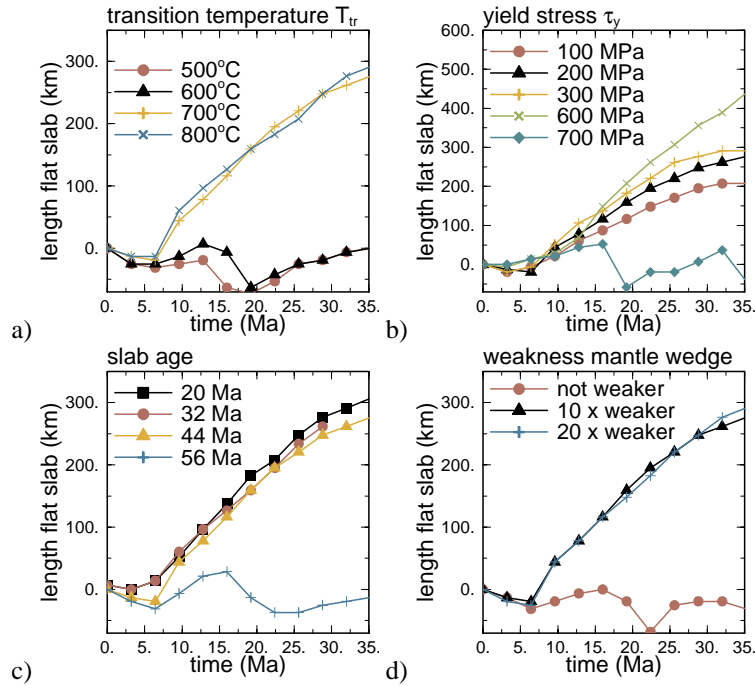
Figure 6.5: *Length of the flat slab segment in time for different values of the most critical model parameters. a) transition temperature T_{tr}. $T_{tr} \leq 600^oC$ gives steep plateau subduction, $T_{tr} > 600^oC$ gives a flat subducting plateau. b) yield stress τ_y. For $\tau_y \leq 600$ MPa, a larger slab strength resists immediate bending after eclogitisation more strongly than a weak one. For $\tau_y > 600$ MPa, the slab is too strong to bend to the horizontal and steep subduction is continued. c) slab age at the trench. Only slabs of 44 Ma old or younger are sufficiently buoyant to be supported by the oceanic plateau. d) relative strength of the mantle wedge and lowermost overriding continent. A mantle wedge weakening of one order of magnitude is required to allow a change in the style of subduction.*

Influence of the age of the slab

Variation of the age of the subducting plate has an effect which is comparable to the variation of the slab strength in the former subsection. Results of models REFp and AGE1 to AGE3 are plotted in Figure 6.5c. The age of the subducting plate at the trench ranges from 20 to 56 Ma. For all slabs of 44 Ma or younger, the plateau is able to produce a flat slab segment. The 56-Ma old slab, however, fails to bend to the horizontal and continues its descend into the mantle. Again, the strength of the slab plays an important role, since older slabs are colder and mechanically stronger than young slabs. Another effect of the age variation comes from the thermal buoyancy: the old and cold slab is denser than a
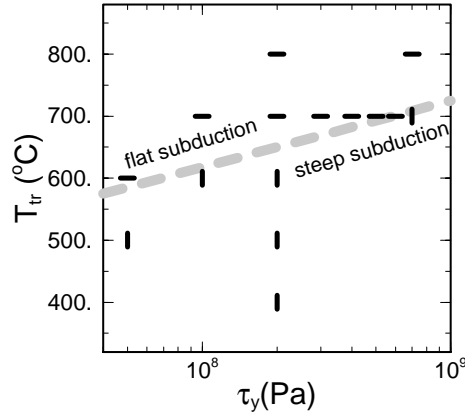
Figure 6.6: *Subduction dynamics for various maximum yield stresses τ_y and eclogitisation transition temperatures T_{tr}. Flat subduction is indicated with a horizontal line, steep subduction with a vertical line. The grey dashed line indicates the approximate transition between steep and flat subduction. Except for very weak slabs, flat subduction requires $T_{tr} = 700^\circ C$ and $\tau_y > 600$ MPa requires an even higher T_{tr}.*

young, warm slab. This results in a larger negative thermal buoyancy. By comparison of thermal and compositional buoyancy forces, Cloos (1993) calculated that an oceanic plateau with a 17-km thick crust is neutrally buoyant at the age of approximately 80 Ma, when the lithosphere is about 100 km thick. Gutscher et al. (2000b) suggested that an 18-km thick crustal oceanic plateau is sufficiently buoyant to support itself, including an adjacent portion of normal slab with comparable width for lithospheric ages up to 50 Ma. We compared thermal and compositional buoyancy of the slab using an analytical cooling-halfspace approach. The extra mass per unit area of the oceanic lithosphere due to thermal contraction Δm_T is calculated (Turcotte and Schubert, 1982, Ch.4-22):

$$\Delta m_T = 2\alpha \rho_m T_m \sqrt{\frac{\kappa t}{\pi}} \tag{6.13}$$

Compositional buoyancy is calculated using relative density values of -400 and -77 kg/m^3 for basalt/gabbro and harzburgite, respectively. Figure 6.7 shows the total (thermal and compositional) buoyancy for different crustal thicknesses before eclogitisation. Normal oceanic crust has a thickness of about 7 km and becomes gravitationally unstable at 25 Ma, but a thicker crust is also stable at greater age. According to this estimate and the ones by Cloos (1993) and Gutscher et al. (2000b), a plateau with an 18-km-thick crust will be buoyant even for the oldest oceanic lithospheres found on Earth today. The absence of a flat plateau in the 56-Ma-lithosphere model calculation from Figure 6.5c is not in agreement with these estimates. This has two reasons. First, the total integrated buoyancy of the slab may be smaller than analytically predicted: parts of the slab around
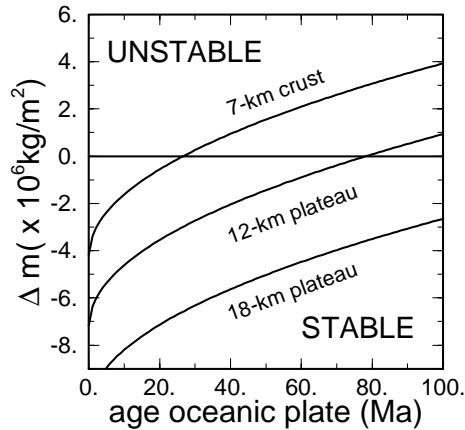
Figure 6.7: *Integrated buoyancy estimates of oceanic lithosphere before eclogitisation as a function of the age of the oceanic plate for crustal thicknesses of 7, 12 and 18 km. Normal oceanic lithosphere (7 km crust) remains buoyant until an age of ~25 Ma, while a plateau with an 18-km crust remains buoyant even at high ages.*

the plateau have no thickened crust and the plateau should be able to support those parts as well; partial eclogitisation of the plateau may already neutralize some of the compositional buoyancy in an early stage in the subduction process. Second, the analytical buoyancy calculations do not take into account the forces that are required to bend the slab. Section 6.3.2 shows that we cannot discard the strength of the slab.

Mantle wedge deformation due to the changing subduction style

In order to enable a changing slab geometry from steep to shallow horizontal subduction, the lowermost part of the lithosphere and the mantle wedge should be able to deform to adapt to the new subduction style. During continuous steep subduction prior to the plateau subduction, the overriding continent and mantle wedge are cooled by thermal conduction in the vicinity of the slab. When the rheology for dry mantle material is applied in the mantle wedge, an asperity is formed, as shown in Figure 6.8. A more realistic rheology description, however, would include hydrous weakening of the overlying mantle wedge as a result of dehydration of the underlying slab (Tatsumi and Eggins, 1995; Karato, 2001), as this process continuously delivers water to the mantle wedge. We investigated the effect of hydrous mantle wedge weakening on the dynamics of the subducting plateau using models REFp, WMW1 and WMW2. To model the effect of hydrous weakening, we applied a regional weakening in a 150 km wide zone in the mantle wedge corner above the slab and below the depth of 100 km. We applied a weakening relative to the dry mantle material, using a local change in the viscosity prefactor $A_{k,m}$ ranging from 1 (no weakening) to 0.05 (20 x weaker mantle wedge). Model REFp contains an intermediate

weakening of 0.1 (10 x weaker mantle wedge). Figure 6.5d combines the results of the various amounts of weakening in terms of a resulting length of the flat slab region as a function of time. The model without a weakened mantle wedge does not show any development of a flat slab segment, while a weakening of one order of magnitude is sufficient to allow the necessary mantle wedge deformation for the flattening. A further decrease of the mantle wedge strength does not further change the slab geometry.

6.4   Discussion

6.4.1   The limited lateral extent of the plateau along the trench

All model results were obtained with a two-dimensional subduction model. Strictly speaking, such model only applies to a subduction process without any changes in the direction along-trench. Aseismic ridges and especially seamount chains are long and relatively narrow features, for which this 2-D model may not apply. Even flat-subducting oceanic plateaus only form a small portion of the total subducting plate at the trench. The possible transition between the flat-subducting plateau and neighboring steep-subducting normal oceanic lithosphere is illustrated by (Sacks, 1983) and (Gutscher et al., 1999b) and is described by either a gradual change in the subduction dip angle or an abrupt one, in case the slab tears. If the slab does not tear, we expect an extra slab pull force on the sides of the subducting plateau, so that the horizontal subduction is hindered by a larger total slab pull. In that case, the presented model results probably form an upperbound of the ability of such a plateau to support the slab.

6.4.2   The transition between steep and flat subducting plateaus

Examination of time series plots in Figure 6.5 reveals a bi-modal behavior, because it shows that a flat slab segment is either fully created or not at all, and that an intermediate-angle subduction regime does not occur. Apparently, initial flattening of the slab strengthens the ability to flatten the slab even more. Several mechanisms are likely to be responsible for this feature. On the one hand, the heating of the top of the slab is retarded if the slab subducts horizontally, since it is not in contact with hot asthenosphere in the mantle wedge, but with the much cooler base of the continent. This results in a delay of the basalt-to-eclogite transition, which keeps the slab buoyant further away from the trench. It also delays the thermal weakening of the slab, so that it does not immediately resubduct after eclogitisation. However, a significant delay in the heating of the slab and the eclogitisation is not observed in models with shallow flat subduction as compared to models with a steeper subduction (Figure 6.2). On the other hand, the dynamic pressure from the mantle wedge flow exerts a torque on the slab that tends to decrease the subduction dip angle. This mechanism was already proposed by Tovish et al. (1978). They showed that this effect increases with decreasing dip angle, as the mantle wedge is getting narrower, and suggested this to be a mechanism to explain the gap in observed subduction angles between about 10 an 20 degrees. In addition, we expect a contribution from
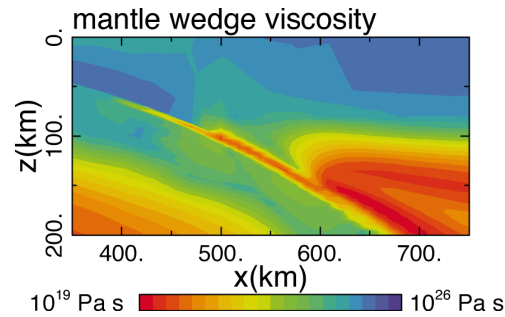
Figure 6.8: *Continuous cooling of the mantle wedge in the vicinity of the steeply subducting slab may result in a strong asperity in case no hydrous weakening is applied in this region.*

the viscous coupling between the converging plates. This resisting force forms another torque in combination with the forced subduction of the buoyant plateau by the rest of the gravitationally unstable plate. The origin of both torques is similar: both result from the combination of resistance at the top of the slab and a driving force in the direction of the slab motion. All mechanism, proposed in this subsection, are implicitly incorporated in the numerical model. It is therefore difficult to distill the significance of each of these effects separately.

6.4.3   Evolution after plateau subduction

Since most slabs subduct rather steep and flat subduction occurs only at about 10% of the convergent zones (Gutscher et al., 2000b), we expect this geometry to be a transient phenomenon, for the duration of the plateau subduction, and to disappear afterwards. In our model results, however, the flat slab becomes a permanent feature, once it is initiated by the plateau subduction. Apparently, flat subduction is a stable feature in our model setup, and only needs to be triggered by the plateau subduction. In the former paragraph, we discussed mechanisms for the absence of subduction with an dip angle between 10 and 20 degrees. These mechanisms could also be responsible for the absence of the 're-steepening' of the slab, as they offer a preference for the slab to stick to the overlying continent. Yet another explanation could come from the two-dimensionality of the model: inflow of asthenospheric mantle material is necessary to separate the slab from the overriding continent again. In a 2-D model, this flow can only come from the 'inland' direction, perpendicular to the trench. In a 3-D model, this asthenospheric inflow is also possible along-trench from an area of steeper subduction, where a mantle wedge still separates the subducting and overlying plates.

6.4.4   Other mechanisms and shallow flat slab observations

For the subduction zone at the Nankai Trough near Japan, a flat slab is present at a distance of at least 200 km from the trench (Sacks, 1983; Gutscher et al., 2000b). Direct comparison with the maximum distance between trench and the modeled flat slab is not possible due to the absence of a forebulge in our model, which overestimates the horizontal extent of the 'fore-arc'. Therefore, we prefer to compare the observed length of the actual flat slab segment with the one from our model calculations. Subtracting the initial steeper part of the subduction zone from the trench to a depth of about 100 km, leaves a flat slab length of approximately 100 km below Japan. Our model results suggest, that this could well be explained with the discussed effects from the subduction of the Palau-Kyushu Ridge. Below Peru and Central Chile, however, a flat slab is observed more than 700 km from the trench (Gutscher et al., 2000b). Subtracting again the part at which the slab subducts from the surface to a depth of 100 km depth, results in an actual flat slab segment of about 400 to 500 km length. The performed model calculations generally do not show a flat slab of such size. The displayed model results in Figure 6.5 mostly show a maximum flat slab length between 200 and 300 kms. As discussed above, this length should be regarded as an upperbound in case of a continuous lateral slab across the edge of the plateau. The dynamical pressure effect as discussed in (Tovish et al., 1978) is implicitly included in our viscous flow model. The spatial and temporal correlation between the subducting oceanic Nazca Ridge and Juan Fernandez Ridge and the occurrence of the Peru and Central Chile flat slab regions, respectively, strongly suggest a causal relation, but the buoyancy and strength of a subducting oceanic plateau seem to be insufficient to explain the flat slab extent of 400 to 500 km. Lithospheric doubling has been proposed as an alternative mechanism to explain shallow flat subduction (Vlaar, 1983; van Hunen et al., 2000). In this mechanism, an active trenchward motion of the overriding continent is responsible for the flattening of a slab. Indeed, the continent of South-America has a westward absolute motion of about 3 cm/yr with respect to the hotspot reference frame (Olbertz et al., 1997; Olbertz, 1997). The combined effects of the subducting plateau and the trenchward overriding plate motion is probably most successful in explaining the flat subduction below Peru and Central Chile. The numerical results from this study confirm to a large extent the qualitative conclusions, based on observations from (Cross and Pilger, 1982) that the subduction dip angle is determined by the combined effects from the absolute (trenchward) overriding plate motion, convergence rate, the presence of subducting seamounts, aseismic ridges or oceanic plateaus and finally by the age of the subducting plate (see also Vlaar and Wortel, 1976).

The formation of the Rocky Mountains during the Sevier-Laramide orogeny has been attributed to flat subduction (Dickinson and Snyder, 1978), with a maximum flat slab segment as long as 1500 km approximately 65 Ma ago. The presented model results show that the subduction of an oceanic plateau is not capable of the creation of a flat slab segment of this extent. Besides, the distribution of igneous activity from 60 to 35 Ma (Dickinson and Snyder, 1978) shows a continuous and much larger north-south extending flat subduction event than is the case for the flat subduction below South America today. Although the buoyancy of subducting plateaus can certainly have contributed, the proposed westward

motion of North America of about 5 cm/yr from 60 to 45 Ma (Engebretson et al., 1985) suggest that lithospheric doubling was the dominant mechanism of the Laramide shallow flat subduction.

6.5   Conclusion

As an attempt to explain the occurrence of flat subduction at approximately 10% of the Earth's subduction zones, the subduction of buoyant oceanic plateaus has been proposed as a possible mechanism. We applied a two-dimensional finite element model to examine the physical circumstances for which a subducting plateau causes shallow flat subduction. We performed a series of model calculations to determine the most influencing physical model parameters in this process. The most important criterion for the occurrence of a flat-subducting plateau is the presence of metastable basalt in the eclogite stability field. Model calculations on a 44-Ma subducting slab demonstrate that basalt should be able to survive a temperature of at least 600-700°C to keep the plateau buoyant sufficiently long to cause a flat slab segment. These models further showed that yield stresses in the slab should not exceed 600 MPa to allow for the necessary bending of the slab to change its dip. Furthermore, the strength of the bottom of the continent and the mantle wedge is a critical factor in the development of a flat slab segment, and our simulations suggest that hydrous weakening of this region above the slab should be at least one order of magnitude to allow for the deformation that is required to change the style of subduction.

In most model calculations, the length of an occurring flat slab segment was limited to about 300 km. The limited metastability of the oceanic basaltic crust and the decreasing strength of the slab during its journey through the mantle do not allow for further horizontal movement. This is likely to be sufficient for the flat slab occurrence at the Nankai Trough, but addition of another mechanism, like lithospheric doubling, is necessary to explain a flat slab segment as far as 700 km from the trench, as proposed below Peru or Central Chile today or an even larger flat slab region of about 1500 km below the western USA around 65 Ma ago.

Chapter 7

The importance of the South-American plate motion and the Nazca Ridge subduction on flat subduction below South Peru

Abstract

Flat subduction near Peru occurs only where the thickened crust of the Nazca Ridge subducts. Furthermore, the South-American continent shows a westward absolute plate motion. Both the overriding motion of South America and the subduction of the Nazca Ridge have been proposed to explain the flat slab segment below South Peru. We have conducted a series of numerical model experiments to investigate the relative importance of both mechanisms. Results suggest that the average upper mantle viscosity should be about 3.5×10^{20} Pa s or less and basaltic crust should be able to survive 600 to 800°C ambient temperature before transforming into eclogite to explain the slab geometry below Peru. The effect of the overriding plate is estimated to be one to two times larger than that of the plateau subduction.

7.1   Introduction

It is widely believed that the gravitational instability of a subducting slab forms the main driving force in the process of plate tectonics (Forsyth and Uyeda, 1975). However, the presence of shallow horizontal subduction does not fit into this model. Modern flat subduction is most clearly observed below Peru and Central Chile (Jarrard, 1986), where a flat slab segment is present as far as 700 km inland. Several mechanisms have been proposed to explain the presence of flat subduction. A westward motion of South America has been suggested to lead to shallow flat subduction (Cross and Pilger, 1978; Vlaar, 1983; van Hunen et al., 2000). Alternatively, buoyant subducting lithosphere has been proposed to explain flat subduction (Cross and Pilger, 1978; McGeary et al., 1985; Gutscher et al., 2000b). Young oceanic lithosphere may be buoyant during a period of 30-40 Ma after formation. Oceanic plateaus, aseismic ridges and seamount chains all contain a thickened basaltic crust and underlying harzburgite layer, which provide compositional buoyancy for older slabs. The Nazca Ridge below South Peru and the Juan Fernandez seamount chain below Central Chile are proposed as the cause for flat subduction below South-America. Other mechanisms have been proposed as well, such as a non-hydrostatic pressure force (Jischke, 1975) or a slab suction force (Tovish et al., 1978). In principle, such mechanisms apply to any subduction zone, but their contribution might be most relevant to areas of low-angle subduction. Here, we study the relative importance of the 3-cm/yr trenchward motion of the South-American continent (Olbertz, 1997; Olbertz et al., 1997) and the subduction of the Nazca Ridge (with a 2.5 times thicker-than-average crust and harzburgite layer (McGeary et al., 1985)) on the development of approximately 400 km of flat slab below Peru.

7.2   Model setup and numerical methods

We performed the numerical model simulations with a two-dimensional finite element model. Using the extended Boussinesq approximations and an infinite Prandtl number fluid, we solve for the conservation of mass, momentum, energy and composition (van Hunen et al., 2000). The oceanic lithosphere is compositionally layered with a crust and depleted mantle layer (harzburgite) on top of undepleted mantle material. We use a composite rheology of temperature and pressure dependent diffusion and dislocation creep (van den Berg et al., 1993; Karato and Wu, 1993) for crust and mantle material separately, and a uniform stress limiter of 300 MPa. Hydrous weakening in the mantle wedge (Mei and Kohlstedt, 2000a,b; Karato, 2001) is included by means of a simple parameterization. Further elaboration of the effects of the yield strength in the slab and the effect of hydrous mantle wedge weakening on the development of a flat slab segment due to plateau subduction is given in Chapter 6. Mantle phase transitions, including latent heat effects (van Hunen et al., 2001), are incorporated in the model. Basalt-to-eclogite phase change kinetics are included in the model, using a parameterization from (Giunchi and Ricard, 1999), in which the kinetics are assumed to be purely determined by the ambient temperature and the Gibbs free energy values of the two phases. In this approach, the

reaction rate increases approximately exponentially with increasing temperature using a kinetic activation energy E_{kin}^*. Values for E_{kin}^* are chosen such, that the eclogitisation takes place within 20 Ma if the temperature equals a given transition temperature T_{tr}. Values for T_{tr} vary between 400 and 800°C in the presented model calculations. Calculations are performed in a 5200 km wide and 2000 km deep Cartesian model domain. For numerical convenience, the model reference frame is chosen fixed to the overriding continent. A 400-km-long region with an 18-km-thick crust and 45-km-thick harzburgitic layer defines the oceanic plateau. At model time $t = 0$, the leading edge of the plateau just enters the subduction zone. The vertical temperature distribution of the plateau is similar to the surrounding normal oceanic lithosphere, which has an age of 45 Ma at the trench. We assume, that the plateau buoyancy does not influence the convergence rate at the trench. Therefore, a constant convergence rate is imposed as a surface boundary condition on the subducting slab. A free-slip fault ensures total decoupling of the upper part of the converging plates, while for larger depth, the weak oceanic crust partly decouples the plates. More detailed descriptions of the model setup, rheology, initial conditions, fault implementation, as well as applied physical model parameters and numerical solution methods are given in (van Hunen et al., 2000, 2001).
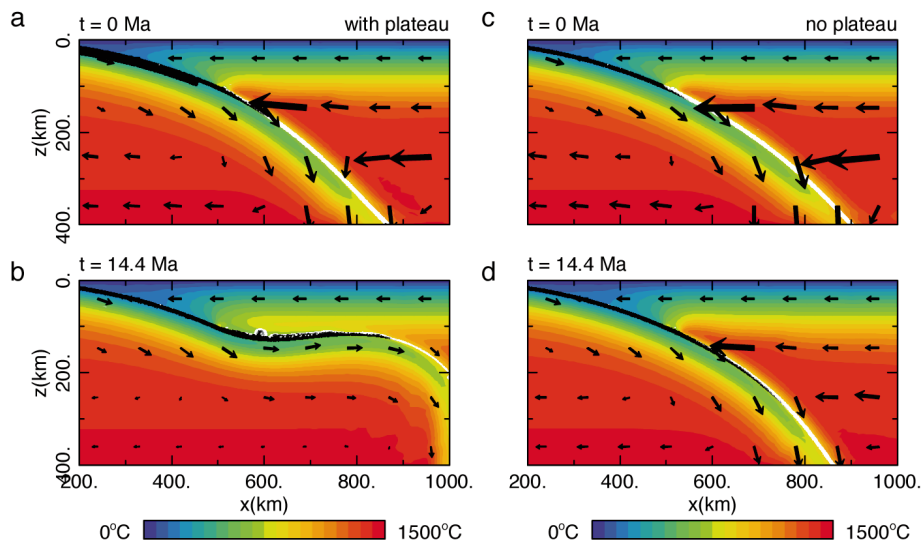

Figure 7.1: *Temperature plot (colors) of the subduction zone for model time $t = 0$ Ma and 14.4 Ma. Panels a and b show the development of a flat slab segment as a result of the subduction of an oceanic plateau. Panels c and d show the absence of a flat slab in case no plateau subducts. Arrows give the flow direction and velocity with respect to the deep mantle. Black and white areas show the basaltic and eclogitic parts of the crust, respectively.*

7.3   Obtaining sets of suitable model parameters

In a first series of model calculations, we define sets of model parameters that show shallow flat subduction in the presence of plateau subduction, and steeper subduction in the absence of a plateau (which is consistent with observations below Peru). Then, this set of models are modified: the plateau thickness is decreased or increased, and the overriding plate velocity is adapted to compensate for this modified plateau thickness, such that approximately the same slab geometry is obtained again. To reduce the amount of model calculations, we fixed most of the model parameters to a reasonable value. Absolute overriding plate motion (3.1 cm/yr) and convergence rate (6.7 cm/yr) are taken from (Olbertz, 1997; Olbertz et al., 1997). Data from (Jarrard, 1986) are used to fix the slab age (44 Ma) and intermediate dip angle (23° as an average value for all subduction zones). A free-slip fault extending to 100 km depth meets the requirement of weak plate margins (Zhong and Gurnis, 1996; Zhong et al., 1998). The thickness of the plateau crust was taken 18 km (McGeary et al., 1985), and the underlying harzburgite layer is taken proportionally thickened with respect to normal oceanic lithosphere. The mantle viscosity is an important parameter in the mechanism of flat subduction below a trenchward moving overlying plate (van Hunen et al., 2001), and different viscosity prefactors are chosen such that the average upper mantle viscosity η_{av} ranges from 2.0 to 6.5×10^{20} Pa s, which roughly satisfies results from post-glacial rebound studies (Lambeck et al., 1998). The extent of basalt metastability strongly influences the capacity of a buoyant plateau to flatten a slab. This mechanism implies a kinetically delayed basalt-to-eclogite transition. In this study, we examine a range of possible transition temperatures T_{tr} from 400 to 800^oC, as suggested by geological observations (Hacker, 1996; Austrheim, 1998). Figure 7.1 shows the temperature distribution for one set of model calculations ($\eta_{av} = 3.5 \times 10^{20}$ Pa s and $T_{tr} = 700^o$C), which satisfies the observations for the Peru subduction area. Panels a and b show the slab geometry before and after the subduction of the plateau. The compositional buoyancy of the basalt is large enough to gradually change the slab geometry and to create a flat slab segment of a few hundred km. Panels c and d show the same time snapshots for a model without a subducting plateau, where the normal crust is not buoyant enough to create a flat slab segment. Figure 7.2a shows the development of the slab geometry in time for the models with (bp) and without (nobp) a plateau from Figure 7.1. The length of the flat slab segment is defined as the horizontal position where the (rheological core of the) slab exceeds the depth of 200 km with respect to the situation in Fig. 7.1c. During the subduction of the plateau, sub-horizontal subduction is initiated and a flat slab segment starts to develop.

Figure 7.2b combines results of several model runs for different mantle strength and extent of the basalt-metastability by showing the resulting flat slab length at model time $t = 14.4$ Ma. The tendency to develop a flat slab segment is increased with both an increased basalt metastability (by increasing T_{tr}) and a stronger mantle (by increasing η_{av}). These effects operate in different ways. An increased mantle viscosity affects the slab dip angle in all models, regardless of the presence of a plateau, while in increased basalt metastability has a larger impact on a plateau than on normal oceanic lithosphere. Models with $\eta_{av} = 6.5 \times 10^{20}$ Pa s, therefore, all show flat subduction, even without

a plateau and for any basalt metastability. Since this type of model cannot explain the observed style of subduction below Peru, we excluded this set of models from further investigation. Models with $\eta_{av} = 3.5 \times 10^{20}$ Pa s and $T_{tr} = 600$ or 700^oC (hereafter referred to as models A and B, respectively), and the model with $\eta_{av} = 2 \times 10^{20}$ Pa s and $T_{tr} = 800^oC$ (hereafter model C), however, give slab geometries that are consistent with observations.

7.4 The relative importance of both mechanisms

We use these models A, B, and C to further investigate the relative importance of the two flattening mechanisms. We proceed by increasing or decreasing the plateau thickness of the plateau in each model with 11 km. This gives a plateau thickness of 7 km (which is a normal oceanic crustal thickness and not a plateau anymore, model NOBP) or 29 km (model LBP). The trenchward motion of the overriding plate is then adapted from the reference value (3.1 cm/yr) in steps of 0.5 cm/yr until approximately the same (flat) slab geometry is again obtained. Results are shown in Figure 7.3. For model A, the increased plateau thickness (LBP) and removal (NOBP) of the plateau are best compensated by a 1.5-cm/yr decrease and increase, respectively, of the overriding plate velocity v_{ov}. In case of model B, removal of the plateau (NOBP) requires an increase of the overriding plate velocity $\Delta v_{ov} = 2$ cm/yr to obtain the same flat slab segment. Comparison with the $\Delta v_{ov} = 1.5$ cm/yr in model A reflects the larger impact of a plateau in case of more extensive basalt-metastability. The increased plateau thickness (LBP), however, is compensated by $\Delta v_{ov} = -1$ cm/yr only: the flat slab segment is already large for a normal plateau (almost 400 km), and a further increase of the plateau thickness has only a limited effect. Comparison of models A and B with model C shows the effect of the decreased mantle strength in the latter: the overriding plate motion is less effective in flattening the slab, and the plateau effect is compensated by a change in the overriding plate motion of 2.5 to 3 cm/yr. Combining these results shows that the ability of the thickened oceanic crust and harzburgite layers in the oceanic plateau to flatten the subducting slab is roughly equal to the effect of a 1.5 to 3.0 cm/yr increase of the overriding plate velocity, depending on the mantle strength and the effective metastability of the basaltic crust. This implies that the South-American westward absolute plate motion (3.1 cm/yr) is approximately one to two times more important than the effect of the subducting Nazca Ridge for the creation of the Peru flat slab region.

7.5 Discussion and concluding remarks

We investigated the relative importance of the westward absolute plate motion of the South-American continent, and the subduction of the Nazca Ridge, an oceanic plateau with thickened crust and harzburgite layer, on the development of the Peru flat slab region. With a simple model setup, we are able to model the essential features for such study: a 40-50 Ma old slab, which converges with about 6.7 cm/yr with a 3 cm/yr-overriding con-
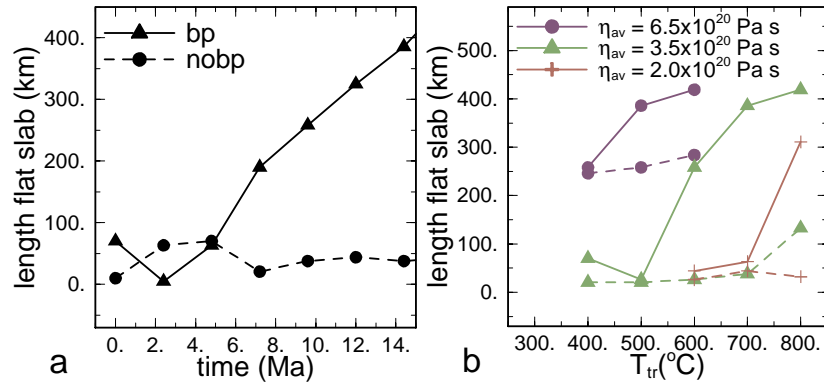
Figure 7.2: *a) Development of the flat slab segment in time for the models with (bp) and without (nobp) an oceanic plateau in Figure 7.1. b) Length of the flat slab segment at model time $t = 14.4$ Ma for several transition temperatures T_{tr} and effective upper mantle viscosities η_{av}.*

tinent, shows flat subduction only when an oceanic plateau like the Nazca ridge subducts. Variation of the plateau thickness and overriding plate motion in the numerical model allows for a comparison of the effects of the two mechanism, and suggests that the South-American absolute plate motion contributes to the flat slab development roughly one to two times more than the plateau subduction does.

Very few model results show a decreasing flat slab segment after full plateau subduction. One would expect such 're-steepening' to occur, since flat subduction occurs at only about 10% of the trenches (Gutscher et al., 2000b). Possible explanations are a slab suction force that is somewhat too effective, or the two-dimensional model used. Slab suction (Stevenson and Turner, 1977; Tovish et al., 1978) is implicitly incorporated in a viscous flow subduction model and is likely to be partly responsible for the flat slab development. This mechanism is proposed to explain the absence of observed subduction dip angles between 10 and 20 degrees. Indeed, such dip angles are also rare in the numerical calculations. Also the implicit absence of along-trench mantle flow in a 2-D model could reduce the ability of the flat slab segment to separate from the overlying continental lithosphere: such separation requires inflow of mantle material to form a new mantle wedge, that accompanies steep subduction. Lateral mantle flow might facilitate this process.

Fig. 7.2b shows that the transition temperature T_{tr} also affects the dip angle in models without a subducting plateau. The eclogitisation of the normal oceanic crust and the thickened plateau crust are controlled by the same function, in which only the Gibbs free energy difference between basalt and eclogite and the ambient temperature play a role. However, also the presence of water and deformation is suggested to enhance eclogitisation significantly (Rubie, 1990; Austrheim, 1998). Extension of the kinetic function with a hydration dependence could result in a larger metastability in the deeper parts of
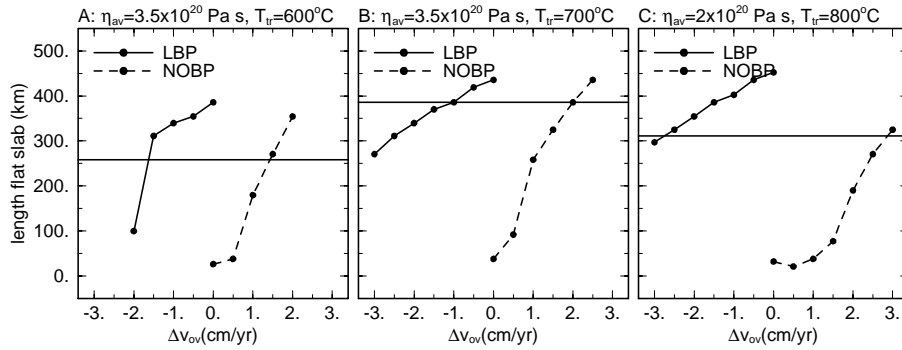
Figure 7.3: *Display of the relative importance of the overriding plate motion and the plateau subduction of models A, B, and C (see text) at time $t = 14.4$ Ma. Model A) The horizontal line represents the flat slab length from Fig. 7.2b. The LBP- and NOBP-models show that an overriding velocity change $\Delta v_{ov} \approx \pm 1.5$ cm/yr compensates the effect of a plateau. Model B) A doubled plateau thickness is compensated by a $\Delta v_{ov} = -1$ cm/yr, while removal of the plateau is compensated by a $\Delta v_{ov} = +2$ cm/yr. Model C) The plateau is compensated by a Δv_{ov} of 2.5 to 3 cm/yr.*

the plateau, while 'normal' oceanic lithosphere could be more hydrated and show faster eclogitisation. The influence of water on eclogitisation and even the (de)hydration of the slab, however, are poorly constrained.

Chapter 8

The viability and style of the modern plate-tectonic subduction process in a hotter Earth

8.1 Introduction

It is widely believed that the Earth has been cooling steadily, and was warmer during the Archean and Proterozoic. How much warmer is not easily answered, and has led to considerable debate. On the one hand, Archean high Mg-komatiites suggest a high mantle temperature up to 350 K more than at present. On the other hand, Archean high grade terrains suggest that geotherms in continental crust have not changed much since the Archean (England and Bickle, 1984; Bickle, 1986; Vlaar, 1986a; Herzberg, 1992; de Wit, 1998). The importance of this debate lies in the geodynamical consequences: a different mantle temperature could have a large impact on the type and vigor of the dominant tectonic regime. First, the mantle viscosity drops by approximately one order of magnitude for each 100 K temperature increase, with an associated increase of the vigor of convection. Furthermore, a hotter mantle gives rise to more pressure-release partial melting, which results in a thicker basaltic oceanic crust and underlying residual harzburgitic layer (Vlaar and van den Berg, 1991). Since both basalt and harzburgite are less dense than their lherzolitic source rock, buoyancy of the lithosphere is increasing with increasing amount of partial melting. The present-day plate tectonic mechanism is based on the gravitational instability of the subducting slabs. If plates remain buoyant, they cannot drive subduction. These ideas have raised the question about the effectiveness of plate tectonics in a hotter Earth (Vlaar, 1986a; Vlaar and van den Berg, 1991; Davies, 1992). Only very old plates would eventually become instable enough to drive the subduction process. However, an increase of the average plate age implies a decrease of either the amount of mid-ocean ridges or a decrease in the spreading rate, and would result in a decreasing

95

effectiveness of the plate tectonic mechanism to cool the Earth. Within the plate-tectonic framework, several solutions to this problem are proposed. Vlaar (1986b), for example, suggests that shallow subduction of the buoyant lithosphere below trenchward moving overriding plates, or lithospheric doubling, could have been the dominant style of sub-duction during the Proterozoic. Abbott et al. (1994) suggest that buoyant, flat subduction was the dominant style of subduction before 1.6 to 2.0 Ga. Alternatively, the basalt-to-eclogite transition in the crust would remove the compositional buoyancy, but this effect is not easily quantified. The equilibrium depth of this transition is at 60-70 km, but the re-action is known to be kinetically slow, and basalt could remain metastable to large depths and temperatures (Hacker, 1996; Austrheim, 1998). Alternatives for Archean plate tec-tonics have been proposed to cool the Earth and recycle crustal material. The lowermost Archean crust may have been ductile and weak, and could have resulted in a lithosphere that was not mechanically coherent, but rather had a sandwich-like rheology (Hoffman and Ranalli, 1988). Delamination of the buoyant crust from the dense underlying man-tle lithosphere would then be an alternative to overcome the buoyancy problem, and this mechanism, termed flake tectonics, has been proposed to form the characteristic Archean greenstone belts. Mass balance calculations, however, show that most of the crust has not been preserved and must have been recycled into the mantle (Hoffman and Ranalli, 1988; Rudnick et al., 2000). Vlaar et al. (1994) proposed 'mini'-subduction within the weak thick crust, subsequent eclogitisation of the lowermost crust, and sinking of these eclogitic parts through the underlying harzburgitic layer. The associated (re)melting and solidification processes could account for the mantle cooling of several 100 degrees dur-ing the Archean.

Geological and geochemical observations do not seem to have reached consensus about the dominant type of tectonic regime in the Precambrian. On the one hand, for example, a reported 2.5 Ga-old ophiolite complex suggests plate tectonic processes since the Late Archean (Kusky et al., 2001), and de Wit (1998) proposes modern plate tecton-ics since the Early Archean (4.0-4.2 Ga). On the other hand, Hamilton (1998) suggest that voluminous magmatism dominated the Earth's cooling during the Archean and plate tectonics only started some two billion years ago, in the Proterozoic. Furthermore geo-chemical resemblance between Archean tonalite-trondhjemite-granodiorite (TTG) series and Cenozoic adakites derived from slab melting (Drummond and Defant, 1990) seem to provide evidence for Archean plate tectonics, but Smithies (2000) suggests that only either flat subduction or a different tectonic regime could explain the geochemical signa-ture of TTG's. Bailey (1999) proposes continental gravitational spreading or overflow to underthrust adjacent oceanic lithosphere and generate TTG's.

In spite of the large number of theoretical considerations and geological and geo-chemical observations that favor either the absence or presence of plate tectonics in a hotter Earth, its viability has not been examined through dynamical modeling. A mini-mum requirement for the presence of plate tectonics in a hotter Earth is that the subduction process can be operative in some form. In this chapter, we examine the presence, vigor, and style of the subduction process in a hotter Earth. In a first set of models, the style and vigor of the subduction process below a trenchward moving plate is examined for dif-ferent mantle temperatures. Then the continuation of modern 'Benioff-type' subduction,

once initiated, is studied, again as a function of the mantle temperature.

8.2   Model description

A set of numerical model experiments is performed to examine the effects of a changing mantle temperature on the viability, vigor, and style of the subduction process as an essential part of the plate tectonic mechanism. To do so, the potential temperature of the mantle is varied from 1300^oC, as a present-day value, up to 1600^oC for a younger Earth. The impact of a hotter mantle on the dynamics of plate tectonics is dominated by two processes. First, an increase of the mantle temperature gives rise to increased partial melting of fertile upper mantle material (lherzolite), and results in thicker crustal and harzburgitic layers. Table 8.2 gives the applied potential temperatures in the model calculations and their associated crustal and harzburgitic layer thicknesses. Values are adopted from (Vlaar and van den Berg, 1991). For the present day situation (with a 7 km thick crust), we assumed a 36 km thick harzburgitic layer, of which the density difference with the underlying undepleted lherzolite $\delta\rho$ tapers linearly from -77 kg/m^3 at its top, to 0 kg/m^3 at its bottom.

$T_{pot}(^oC)$	d_{crust}(km)	d_{hz}(km)
1300	7	36
1338	9	46
1375	11	57
1450	15	77
1525	22	113
1600	30	108

Table 8.1: *Crustal thickness d_{crust} and harzburgitic thickness d_{hz} corresponding to the applied potential temperatures of the model calculations.*

When basalt (with $\delta\rho = -400$ kg/m^3 with respect to fertile mantle material) transforms into eclogite (with $\delta\rho = +200$ kg/m^3), the compositional buoyancy terms of the crust and harzburgite approximately cancel. For higher mantle temperatures, the same ratio of crustal to harzburgitic thickness is assumed. Second, a warmer mantle is weaker due to the temperature dependence in the rheological flow laws. As a rule of thumb, the viscosity of the mantle decreases with one order of magnitude for every 100 degrees temperature increase. This affects the coupling between mantle and plates, the ability of the plates to decend into the mantle, and the strength of the slabs (van Hunen et al., 2000).

Eclogitisation of the crust could be a mechanism to remove the compositional buoyancy of the slab and allow for its subduction. Not-subducted oceanic crust, however, seldom reaches the eclogite stability field, and the stably stratified oceanic lithosphere will not subduct in the absence of external forces. Active trenchward motion of an overriding plate, or lithospheric doubling, was proposed as a possible mechanism to force

the subduction process to occur, and to result in low-angle subduction, in case of a low basalt-to-eclogite reaction rate (Vlaar, 1986b). In a first set of experiments, the ability of a 'drifting' continent to override neighboring oceanic lithosphere and to cause flat subduction in a hotter Earth is examined. The effect of a thicker oceanic crust and harzburgite layer and weaker mantle on the overriding process is examined. To do so, a 45-Ma old 'oceanic'-type lithosphere with compositional layering as described above is positioned next to a 'continental' lithosphere with a steady state equilibrium geotherm. The relatively low age of the oceanic lithosphere was chosen to satisfy the constraint that extra spreading activity was necessary to dissipate the heat from the hotter mantle (Hoffman and Ranalli, 1988). This implies either an increased total ridge length or an increased spreading rate, and both result in subduction of oceanic lithosphere of a decreased age.

The continent was defined to have a trenchward motion of 5 cm/yr with respect to the deep mantle. Ideally, the examination of plate tectonics in a hotter Earth includes the initiation of subduction by creation of a new convergence zone. This process is clearly distinct from subduction continuation (Cloetingh et al., 1984; Toth and Gurnis, 1998; Branlund et al., 2001). Here, we restrict ourselves to situations in which the subduction zone has already developed: the two lithospheres are separated on the contact by a free-slip fault that extends to 100 km deep.

If subduction would only proceed if it is continuously forced by a mechanism such as lithospheric doubling, this would imply a type of plate-tectonic regime which is different from the present-day one. Today, oceanic plates continuously subduct primarily because of slab pull forces, and external forces are not required to keep this process going. In a second set of experiments, the viability of the present-day plate-tectonic process is examined for a higher mantle temperature. We investigate whether a hotter Earth would still provide the necessary conditions for the continuation of the subduction process, once it has been initiated. In these experiments, the initial stage of the subduction process is again enabled through lithospheric doubling, but after convergence over some distance, the overriding plate motion is removed, and the subduction process without external driving forces can then be examined.

The general model setup is defined in Chapter 2. Section 2.5 gives the model geometry and applied boundary conditions. Section 2.4.2 describes the incorporation of the kinetics of the basalt-to-eclogite phase transition. The metastability of the basalt phase is parameterized as a function that depends on the Gibbs free energy of both phases, which determines the stability fields of both phases, and the ambient temperature. A transition temperature T_{tr} is defined such that half of the reaction takes place within 10 Ma, if the ambient temperature $T = T_{tr}$. A composite rheology of diffusion creep, dislocation creep, and a stress-limiting mechanism was applied, with different parameters for crust and mantle material. The rheological parameters for the deformation of both materials are modified from the creep parameters from (Karato and Wu, 1993) and (Shelton and Tullis, 1981) for mantle and crustal material, respectively, and the applied parameter values are given in Table 8.2. The present-day potential temperature is assumed to be 1300^oC, and rheological prefactors are adapted to obtain a reasonable fit with post-glacial rebound results. Chapter 2.2.1 deals with a more elaborate description of the mantle rheology. The stress-limiting rheology parameters are equal to the ones applied in Chapter 6 with a yield

material	mechanism	$A(\mathrm{Pa^{-n}/s})$	n	$E^*(\mathrm{J/mol})$	$V^*(\mathrm{cm^3/mol})$
crust	dislocation creep	8.8×10^{-19}	3.4	260×10^3	10
mantle	diffusion creep	3.04×10^{-11}	1.0	300×10^3	4.5
mantle	dislocation creep	3.84×10^{-16}	3.5	540×10^3	14.5

Table 8.2: *Rheology parameters for the deformation mechanisms of crust and mantle material. Crustal diffusion creep is not applied.*

stress of 200 MPa.

8.3   Subduction below an overriding plate

The process of subduction below an trenchward moving overriding plate, or lithospheric doubling, is examined for several mantle temperatures. Figure 8.1 shows the results for
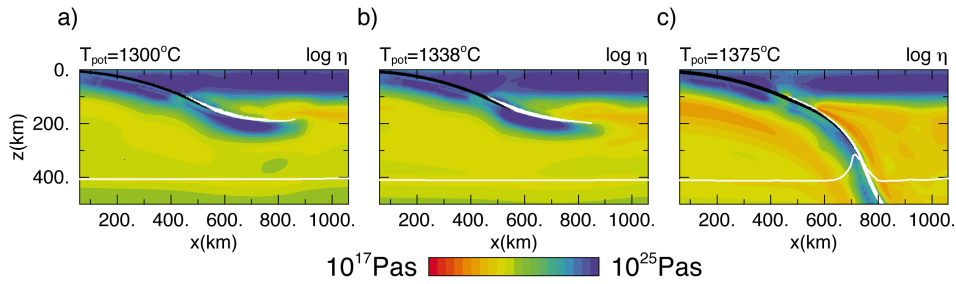

Figure 8.1: *Viscosity plot of subduction process below an trenchward moving overriding continent at $t = 12.8$ Ma after model initiation. Colors represent the effective mantle viscosity, while black and white areas refer to basaltic and eclogitic crust, respectively. Potential temperature: a) $T_{pot} = 1300^oC$, b) $T_{pot} = 1338^oC$, c) $T_{pot} = 1375^oC$. The white line at 400 km depth represents the olivine/spinel phase boundary.*

1300, 1338, and 1375^oC potential temperature. For these results, a moderate basalt metastability was applied, by choosing the transition temperature $T_{tr} = 500^oC$. These results show that for a small potential temperature increase of 38 K, the overriding plate still causes flat subduction, but for a potential temperature increase of 75 K, the style of subduction is steep. This variation in subduction style is reflected in the convergence velocity between the overriding and the subducting plate. During flat subduction, the subducting lithosphere is positioned rather passively on the underlying mantle, which results in a convergence velocity that approximately equals the overriding velocity of the obducting plate. In case of steep 'Benioff-type' subduction, the subducting plate sinks through the mantle below, which results in a considerably larger convergence velocity. This is

shown in Figure 8.2, where the dotted lines show the convergence velocity of the model calculations from Figure 8.1, measured at the trench.
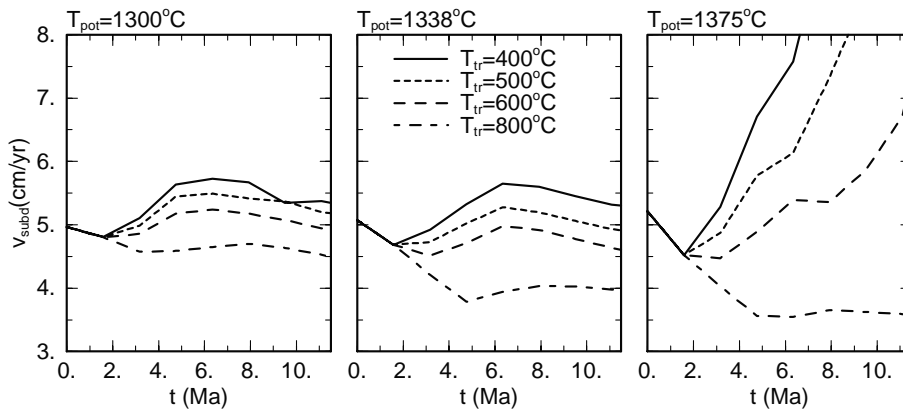

Figure 8.2: *Convergence velocity during subduction below a trenchward moving overriding continent for different values the transition temperature T_{tr}, which determines the amount of basalt metastability and potential temperatures T_{pot}.*

To determine the importance of the basalt metastability on the subduction style, the transition temperature T_{tr} was varied between 400° and 800^oC. This range resembles the geologically observed range (Hacker, 1996; Austrheim, 1998). The effect on the subduction process is rather small in case of the 1300^oC potential temperature. The convergence velocity decreases somewhat with increasing transition temperature as a result of the extra resistance against subduction of buoyant basaltic material. Apparently, the varying buoyancy of the crust does not change the style of subduction. For $T_{pot} = 1338^o$C, the influence of the basalt metastability is larger due to the thicker crust (9 instead of 7 km), but again flat subduction occurs for all transition temperatures. In case of $T_{pot} = 1375^o$C, the basalt metastability determines the style of subduction: for transition temperatures up to 600^oC, steep subduction occurs, while for 800^oC, flat subduction occurs due to the delayed eclogitisation. This is again reflected by the low convergence velocity.

Model calculations were performed at even higher potential temperatures than 1375^oC, representative for a younger Earth. All calculations showed steep subduction for transition temperatures up to 600^oC, while for higher transition temperatures, no subduction occurred at all. For high transition temperatures, basalt metastability is significant, which, in case of a relatively hot mantle, results in considerable resistance against obduction, and may lead to collison: the low coupling between the oceanic plate and the weak underlying mantle may not provide the necessary reaction force for the lithospheric doubling process, and collision instead of convergence results. The change in style of subduction from flat to steep for increasing potential temperature is explained by the weaker mantle at higher temperature, which allows a gravitationally unstable slab to subduct more easily. Further-

more, a higher mantle viscosity increases the coupling between the subducting plate and the underlying mantle and facilitates convergence and the development of a flat slab during lithospheric doubling (van Hunen et al., 2000). Once descending has been initiated, the slab pull becomes more effective, which reinforces the process of steep subduction.

8.4 The viability of modern plate tectonics in a hotter Earth

In the next set of experiments, we quantified the possible operation of modern plate tectonics in a hotter Earth. An essential requirement for this is the ability of the plate tectonic process to provide conditions for its own continuation. As in the section 8.3, we used the mechanism of a trenchward moving overriding lithosphere to overcome the buoyancy problem during the initial stage of subduction of a stably stratified oceanic lithosphere with a thick basaltic crust. In order to study the self-regulating characteristics of the plate tectonic process, the overriding plate motion was only used to trigger the subduction. Once eclogitisation occurred and convergence velocity exceeded the overriding plate velocity, the absolute overriding plate motion is set to zero. Results are shown in Figure 8.3. The top panels show the convergence velocity (v_{conv}) and root-mean-square velocity (v_{rms}) of the total model domain with respect to the overriding continent for model calculations with a transition temperature of 500^oC. For the present-day situation with an assumed 1300^oC potential temperature (Figure 8.3a), the initial stage of 4.8 Ma of subduction below an 5-cm/yr overriding plate is followed by a sudden drop in v_{conv} and v_{rms}, as a result of the removed overriding plate motion. Subduction then slowly develops until the slab reaches 400 km depth, and the subduction is reinforced by the extra phase buoyancy of the exothermic olivine-to-β-spinel phase transition. At reaching the 670-km phase transition, the subduction rate decreases again. This time-dependent subduction velocity pattern is similar to experiments described in Becker et al. (1999).

Figure 8.3b shows a similar experiment for a 1450^oC potential temperature, where different velocity and time scales are used in the top frame. After the initial overriding stage, v_{conv} and v_{rms} drop again, and a Benioff-type subduction zone again develops. The slab reaches the 400-km phase transition after 17 Ma, which indicates that the total process develops roughly twice as fast as for the $T_{pot} = 1300^oC$-situation. This is predominantly the result of the weaker mantle. The sharp spikes in the v_{rms} are the result of detachment of small pieces of eclogitic crust and the tip of the slab. These spikes are only observed during the first part of the model calculation, and disappear once a significant slab length has developed. The peak convergence rates over 25 cm/yr and the presence of a Benioff-type steep slab indicate the vigorous regime and viability of plate tectonics for a 150 K higher-than-today mantle temperature.

A further increase of the potential temperature to 1525^oC changes the results significantly (Figure 8.3c). The initial overriding plate motion stage was maintained for 6.4 Ma to create enough eclogite to provide the necessary gravitational instability to continue without an overriding plate. After the initial stage, however, the convergence rate further
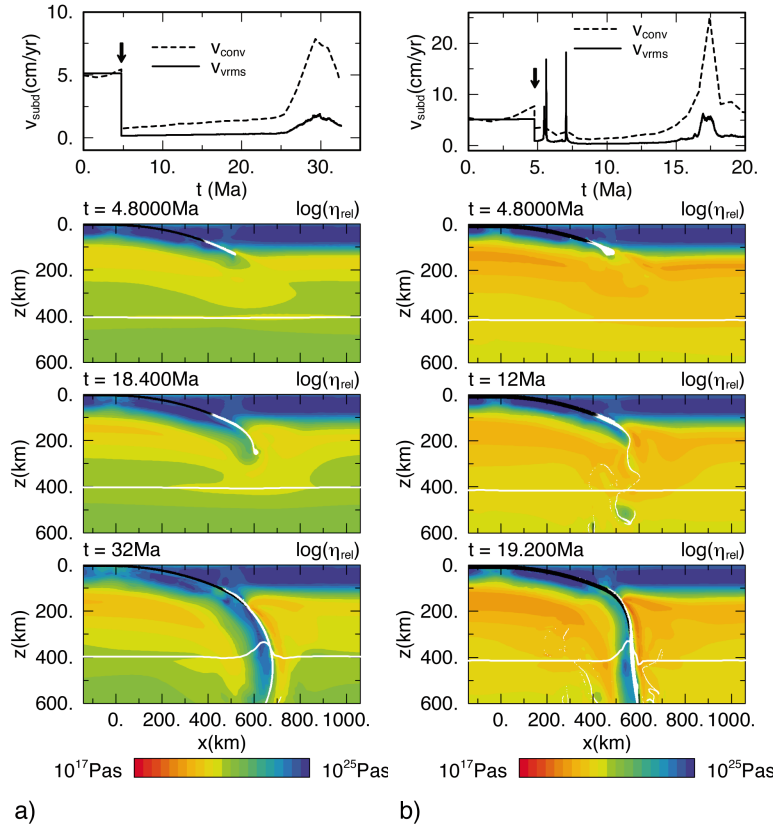
Figure 8.3: *Top panel: Convergence velocity v_{conv} and root-mean-square velocity v_{rms} with respect to the overlying continent during the subduction process at a potential temperature T_{pot} of a) 1300^oC, b) 1450^oC, c) 1525^oC, and d) 1600^oC. The subduction process is initiated by a period of trenchward motion of the overlying lithosphere. The sudden drop in the v_{conv} and v_{rms} below the arrow indicate the moment at which the overriding plate motion is set to zero. Lower three panels: time snapshots of the viscosity field for the subduction process.*

decreases to very low values. Smaller and larger spikes in the v_{rms} indicate several spin-ups, most likely because of delamination of eclogite parts of the subducting plate, but the viscosity plots do not show any detachment. A significant slab is not developing, due to the very low convergence rate. Apparently the plate is too buoyant to descend into the mantle. This might be the result of the delamination of the eclogitic part of the slab from its mantle lithosphere. The crustal material becomes very weak during re-heating in the subduction zone, and easily flows down into the mantle. The remaining part of the slab becomes more buoyant as a result of this process. The subduction process seems to be
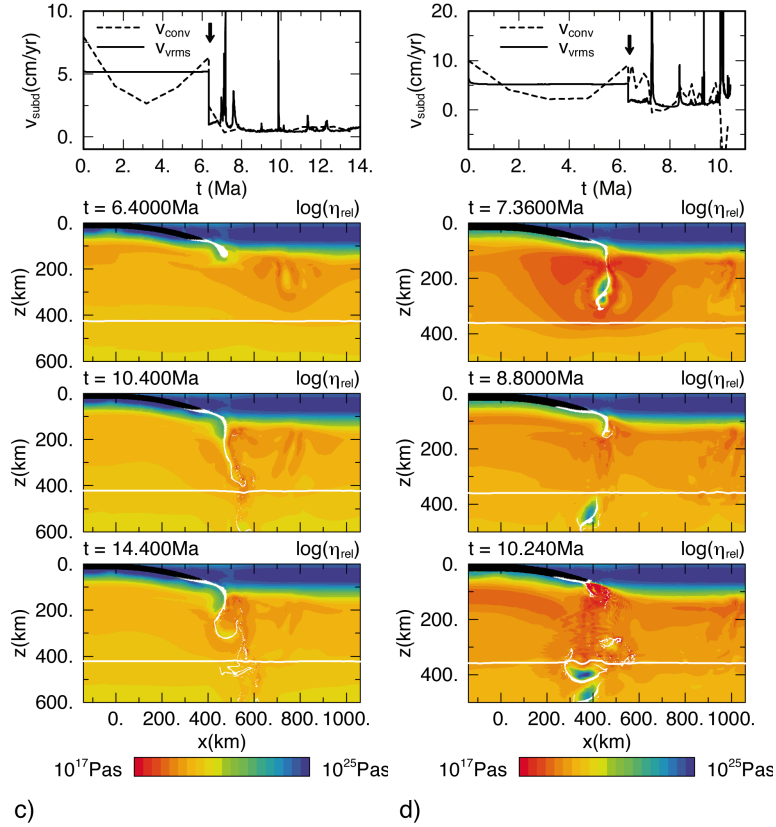
Figure 8.3: *Continued*

hampered by the separation of the dense and buoyant parts of the plate.

An increase in the mantle temperature results in a thinning of the total lithosphere, and an increase in the crustal thickness. This implies a decrease in the rheologically strong mantle part of the lithosphere. Figure 8.3d illustrates this in experiments with a further increased potential temperature to 1600^oC. The initial overriding stage was again maintained for 6.4 Ma. After this stage, the v_{conv} and v_{rms} indicate an irregular motion of the subducting plate. The average convergence rate is larger than for the $T_{pot} = 1525^oC$-case, which is a result of more extensive eclogitisation at the base of the crust, and associated increase in the gravitational instability of the plate. The base of the crust easily reaches the transition temperature of 500^oC, because it is extending to a depth which is near to the thermal base of the lithosphere. The viscosity plots show frequent detachment of small pieces of the slab. This results in large spikes in the v_{rms}, and sudden drops in the convergence rate. At 10 Ma, the slab breaks very shallowly, after which the convergence velocity even becomes negative for a while, and the total subduction process ceases, due

to removal of basically all slab pull.

In a following experiment, model calculations are repeated for different eclogitisation rates by variation of the transition temperature T_{tr} between 400 and 600°C to quantify the influence of the basalt-metastability. The convergence velocity for each of these calculations is compiled in Figure 8.4. For the 1300 and 1450°C potential temperature cases,
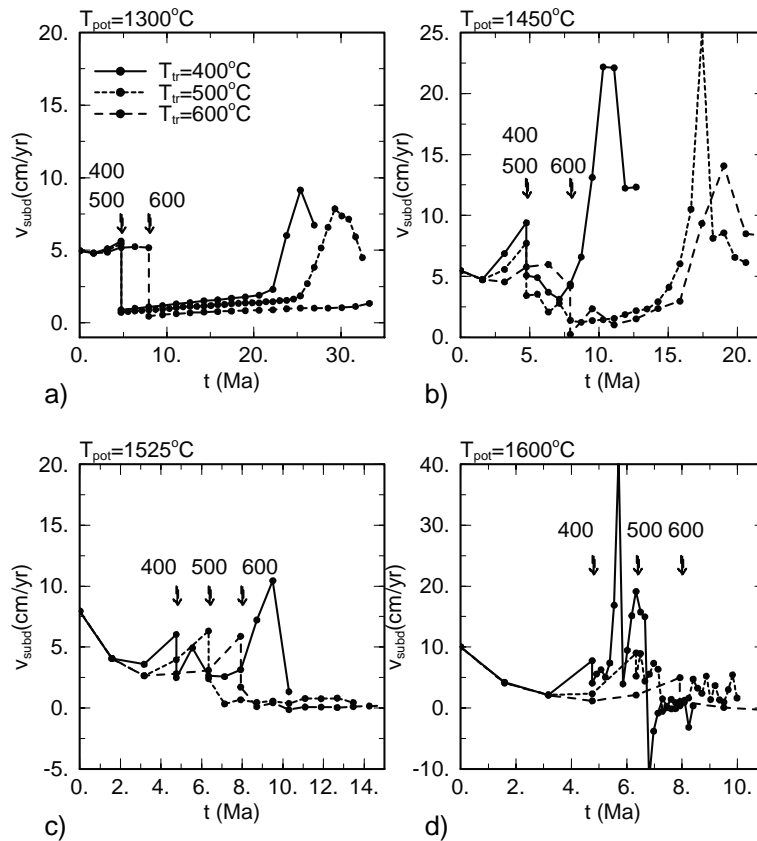

Figure 8.4: *Convergence velocity of the subduction process, during and after the period of active trenchward continental motion for transition temperatures of* 400°*C,* 500°*C, and* 600°*C. The end of the first period for each calculation is indicated by an arrow with the transition temperature.*

the rate of eclogitisation mainly affects the convergence rate of the subduction process. At $T_{pot} = 1525°$C, a slab develops in case of a low transition temperature $T_{tr} = 400°$C (high eclogitisation rate), and a convergence rate of 10 cm/yr is reached. After that, the weak eclogitic crust again delaminates from the crust and results in a decrease of the convergence rate. For the highest potential temperature $T_{pot} = 1600°$C and a fast

eclogitisation rate $T_{tr} = 400^oC$, the subduction process is very vigorous and irregular by alternating subduction and necking of the subducted lithosphere. A final shallow detachment again puts an end to the total subduction process. An increase of the basalt metastability to $T_{tr} = 600^oC$ results in complete blocking of the subduction process for both $T_{pot} = 1525^oC$ and $T_{pot} = 1600^oC$.

These model calculations show that the subduction process does not simply cease or continue with increasing potential temperature. The several rheological consequences of the hotter Earth both favor and hinder a rapid subduction process. The weaker mantle decreases mantle drag on the plates, which facilitates rapid Benioff-type subduction, but complicates subduction below a trenchward moving overriding plate. The thickened weak oceanic crust, resulting from increased partial melting of mantle material, on the one hand allows for a better decoupling between the converging plates, but on the other hand may induce delamination of the dense and weak eclogite from the rest of the slab during its sub-vertical descend. Finally, the rheological mantle part of the lithosphere is thinner, because of the combined effects of increased mantle temperature and crustal thickness, and facilitates bending at lower stresses. A minimum strength of the slab, however, is required to maintain the mechanical coherence of the slab during its descend and to avoid systematic necking of the slab. The buoyancy effects of the thickened crust in a mantle with higher potential temperature are more difficult to quantify due to the poorly constrained eclogitisation rates. The cold lithosphere has more negative thermal buoyancy with respect to the warmer mantle. Assuming an eclogitisation depth, which is more or less independent on the potential temperature implies a compositional buoyancy that increases roughly linearly with increasing crustal thickness, for either positive or negative compositional buoyancy. However, more rapid eclogitisation of the warm crustal base or delamination of eclogite during the slab descent would completely dominate the effective buoyancy.

8.5 Discussion

Today, crustal melting in a subducting slab is mainly restricted to very young and low-angle subduction zones (Defant and Drummond, 1993; Gutscher et al., 2000a). It is likely that in a warmer mantle, the solidus temperature of crustal material was more abundantly exceeded, and slab melting was a more common feature. It could have been responsible for the formation of an early continental crust. Slab melting is not incorporated in the numerical model. One expected effect of slab melting on the dynamics of the plate tectonic process in a hotter Earth could be delamination and upwelling of the slab material from the slab through the overlying mantle wedge to the surface. Removal of the crust and its associated buoyancy has an effect that is similar to the eclogite delamination, as described in the former section.

In the present-day plate tectonic process, crustal and harzburgitic layers become part of the lithosphere during cooling after their formation at the mid-ocean ridge. This implies that both layers subduct at the trench as part of the slab. As the thickness of both layers increases with increasing mantle temperature, part of the harzburgitic layer forms

the asthenosphere at potential temperatures higher than about 1450^oC. This part will not contribute to the slab buoyancy, which makes the slab gravitationally more instable. Another consequence is that, in case of subduction, this part will not subduct, which eventually will lead to a more depleted upper mantle, and may partly choke the formation of new crustal material (de Smet et al., 2000). This could lead to a thinner crust, lift the harzburgite layer to a shallower level, and allow for more harzburgite subduction to form a self-regulating system. The process of crust formation at the ridge is not explicitly incorporated into the numerical model setup, and the time span of the model calculations is too short to study this phenomenon.

The fault between the converging plates has a fixed and constant arc-shaped geometry in all model calculations, with a dip angle that increases from zero (horizontal) at the surface to about 23° at 100 km depth. Such dip angle corresponds well to the average observed intermediate-depth dip angles of the present-day subduction zones (Jarrard, 1986). Figure 8.3, however, illustrates that such dip angle seems to be too small for subduction zones in a hotter Earth. The weaker lithosphere bends more easily and would result in a smaller arc radius and a steeper dip angle at 100 km depth, if the fault geometry were not fixed. A possible solution to this problem would be the implementation of a mobile fault, of which the geometry adjusts to the stress and flow field (Zhong and Gurnis, 1995; Toth and Gurnis, 1998), although even then the subduction zone geometry would be dominated by its initial shape due to the relatively stiff overlying lithosphere and the relatively short time span of the model calculations.

An increased mantle temperature implies a more vigorous convective regime in the Earth, due to the larger Rayleigh number of the mantle. Mantle plumes might have been more abundant. The initially imposed adiabatic temperature distribution does not give rise to large-scale convection or mantle plumes, and a deep thermal boundary layer (at 670-km depth or at the core-mantle boundary) would be necessary to induce such features. The purpose of this study was mainly to investigate the possible role of the subduction process as part of the plate-tectonic mechanism. Incorporation of other mantle dynamic features, such as large-scale convection or plumes would make the calculations numerically less feasible and results more difficult to interpret. Therefore, we decided to study the subduction process in a hotter Earth as a separated process, and assumed that the results are little affected by interaction with mantle plumes and convection.

For the highest potential temperature $T_{pot} = 1600^o$C in the experiments, the oceanic plate becomes very weak, and events of delamination or detachment of slab material, soon after entering the mantle, dominate and eventually terminate subduction. These processes occur on a rather small scale, but they show similarities with slab detachment, as observed today in three-dimensional settings in final stages of a subduction process, for example at the closure of an oceanic basin due to increased resistance against subduction at continent-continent collision (Wortel and Spakman, 1992, 2000). For such setting, it has been suggested that slab detachment of the relatively strong subducting plate operates by lateral migration of the tear along strike of the subduction zone, and is facilitated by stress concentration at the point of detachment (Yoshioka and Wortel, 1995). The negative convergence velocity, as shown in Figure 8.4 can be associated with the geologically and numerically observed surface uplift as a result of slab detachment (van der Meulen

et al., 2000; Buiter, 2000). The frequency and size of these events in a hotter mantle, however, differ significantly from the present-day slab detachment events. Figure 8.3d shows dripping of pieces of the slab of about 100 km in size, approximately every million years, while present-day slab detachment usually concerns break-off of the total slab, and occurs only once during a plate-tectonic cycle. The depth of slab detachment in the presented model results might be influenced by the choice of the fault dip angle, since the increased bending of the slab at about 100 km depth causes strain weakening due to the non-linear dependence between stress and strainrate, and may provide a favorable location for slab detachment.

Examination of Figures 8.3c,d and 8.4c,d indicates that the style of 'crustal recycling' changes from mainly delamination, with very little or no convergence, to frequent break-off of the slab with somewhat larger subduction rates. This change is predominantly due to i) more extensive eclogitisation of the base of the crust, and ii) thinning of the strong mantle part of the lithosphere. Both effects are dependent on the total thermal thickness of the subducting plate, and thus on its age. Therefore, we expect this changing style to occur at higher mantle temperatures for older plates.

8.6   Conclusion

The Earth was probably warmer during the Archean and Proterozoic, although geological observations do not seem to provide a uniform answer to the question of the actual temperature drop until today, and values between 50 and 300 K have been suggested. An increased mantle temperature gave rise to a thicker basaltic oceanic crust and underlying harzburgitic layer, which probably increased the gravitational stability of the oceanic plate. This phenomenon has led to the idea that buoyant, low-angle subduction might have been more abundant than today, and subduction below a trenchward moving overriding continent, or lithospheric doubling, has been suggested as a mechanism to enable buoyant subduction. The uncertainty in the actual mantle temperature through time, and the associated increased buoyancy of the oceanic lithosphere contributes to the ongoing debate about the viability, effectiveness and presence of the modern plate tectonic mechanism in a younger Earth. We have conducted a series of numerical model calculations to quantify the viability of the subduction process for an Earth with a potential temperature in the range of 1300^oC to 1600^oC. As the basalt-to-eclogite transition in the crust probably plays an important role in the buoyancy of the oceanic plate and slab, and therefore also in its ability to subduct, the kinetics of this eclogitisation process is included in the numerical model by means of a simple parameterization, based on the ambient temperature and the Gibbs free energy of the two phases. The presented model results suggest that flat subduction below an overriding lithosphere can give rise to flat subduction up to a mantle temperature, which is not much higher (38 to 75 K) than today. A higher mantle temperature results in a mantle that is too weak to support the flat slab, and fast, steep Benioff subduction develops. For potential temperatures of 1450^oC or more, and extensive basalt metastability, subduction below an overriding plate does not occur at all, while again for lower transition temperatures, steep Benioff-type subduction occurs. In

a second set of experiments, we examined whether the modern-style subduction process, without an extra driving force, such as lithospheric doubling, could be a viable mechanism, when the mantle is hotter than today. In order to trigger the subduction process, we used again the mechanism of lithospheric doubling, which was switched off after 'active' subduction developed. Results show that for a potential temperature as high as 1450^oC, the subduction process essentially resembles the present-day situation. Subduction rates increase with increasing mantle temperature and decreasing transition temperature. For a 1525^oC potential temperature, considerable amounts of the dense eclogitic crust of the steeply descending slab delaminate from its mantle lithosphere, and sinks rapidly into the mantle. The remainder of the slab becomes more buoyant by this process, which essentially blocks the subduction process. At 1600^oC potential temperature, the mechanical coherence of the descending slab is reduced to such extent that frequent detachment of small pieces of the slab start to occur. The faster eclogitisation of the base of the 30-km thick crust allows for slow continuation of the 'subduction' process, until shallow slab detachment removes too much slab pull to allow for further convergence. The potential temperature at which the subducting plate only shows a marginal coherence, depends on the thickness of the plate at the trench, and therefore on its age. The results indicate that the eventual viability and 'mode' of the plate tectonic mechanism is determined by a complicated interaction between crustal thickness, eclogitisation rate, slab age, and the rheology of both crust and mantle.

Summary and Conclusions

The process of subduction is an essential feature of plate tectonics: where two plates converge, one of them, mostly an oceanic one, disappears into the mantle. An obvious driving mechanism for plate motion is gravitational instability of the cool and dense plates. The dense subducted part of the plate, the slab, exerts a pulling force on the attached plate at the surface. This 'slab pull' is regarded as the dominant contribution to plate motion. The stress orientation and steep dip angle of most slabs support this view. However, shallow, almost horizontal subduction, as occurring below Peru or Central Chile, does not fit into this simple picture, and has been puzzling geodynamicists since their discovery in the seventies. Also the subduction of mid-ocean ridges and young, and therefore buoyant and weak oceanic lithosphere requires alternative driving forces. These enigmas formed the motivation for this study. Several proposed mechanisms for flat or buoyant subduction are investigated by means of numerical modeling experiments using a thermo-chemical convection code. The physical background, and applied numerical techniques are described in Chapters 2 and 3, respectively.

Active trenchward motion of the overlying lithosphere can force young, and weak oceanic lithosphere to subduct without the presence of a significant slab and associated slab pull, and may lead to shallow flat subduction. In Chapter 4, the required physical circumstances for this process, coined lithospheric doubling (Vlaar, 1983), are examined. A weak, preexisting lithospheric fault that extends throughout most of the lithosphere, in combination with a lubricating 7-km-thick oceanic crust are required to continue the convergence during flat subduction, and to preserve of plate-like behavior of the weak subducting plate. A relatively strong mantle is necessary to fix the oceanic plate while being overridden, and to prevent the slab from descending more steeply through this mantle. Lithospheric doubling results in a forced descend of mantle material below the subducting plate through the major mantle phase transitions at 400 and 670 km depth. The contributions of the resultant latent heat effects on the process of shallow flat subduction are investigated in Chapter 5. In case of low-angle subduction of moderately young oceanic lithosphere, inclusion of the latent heat results in a significant increase of the flat slab length of 300-400 km. The effect from the 400-km phase transition is significantly larger than from the one at 670 km depth.

A proposed alternative mechanism for the occurrence of shallow flat slabs is the subduction of oceanic plateaus, aseismic ridges or seamount chains. These oceanic features all have a thickened crust (up to 35 km), and a proportionally thickened underlying harzburgitic layer, which give rise to an increased buoyancy of the subducting plate, as long as the basaltic crust does not transform into much denser eclogite. Chapter 6 deals with the physical circumstances for which a moderate oceanic plateau causes shallow flat subduction. Modeling results show that the amount of metastable basalt must be substantial to keep the plateau sufficiently buoyant. To allow for the necessary bending of the slab to the horizontal, the strength of the slab must be limited to about 600 MPa, and negative thermal buoyancy limits the slab age to about 60 Ma. The flat subduction below

Peru is most likely to be caused by both described mechanisms, since South America has a 3-cm/yr westward absolute plate motion with respect to the hotspot reference frame, and the subduction of the Nazca Ridge, an oceanic plateau with an 18-km-thick crust, occurs below Peru. In Chapter 7, the relative importance of both mechanisms is quantified. Results suggest a maximum average upper mantle viscosity of 3.5×10^{20} Pa s, and basalt metastability up to 600 to $800^{\circ}C$ to explain the observed slab geometry. Under these circumstances, the effect of the overriding lithosphere is estimated to be one to two times larger than the effect of the plateau subduction.

In Chapter 8, the viability of the present-day subduction processes in a younger, hotter Earth is quantified. An increased mantle temperature gave rise to more partial melting and resulted in a thicker oceanic crust, comparable to present-day oceanic plateaus. Flat buoyant subduction has therefore been suggested to have been more important in a younger Earth. Model results, however, suggest that already for a modest increase of the mantle temperature less than about 75 K, the mantle becomes too weak to support flat subduction. Nonetheless, forced subduction below an overriding plate, either flat or steep, could have been important in triggering the subduction process by favoring conditions for the onset of eclogitisation of the oceanic crust. For a potential temperature of at least 150 K higher than today, the modeling results suggest that modern-type Benioff subduction remains a viable tectonic process. For higher mantle temperature, the occurrence of crustal delamination or slab detachment prohibits a continuous subduction process.

This research has raised some unanswered questions that suggest further research. The compositional layering of the oceanic lithosphere was shown to be important for the dynamics of the subduction process. Both the rheology and the buoyancy of the crust differ significantly from those of the mantle lithosphere. By further refinement of this layering (inclusion of the sediment layer on top of the crust; grainsize variation throughout the crust), dynamical modeling could impose more constraints on the crustal rheology. At the moment, numerical resolution limitations prohibit such refinement. Improved quantification of the effects of hydration and deformation on the eclogitisation kinetics are necessary to obtain a better understanding of this process. Explicit modeling of (de)hydration of the oceanic crust and the mantle wedge (e.g. Iwamori, 1998) in combination with a dynamical subduction model could then provide improved dynamical constraints on these kinetics and associated slab buoyancy.

Extension of the plateau subduction in a three-dimensional model would enable modeling more complex subduction geometries with an along-trench mantle flow (Russo and Silver, 1994) and variation in the dip angle. It would provide a means to study a purely internally driven plateau subduction process and the modeling of the subduction of thicker and larger plateaus, such as the Ontong-Java plateau, which possibly collides with the trench and prohibits further subduction.

An important issue with respect to the subduction process in a hotter Earth is the dynamical effect of an harzburgitic asthenosphere, that, unlike the harzburgite in the overlying lithosphere, avoids subduction, and can eventually partly choke the formation of new crust at the ridge, and shut down regular subduction altogether. Under these circumstances, alternative scenario's of mantle recycling, which are not considered here, may become relevant.

Bibliography

Abbott, D., Drury, R., and Smith, W. H. F. (1994). Flat to steep transition in subduction style. *Geology*, 22:937–940.

Abers, G. A. (2000). Hydrated subducted crust at 100-250 km depth. *Earth Plan. Sci. Let.*, 176:323–330.

Ahrens, T. J. and Schubert, G. (1975). Gabbro-eclogite reaction rate and its geophysical significance. *Rev. of Geophysics and Space Physics*, 13(2):383–400.

Anderson, D. L. (1979). The upper mantle transition region: eclogite? *Geophys. Res. Let.*, 6(6):433–436.

Austrheim, H. (1998). Influence of fluid and deformation on metamorphism of the deep crust and consequences for the geodynamics of collision zones. In Hacker, B. and Liou, J., editors, *When continents collide: geodynamics and geochemistry of ultrahigh-pressure rocks*, pages 297–323. Kluwer academic publishers.

Bailey, R. C. (1999). Gravity-driven continental overflow and Archaean tectonics. *Nature*, 398:413–415.

Barazangi, M. and Isacks, B. L. (1976). Spacial distribution of earthquakes and subduction of the Nazca plate beneath South America. *Geology*, 4:686–692.

Barr, T. D. and Houseman, G. A. (1996). Deformation fields around a fault embedded in a non-linear ductile medium. *Geophys. J. Int.*, 125:473–490.

Becker, T. W., Facenna, C., O'Connell, R. J., and D., G. (1999). The development of slabs in the upper mantle: insights from numerical and laboratory experiments. *J. Geophys. Res.*, 104:15207–15226.

Benz, H. M. and Vidale, J. E. (1993). Sharpness of upper-mantle discontinuities determined from high-frequency reflections. *Nature*, 365:147–150.

Bickle, M. J. (1986). Implications of melting for stabilisation of the lithosphere and heat loss in the Archaean. *Earth Plan. Sci. Let.*, 80:314–324.

Bijwaard, H. and Spakman (2000). Non-linear global P-wave tomography by iterated linearized inversion. *Geophys. J. Int.*, 141:71–82.

Bijwaard, H., Spakman, W., and Engdahl, E. R. (1998). Closing the gap between regional and global travel time tomography. *J. Geophys. Res.*, 103:30055–30078.

Bina, C. and Helffrich, G. (1994). Phase transition Clapeyron slopes and transition zone seismic discontinuity topography. *J. Geophys. Res.*, 99(B8):15853–15860.

Bird, P. (1988). Formation of the rocky mountains, Western United States: A continuum computer model. *Science*, 239:1501–1507.

Bird, P. (1998). Kinematic history of the Laramide orogeny in latitudes 35°-49° N, western United States. *Tectonics*, 17(5):780–801.

Birdsall, C. K. and Langdon, A. B. (1991). *Plasma physics via computer simulation*. McGraw-Hill, Inc.

Blankenbach, B., Busse, F., Christensen, U., Cserepes, L., Gunkel, D., Hansen, U., Harder, H., Jarvis, G., Koch, M., Marquart, G., Moore, D., Olson, P., Schmeling, H., and Schnaubelt, T. (1989). A benchmark comparison for mantle convection codes. *Geophys. J. Int.*, 98:23–38.

Bos, B. and Spiers, C. J. (2001). Frictional-viscous flow of phyllosilicate-bearing fault rock: Microphysical model and implications for crustal strength. accepted for publication in *J. Geophys. Res.*, 2001.

Branlund, J. M., Regenauer-Lieb, K., and Yuen, D. A. (2001). Weak zone formation for initiating subduction from thermo-mechanical

feedback of low-temperature plasticity. *Earth Plan. Sci. Let.*, 190:237–250.

Brocher, T., Fuis, G. S. andFisher, M. A., Plafker, G., and Moses, M. J. (1994). Mapping the megathrust beneath the northern Gulf of Alaska using wide-angle seismic data. *J. Geophys. Res.*, 99:11663–11685.

Buiter, S. J. H. (2000). *Surface deformation resulting from subduction and slab detachment*. PhD thesis, Utrecht University, The Netherlands.

Caristan, Y. (1982). The transition from high-temperature creep to fracture in Maryland diabase. *J. Geophys. Res.*, 87:6781–6790.

Chapman, D. S. (1986). Thermal gradients in the continental crust. In Dawson, J. B., Carswell, D. A., , Hall, J., and Wedepohl, K. H., editors, *The Nature of the Lower Continental crust*, pages 63–70. Geological Society.

Christensen, U. R. (1996). The influence of trench migration on slab penetration into the lower mantle. *Earth Plan. Sci. Let.*, 140:27–39.

Christensen, U. R. (1998). Dynamic phase boundary topography by latent heat effects. *Earth Plan. Sci. Let.*, 154:295–306.

Christensen, U. R. and Hofmann, A. W. (1994). Segregation of subducted oceanic crust in the convecting mantle. *J. Geophys. Res.*, 99(B10):19867–19884.

Christensen, U. R. and Yuen, D. A. (1985). Layered convection induced by phase transitions. *J. Geophys. Res.*, 99:10291–10300.

Cloetingh, S. A. P. L., Wortel, M. J. R., and Vlaar, N. J. (1984). Passive margin evolution, initiation of subduction and the Wilson cycle. *Tectonophysics*, 109:147–163.

Cloos, M. (1993). Lithospheric buoyancy and collisional orogenesis: Subduction of oceanic plateaus, continental margins, island arcs, spreading ridges, and seamounts. *Geol. Soc. Am. Bull.*, 105:715–737.

Conrad, C. P. and Hager, B. H. (1999a). Effects of plate bending and fault strength at subduction zones on plate dynamics. *J. Geophys. Res.*, 104(B8):17551–17571.

Conrad, C. P. and Hager, B. H. (1999b). The thermal evolution of an earth with strong subduction zones. *Geophys. Res. Let.*, 26(19):3041–3044.

Conrad, C. P. and Hager, B. H. (2001). Mantle convection with strong subduction zones. *Geophys. J. Int.*, 144:271–288.

Cross, T. A. and Pilger, Jr, R. H. (1978). Tectonic controls of late Cretateous sedimentation, western interior, USA. *Nature*, 274:653–657.

Cross, T. A. and Pilger, Jr, R. H. (1982). Controls of subduction geometry, location of magmatic arcs, and tectonics of arc and back-arc regions. *Geol. Soc. Am. Bull.*, 93:545–562.

Crosson, R. S. and Owens, T. J. (1987). Slab geometry of the Cascadia subduction zone beneath Washington from earthquake hypocenters and teleseismic converted waves. *Geophys. Res. Let.*, 14(8):824–827.

Cuvelier, C., Segal, A., and van Steenhoven, A. A. (1986). *Finite element methods and Navier-Stokes equations*. D. Reidel Publishing Company, Dordrecht, The Netherlands.

Däßler, R., Yuen, D., Karato, S.-I., and Riedel, M. (1996). Two-dimensional thermo-kinetic model for the olivine-spinelphase transition in subducting slabs. *Phys. Earth Planet. Inter.*, 94:217–239.

Davies, G. F. (1992). On the emergence of plate tectonics. *Geology*, 20:963–966.

Davies, G. F. (1998). Plates, plumes, mantle convection and mantle evolution. In Jackson, I., editor, *The Earth's mantle: composition, structure and evolution*, pages 228–258. Cambridge University Press.

de Smet, J. H. (1999). *Evolution of the continental upper mantle: numerical modelling of thermo-chemical convection including partial melting*. PhD thesis, Utrecht University, The Netherlands.

de Smet, J. H., van den Berg, A. P., and Vlaar, N. J. (2000). Early formation and long-term stability of continents resulting from decompression melting in a convecting mantle. *Tectonophysics*, 322:19–33.

de Wit, M. J. (1998). On Archean granites,

greenstones, cratons and tectonics: does the evidence demand a verdict? *Precambrian Res.*, 91:181–226.

Defant, M. J. and Drummond, M. S. (1990). Derivation of some modern arc magmas by melting of young subducted lithosphere. *Nature*, 347:662–665.

Defant, M. J. and Drummond, M. S. (1993). Mount St. Helens: potential example of the partial melting of the subducted lithosphere in a volcanic arc. *Geology*, 21:547–550.

Dickinson, W. and Snyder, W. (1978). Plate tectonics of the Laramide orogeny. *Geol. Soc. Am. Mem.*, 151:355–366.

Doglioni, C. (1990). The global tectonic pattern. *Journal of geodynamics*, 12:21–38.

Drummond, M. S. and Defant, M. J. (1990). A model for trondhjemite-tonalite-dacite genesis and crustal growth via slab melting: Archean to modern comparisons. *J. Geophys. Res.*, 95:21503–21521.

Drury, M. R. and Fitz Gerald, J. D. (1998). Mantle rheology: insights from laboratory studies of deformation and phase transition. In Jackson, I., editor, *The Earth's mantle: composition, structure and evolution*, pages 503–559. Cambridge University Press.

Engebretson, D. C., Cox, A., and Gordon, R. G. (1985). Relative motions between oceanic and continental plates in the pacific basin. *The geological society of America, special paper*, 286:1–59.

England, P. and Bickle, M. (1984). Continental thermal and tectonic regimes during the Archaean. *Journal of Geology*, 92:353–367.

Fjeldskaar, W. (1994). Viscosity and thickness of the asthenosphere detected from the Fennoscandian uplift. *Earth Plan. Sci. Let.*, 126:399–410.

Forsyth, D. and Uyeda, S. (1975). On the relative importance of the driving forces of plate motion. *Geoph.J.R.Astron.Soc.*, 43:163–200.

Giunchi, C. and Ricard, Y. (1999). High-pressure/low-temperature metamorphism and the dynamics of an accretionary wedge. *Geophys. J. Int.*, 136:620–628.

Gordon, R. G. and Jurdy, D. M. (1986). Ceno-zoic global plate motions. *J. Geophys. Res.*, 91(B12):12389–12406.

Griffiths, R. W., Hackney, R. I., and van der Hilst, R. D. (1995). A laboratory investigation of effects of tranch migration on the descent of subducted slabs. *Earth Plan. Sci. Let.*, 133:1–17.

Gripp, A. E. and Gordon, R. G. (1990). Current plate velocities relative to the hotspot incorporating the Nuvel-1 global plate motion model. *Geophys. Res. Let.*, 17(8):1109–1112.

Gurnis, M. and Davies, G. F. (1986). Mixing in numerical models of mantle convection incorporating plate kinematics. *J. Geophys. Res.*, 91(B6):6375–6395.

Gutscher, M.-A. and Lallemand, S. (1999). Birth of a major strike-slip fault in SW Japan. *Terra Nova*, 11:203–209.

Gutscher, M.-A., Malavieille, J., Lallemand, S., and Collot, J.-Y. (1999a). Tectonic segmentation of the North Andean margin: impact of the Carnegie ridge collision. *Earth Plan. Sci. Let.*, 168:255–270.

Gutscher, M.-A., Maury, R., and J.P., E. (2000a). Can slab melting be caused by flat subduction? *Geology*, 28(6):535–538.

Gutscher, M.-A., Olivet, J.-L., Aslanian, D., Eissen, J.-P., and Maury, R. (1999b). The "lost Inca Plateau": cause of flat subduction beneath Peru? *Earth Plan. Sci. Let.*, 171:335–341.

Gutscher, M.-A., Spakman, W., Bijwaard, H., and Engdahl, E. (2000b). Geodynamics of flat subduction: Seismicity and tomographic constraints from the Andean margin. *Tectonics*, 19(5):814–833.

Hacker, B. R. (1996). Eclogite formation and the rheology, buoyancy, seismicity and H_2O content of oceanic crust. In *Subduction: Top to Bottom*, pages 337–346. AGU Monogr.

Hacker, B. R., Bohlen, S. R., and Kirby, S. H. (1993). albite $\rightarrow$ jadeite $+$ quartz transformation in albitite. *Eos, Trans. Am. Geoph. Union*, 74:611.

Hager, B. H. (1991). Mantle viscosity: a comparison of models from postglacial rebound and from the geoid, plate driving forces, and

advected heat flux. In Sabadini, R., editor, *Glacial isostasy, sea-level and mantle rheology*, pages 493–513. Kluwer Academic Publishers, The Netherlands.

Hamilton, W. B. (1998). Archean magmatism and deformation were not products of plate tectonics. *Precambrian Res.*, 91:143–179.

Han, L. and Gurnis, M. (1999). How valid are dynamic models of subduction and convection when plate motions are prescribed? *Phys. Earth Planet. Inter.*, 110:235–246.

Hasegawa, A. and Sacks, I. S. (1981). Subduction of the Nazca plate beneath Peru as determined from seismic observations. *J. Geophys. Res.*, 86(B6):4971–4980.

Herzberg, C. (1992). Depth and degree of melting of komatiites. *J. Geophys. Res.*, 97:4521–4540.

Hirahara, K. (1981). Three-dimensional seismic structure beneath southwest Japan: the subducting Philippine Sea plate. *Tectonophysics*, 79:1–44.

Hockney, R. W. and Eastwood, J. W. (1988). *Computer simulations using particles*. IOP Publishing Ltd, Bristol.

Hoffman, P. F. and Ranalli, G. (1988). Archean oceanic flake tectonics. *Geophys. Res. Let.*, 15:1077–1080.

Holland, T. J. B. (1980). The reaction albite = jadeite + quartz determined experimentally in the range $600\text{-}1200^o$ C. *Am. Mineralogist*, 65:129–134.

Houseman, G. A. and Gubbins, D. (1997). Deformation of subducted oceanic lithosphere. *Geophys. J. Int.*, 131:535–551.

Irifune, T. and Ringwood, A. E. (1993). Phase transformations in subducted oceanic crust and buoyancy relations at depths of 600-800 km in the mantle. *Earth Plan. Sci. Let.*, 117:101–110.

Ita, J. and King, S. D. (1994). Sensitivity of convection with an endothermic phase change to the form of governing equations, initial conditions, boundary conditions, and equation of state. *J. Geophys. Res.*, 99(B8):15919–15938.

Iwamori, I. (1998). Transportation of H_2O and melting in subduction zones. *Earth Plan. Sci. Let.*, 160:65–80.

Jarrard, R. D. (1986). Relations among subduction parameters. *Rev. of Geophysics*, 24(2):217–284.

Ji, S. and Zhao, P. (1994). Layered rheological structure of subducting oceanic lithosphere. *Earth Plan. Sci. Let.*, 124:75–94.

Jin, D., Karato, S.-I., and Obata, M. (1998). Mechanisms of shear localization in the continental lithosphere: inferences from the deformation microstructures of peridotites from the Ivrea zone, northwestern Italy. *J. Struct. Geol.*, 20(2/3):195–209.

Jischke, M. C. (1975). On the dynamics of descending lithospheric plates and slip zones. *J. Geophys. Res.*, 80(35):4809–4813.

Kameyama, M., Yuen, D. A., and Karato, S.-i. (1999). Thermal-mechanical effects of low-temperature plasticity (the Peierls mechanism) on the deformation of a viscoelastic shear zone. *Earth Plan. Sci. Let.*, 168:159–172.

Karato, S.-i. (1996). Phase transformations and rheological properties of mantle minerals. In Crossley, D. and Soward, A. M., editors, *Earth's deep interior*, pages 223–272. Gordon and Breach Sci. Pub.

Karato, S.-i. (1997). On the separation of crustal component from subducted oceanic lithosphere near the 660 km discontinuity. *Phys. Earth Planet. Inter.*, 99:103–111.

Karato, S.-i. (2001). Mapping water content in the upper mantle. Submitted to *Subduction Factory (AGU Monogr.)*.

Karato, S.-i. and Jung, H. (2001). Effects of pressure on high-temperature dislocation creep in olivine. Submitted to *Philosoph. Mag. A*.

Karato, S.-i., Riedel, M. R., and Yuen, D. A. (2001). Rheological structure and deformation of subducted slabs in the mantle transition zone: implications for mantle circulations and deep earthquakes. *Phys. Earth Planet. Inter.*, in press.

Karato, S.-i. and Rubie, D. C. (1997). Toward an experimental study of deep mantle rheology:

A new multianvil sample assembly for deformation studies under high pressures and temperatures. *J. Geophys. Res.*, 102(B9):21111–20122.

Karato, S.-i. and Wu, P. (1993). Rheology of the upper mantle: a synthesis. *Science*, 260:771–778.

Kincaid, C. and Sacks, I. S. (1997). Thermal and dynamical evolution of the upper mantle in subduction zones. *J. Geophys. Res.*, 102(B6):12295–12315.

King, S. D., Gable, C. W., and Weinstein, S. A. (1992). Models of convection-driven tectonic plates: a comparison of methods and results. *Geophys. J. Int.*, 109:481–487.

Kirby, S., Engdahl, E. R., and Denlinger, R. (1996a). Intermediate-depth intraslab earthquakes and arc volcanism as physical expressions of crustal and uppermost mantle metamorphism in subducting slabs. In *Subduction: Top to Bottom*, pages 195–214. AGU Monogr.

Kirby, S. H., Stein, S., Okal, E. A., and Rubie, D. C. (1996b). Metastable mantle phase transformations and deep earthquakes in subducting oceanic lithosphere. *Rev. of Geophysics*, 34(2):261–306.

Kirkpatrick, R. (1976). Towards a kinetic model for the crystallization of a magma body. *J. Geophys. Res.*, 81:2565–2571.

Kohlstedt, D. L., Evans, B., and Mackwell, S. J. (1995). Strength of the lithosphere: Constraints imposed by laboratory experiments. *J. Geophys. Res.*, 100(B9):17587–17602.

Kusky, T. M., Li, J.-H., and Tucker, R. D. (2001). The Archean Dongwanzi ophiolite complex, North China craton: 2.505-Billion-year-old oceanic crust and mantle. *Science*, 292:1142–1145.

Lambeck, K. and Johnston, P. (1998). The viscosity of the mantle: Evidence from analysis of glacial-rebound phenomena. In Jackson, I., editor, *The Earth's mantle: composition, structure and evolution*, pages 461–502. Cambridge University Press.

Lambeck, K., Smither, C., and Johnston, P. (1998). Sea-level change, glacial rebound and mantle viscosity for northern Europe. *Geophys. J. Int.*, 134:102–144.

Lenardic, A. and Kaula, W. M. (1994). Self-lubricated mantle convection: two-dimensional models. *Geophys. Res. Let.*, 21(16):1707–1710.

Mackwell, S. J., Zimmerman, M. E., and Kohlstedt, D. L. (1998). High-temperature deformation of dry diabase with application to tectonics on Venus. *J. Geophys. Res.*, 103(B1):975–984.

Malamud, B. D. and Turcotte, D. L. (1999). How many plumes are there? *Earth Plan. Sci. Let.*, 174:113–124.

McGeary, S., Nur, A., and Ben-Avraham, Z. (1985). Spacial gaps in arc volcanism: the effect of collision or subduction of oceanic plateaus. *Tectonophysics*, 119:195–221.

McKenzie, D. P. (1969). Speculations on the consequences and causes of plate motions. *Geoph.J.R.Astron.Soc.*, 18:1–32.

Mei, S. and Kohlstedt, D. L. (2000a). Influence of water on plastic deformation of olivine aggregates 1: Diffusion creep regime. *J. Geophys. Res.*, 105:21457–21469.

Mei, S. and Kohlstedt, D. L. (2000b). Influence of water on plastic deformation of olivine aggregates 2: Dislocation creep regime. *J. Geophys. Res.*, 105:21471–21481.

Meijer, P. T., Govers, R., and Wortel, M. J. R. (1997). Forces controlling the present-day state of stress in the Andes. *Earth Plan. Sci. Let.*, 148:157–170.

Moresi, L. and Gurnis, M. (1996). Constraints on the lateral strength of slabs from three-dimensional dynamic flow models. *Earth Plan. Sci. Let.*, 138:15–28.

Olbertz, D. (1997). *The long-term evolution of subduction zones: a modelling study*. PhD thesis, Utrecht University, The Netherlands.

Olbertz, D., Wortel, M. J. R., and Hansen, U. (1997). Trench migration and subduction zone geometry. *Geophys. Res. Let.*, 24:221–224.

Peacock, S. and Hyndman, R. (1999). Hydrous minerals in the mantle wedge and the maximum depth of subduction thrust earthquakes.

Geophys. Res. Let., 26:2517–2520.

Peacock, S. M. (1993). The importance of blueschist → eclogite dehydration reactions in subducting oceanic crust. *Geol. Soc. Am. Bull.*, 105:684–694.

Press, W. H., Teukolsky, S. A., Vetterling, W. T., and Flannery, B. P. (1992). *Numerical recipes in Fortran, The Art of Scientific Computing.* Cambridge University Press.

Putnis, A. (1992). *Introduction to mineral sciences*. Cambridge University Press.

Ranalli, G. (1987). *Rheology of the Earth, deformation and flow processes in geophysics and geodynamics*. Allen & Unwin.

Ranalli, G. (1998). Inferences on mantle rheology from creep laws. In *dynamics of the ice age earth: a modern perspective*, pages 323–340. Trans tech publications.

Riedel, M. R. and Karato, S. (1997). Grain-size evolution in subducted oceanic lithosphere associated with the olivine-spinel transformation and its effects on rheology. *Earth Plan. Sci. Let.*, 148:27–44.

Riedel, M. R. and Karato, S.-i. (1996). Microstructural development during nucleation and growth. *Geophys. J. Int.*, 125:397–414.

Ringwood, A. E. (1994). Role of the transition zone and 660 km discontinuity in mantle dynamics. *Phys. Earth Planet. Inter.*, 86:5–24.

Rubie, D. (1990). Role of kinetics in the formation and preservation of eclogites. In Carswell, editor, *Eclogite facies rocks*, pages 111–140. Blackie, Glasgow.

Rubie, D. C. and Ross II, C. R. (1994). Role of the transition zone and 660 km discontinuity in mantle dynamics. *Phys. Earth Planet. Inter.*, 86:223–241.

Rudnick, R. L., Barth, M., Horn, I., and McDonough, W. F. (2000). Rutile-bearing refractory eclogites: missing link between continents and depleted mantle. *Science*, 287:278–281.

Russo, R. M. and Silver, P. G. (1994). Trench-parallel flow beneath the Nazca plate from seismic anisotropy. *Science*, 263:1105–1111.

Sacks, I. S. (1983). The subduction of young lithosphere. *J. Geophys. Res.*, 88(B4):3355–3366.

Saunders, A., Tarney, J., Kerr, A., and Kent, R. (1996). The formation and fate of large oceanic igneous provinces. *Lithos*, 37:81–95.

Schmeling, H., Monz, R., and Rubie, D. C. (1999). The influence of olivine metastability on the dynamics of subduction. *Earth Plan. Sci. Let.*, 165:55–66.

Schott, B. and Schmeling, H. (1998). Delamination and detachment of a lithospheric root. *Tectonophysics*, 296:225–247.

Schott, B., Yuen, D. A., and Schmeling, H. (1999). Viscous heating in heterogeneous media as applied to the thermal interaction between crust and mantle. *Geophys. Res. Let.*, 26(4):513–516.

Segal, A. (1993). Finite element methods for advection-diffusion equations. In *Numerical methods for advection-diffusion problems*, pages 195–214. Vieweg & Sohn Verlagsgesellschaft mbH, Braunschweig.

Segal, A. and Praagman, N. P. (2000). The sepran package. Technical report, http://dutita0.twi.tudelft.nl/sepran/sepran.html.

Shelton, G. and Tullis, J. (1981). Experimental flow laws for crustal rocks. *Eos, Trans. Am. Geoph. Union*, 62(17):396.

Shepard, D. (1968). A two-dimensional interpolation function for irregularly-spaced data. *Proceedings of the 23rd National Conference. ACM, New York*, pages 517–524.

Sigmundsson, F. (1991). Post-glacial rebound and asthenosphere viscosity in Iceland. *Geophys. Res. Let.*, 18:1131–1134.

Smithies, R. H. (2000). The Archean tonalite-trondhjemite-granodiorite (ttg) series is not an analogue of cenozoic adakite. *Earth Plan. Sci. Let.*, 182:115–125.

Spencer, J. E. (1996). Uplift of the Colorado Plateau due to lithosphere attenuation during Laramide low-angle subduction. *J. Geophys. Res.*, 101(B6):13595–13609.

Steinbach, V. and Yuen, D. A. (1995). The effects of temperature-dependent viscosity on mantle convection with two major phase transitions. *Phys. Earth Planet. Inter.*, 90:13–36.

Stevenson, D. J. and Turner, S. J. (1977). Angle

of subduction. *Nature*, 270:334–336.

Stöckhert, B. and Renner, J. (1998). Rheology of crustal rocks at ultrahigh pressure. In Hacker, B. and Liou, J., editors, *When continents collide: geodynamics and geochemistry of ultrahigh-pressure rocks*, pages 57–95. Kluwer academic publishers.

Suarez, G., Monfret, T., Wittlinger, G., and David, C. (1990). Geometry of subduction and depth of seismogenic zone in the Guerrero gap, Mexico. *Nature*, 345:336–340.

Sung, C.-M. and Burns, R. G. (1976). Kinetics of the olivine-spinel transition: implications to deep-focus earthquake genesis. *Earth Plan. Sci. Let.*, 32:165–170.

Tackley, P. J., Stevenson, D. J., Glatzmaier, G. A., and Schubert, G. (1994). Effects of multiple phase transitions in a three-dimensional spherical model of convection in Earth's mantle. *J. Geophys. Res.*, 99(B8):15877–15901.

Tatsumi, Y. and Eggins, S. (1995). *Subduction zone magmatism*. Blackwell Science.

Toth, J. and Gurnis, M. (1998). Dynamics of subduction initiation at preexisting fault zones. *J. Geophys. Res.*, 103(B8):18053–18067.

Tovish, A., Schubert, G., and Luyendyk, B. P. (1978). Mantle flow pressure and the angle of subduction: non-newtonian corner flows. *J. Geophys. Res.*, 83(B12):5892–5898.

Trompert, R. and Hansen, U. (1998). Mantle convection simulations with rheologies that generate plate-like behaviour. *Nature*, 395:686–689.

Turcotte, D. L. and Schubert, G. (1982). *Geodynamics, Applications of continuum physics to geological problems*. John Wiley & Sons.

van den Berg, A. P., van Keken, P. E., and Yuen, D. A. (1993). The effects of a composite non-Newtonian and Newtonian rheology on mantle convection. *Geophys. J. Int.*, 115:62–78.

van den Berg, A. P. and Yuen, D. A. (1996). Is the lower-mantle rheology Newtonian today? *Geophys. Res. Let.*, 23(16):2033–2036.

van den Berg, A. P. and Yuen, D. A. (1998). Modelling planetary dynamics by using the temperature at the core-mantle boundary as a control variable: effects of rheological layering on mantle heat transport. *Phys. Earth Planet. Inter.*, 108:219–234.

van den Berg, A. P., Yuen, D. A., and van Keken, P. E. (1991). Effects of depth-variations in creep laws on the formation of plates in mantle dynamics. *Geophys. Res. Let.*, 18(12):2197–2200.

van den Beukel, J. and Wortel, R. (1988). Thermo-mechanical modeling of arc-trench regions. *Tectonophysics*, 154:177–193.

van der Hilst, R. (1995). Complex morphology of subducted lithosphere in the mantle beneath the Tonga trench. *Nature*, 374:154–157.

van der Hilst, R. and Mann, P. (1994). Tectonic implications of tomographic images of subducted lithosphere beneath northwestern South America. *Geology*, 22:451–454.

van der Hilst, R. and Seno, T. (1993). Effects of relative plate motion on the deep structure and penetration depth of slabs below Izu-Bonin and Mariana island arcs. *Earth Plan. Sci. Let.*, 120:395–407.

van der Lee, S. and Nolet, G. (1997). Seismic image of the subducted trailing fragments of the Farallon plate. *Nature*, 386:266–269.

van der Meulen, M. J., Kouwenhoven, T. J., van der Zwaan, G. J., Meulenkamp, J. E., and Wortel, M. J. R. (2000). Late Miocene uplift in the Romagnan Apennines and the detachment of subducted lithosphere. *Tectonophysics*, 315:315–331.

van Hunen, J., van den Berg, A. P., and Vlaar, N. J. (2000). A thermo-mechanical model of horizontal subduction below an overriding plate. *Earth Plan. Sci. Let.*, 182:157–169.

van Hunen, J., van den Berg, A. P., and Vlaar, N. J. (2001). Latent heat effects of the major mantle phase transitions on low-angle subduction. *Earth Plan. Sci. Let.*, 190:125–135.

van Keken, P. E. (1993). *Numerical Modelling of Thermochemically Driven Fluid Flow With Non-Newtonian Rheology*. PhD thesis, Utrecht University, The Netherlands.

van Keken, P. E., Karato, S., and Yuen, D. A.

(1996). Rheological control of oceanic crust separation in the transition zone. *Geophys. Res. Let.*, 23(14):1821–1824.

van Keken, P. E., King, S. D., Schmeling, H., Christensen, U. R., Neumeister, D., and Doin, M.-P. (1997). A comparison of methods for the modeling of thermochemical convection. *J. Geophys. Res.*, 102:22477–22495.

Vermeersen, L. L. A., Sabadini, R., Devoti, R., Luceri, V., Rutigliani, P., Sciarreta, C., and G., B. (1998). Mantle viscosity inferences from joint inversions of Pleistocene deglaciation-induced changes in geopotential with a new SLR analysis and polar wander. *Geophys. Res. Let.*, 25(23):4261–4264.

Vlaar, N. J. (1975). The driving mechanism of plate tectonics, a qualitative approach. In *Progress in Geodynamics*, pages 234–245, Amsterdam. North Holland Publ. Comp.

Vlaar, N. J. (1983). Thermal anomalies and magmatism due to lithospheric doubling and shifting. *Earth Plan. Sci. Let.*, 65:322.

Vlaar, N. J. (1986a). Archaean global dynamics. *Geologie en Mijnbouw*, pages 91–101.

Vlaar, N. J. (1986b). Geodynamic evolution since the Archaean. *Geophysics*, B89(4):387–406.

Vlaar, N. J. and Cloetingh, A. P. L. (1984). Orogeny and ophiolites: plate tectonics revisited with reference to the Alps. *Geologie en Mijnbouw*, 63:159–164.

Vlaar, N. J. and van den Berg, A. P. (1991). Continental evolution and archeao-sea-levels. In Sabadini, R., Lambeck, K., and Boschi, E., editors, *Glacial Isostasy, Sea-Level and Mantle Rheology*. Kluwer.

Vlaar, N. J., van Keken, P. E., and van den Berg, A. P. (1994). Cooling of the Earth in the Archaean: Consequences of pressure-release melting in a hotter mantle. *Earth Plan. Sci. Let.*, 121:1–18.

Vlaar, N. J. and Wortel, M. J. R. (1976). Lithospheric aging, instability and subduction. *Tectonophysics*, 32:331.

Vreugdenhil, C. B. (1989). *Computational hydraulics*. Springer-Verlag, Berlin.

Weinberg, R. F. and Schmeling, H. (1992). Polydiapirs: multiwavelength gravity structures. *J. Struct. Geol.*, 14:425–436.

Wortel, M. J. R., Remkes, M. J. N., Govers, R., Cloetingh, S. A. P. L., and Meijer, P. T. (1991). Dynamics of the lithosphere and the intraplate stress field. *Phil. Trans. R. Soc. Lond.*, 337:111–126.

Wortel, M. J. R. and Spakman, W. (1992). Structure and dynamics of subducted lithosphere in the Mediterranean region. *Proc. Kon. Ned. Akad. v. Wetensch.*, 95:325–347.

Wortel, M. J. R. and Spakman, W. (2000). Subduction and slab detachment in the Mediterranean-Carpathian region. *Science*, 290:1910–1917.

Wortel, M. J. R. and Vlaar, N. J. (1978). Age-dependent subduction of oceanic lithosphere beneath western South America. *Phys. Earth Planet. Inter.*, 17(3):201–208.

Yoshioka, S. and Wortel, M. J. R. (1995). 3-dimensional numerical modeling of detachment of subducted lithosphere. *J. Geophys. Res.*, 100:20223–20244.

Yuen, D. A., Fleitout, L., and Schubert, G. (1978). Shear deformation zones along major transform faults and subducting slabs. *Geoph.J.R.Astron.Soc.*, 54:93–119.

Zhong, S. and Gurnis, M. (1992). Viscous flow model of a subduction zone with a faulted lithosphere: long and short wavelength topography, gravity and geoid. *Geophys. Res. Let.*, 19(18):1891–1894.

Zhong, S. and Gurnis, M. (1994). Controls on trench topography from dynamic models of subducted slabs. *J. Geophys. Res.*, 99(B8):15683–15695.

Zhong, S. and Gurnis, M. (1995). Mantle convection with plates and mobile, faulted plate margins. *Science*, 267:838–843.

Zhong, S. and Gurnis, M. (1996). Interaction of weak faults and non-newtonian rheology produces plate tectonics in a 3D model of mantle flow. *Nature*, 383:245–247.

Zhong, S., Gurnis, M., and Moresi, L. (1998). Role of faults, nonlinear rheology, and viscosity structure in generating plates from instantaneous mantle flow models. *J. Geophys. Res.*, 103(B8):15255–15268.

Appendix A

The tracer method

A tracer method is developed to transport non-diffusive properties through the model domain in a time-dependent model. This method is applied to solve Equations 2.13 and 2.16. A large number of particles (or tracers) is initially emplaced with a uniform random spacial distribution in (a part of) the model domain. The particles are then advected with the flow field for each time step. Each tracer contains one or more properties, which are automatically advected with the flow. These properties can be constant in time or varying. Finite element solutions can be interpolated to the particles to update the value of the properties. Alternatively, interpolation of the particle properties to a finite element point can be performed, to calculate the coefficients of the equations to be solved with the finite element method.

A.1 Advection of particles

As each particle is individually advected with the flow, time integration of the conservation equation for composition does not involve the solution of a large system of unknowns simultaneously, but simply implies a time integration for each particle separately. In the predictor, an estimate of the new particle location is derived with a second-order Runge-Kutta time integration (Press et al., 1992):

$$k_1 = \Delta t \, \vec{v}(t, \vec{x}(t)) \tag{A.1}$$

$$k_2 = \Delta t \, \vec{v}(t + \frac{\Delta t}{2}, \vec{x}(t + \frac{\Delta t}{2})) \tag{A.2}$$

$$\approx \Delta t \, \vec{v}(t + \frac{\Delta t}{2}, \vec{x}(t) + \frac{\Delta t}{2}\vec{v}(t, \vec{x}(t)))$$

$$= \Delta t \, \vec{v}(t + \frac{\Delta t}{2}, \vec{x}(t) + \frac{k_1}{2})$$

$$\vec{x}(t + \Delta t) = \vec{x}(t) + k_2 \tag{A.3}$$

For each integration time value, the velocity field is interpolated from the finite element nodes to the required particle positions. As a prediction of the velocity field for time $t + \frac{\Delta t}{2}$ is not available, this is substituted by the velocity from time t. In the corrector step, the more accurate, but also more time-consuming fourth-order Runge-Kutta scheme is applied:

$$k_1 = \Delta t\, \vec{v}(t, \vec{x}(t)) \tag{A.4}$$

$$k_2 = \Delta t\, \vec{v}(t + \frac{\Delta t}{2}, \vec{x}(t) + \frac{k_1}{2}) \tag{A.5}$$

$$k_3 = \Delta t\, \vec{v}(t + \frac{\Delta t}{2}, \vec{x}(t) + \frac{k_2}{2}) \tag{A.6}$$

$$k_4 = \Delta t\, \vec{v}(t + \frac{\Delta t}{2}, \vec{x}(t) + k_3) \tag{A.7}$$

$$\vec{x}(t + \Delta t) = \vec{x}(t) + \frac{k_1}{6} + \frac{k_2}{3} + \frac{k_3}{3} + \frac{k_4}{6} \tag{A.8}$$

The velocity field at time $t + \frac{\Delta t}{2}$ is obtained by linear time interpolation of the finite element velocity field at times t and $t + \Delta t$ for each nodal point:

$$\vec{v_i}(t + \frac{\Delta t}{2}) = \left[\vec{v_i}(t) + \vec{v}_{Pi}(t + \Delta t) \right] / 2 \tag{A.9}$$

A.2   Interpolation to and from particles

Interpolation to the particles is always performed from the surrounding nodalpoints in the finite element mesh, using the finite element shape functions of the element in which the tracer particle is positioned. First the value of the shape functions ϕ_i at the interpolation point need to be determined. For the linear (sub)elements, this is performed with a straightforward linear interpolation. For the extended quadratic elements, used in the representation of the velocity field, the determination of the shape functions is performed for a general curvilinear element (Cuvelier et al., 1986): first a transformation of particle coordinates to the natural coordinates of the extended quadratic finite element is performed (i.e. a transformation to its coordinates in the unit triangle). In these natural coordinates, the values of the basis functions are easily calculated. The extended quadratic interpolation requires the function value in the 7th, barycentric point. Finally, the value f of the actual interpolation for both linear and extended quadratic interpolation is

$$f = \sum_{i=1}^{n} \phi_i f_i \tag{A.10}$$

where f_i are the nodal point values, and $n = 3$ or $n = 7$ in case of linear or extended quadratic interpolation, respectively.

For the interpolation from particles to the finite element gaussian or nodal points, two interpolation methods have been implemented: Shepard interpolation (Shepard, 1968) and Particle-In-Cell interpolation (Hockney and Eastwood, 1988; Birdsall and Langdon,
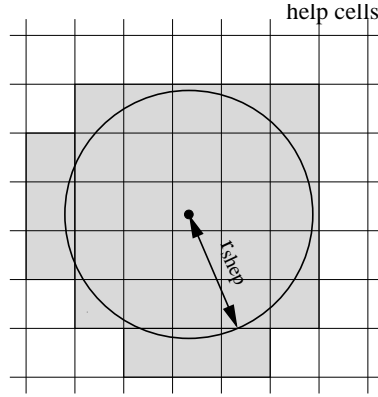
Figure A.1: *Particles from the help cells within a circle with Shepard radius r_{shep} from the interpolation point (grey shaded) are included in the Shepard interpolation. This reduces the computation time significantly in case of a large number of particles.*

1991). Both methods use a equidistant 'help cell grid', which subdivides the total tracer domain into a large number of approximately square areas, which are hereafter called help cells.

```
i = 1, n                        loop over particles
   j = 1, 4                     loop over surrounding grid points
      C_{J(j)} = C_{J(j)}
             +  C_i(Δx - x_J - x_i)(Δy - y_J - y_i)/(ΔxΔy)
      N_{J(j)} = N_{J(j)} + 1

   J = 1, K                     loop over all grid points
      C_J = C_J/N_J
```

Figure A.2: *Pseudo-code for the first step in the applied Particle-In-Cell algorithm*

The Shepard interpolation (Shepard, 1968) has an inverse-distance weighted approach and interpolation of a set of n particles is defined as:

$$C(\vec{x}) = \frac{\sum_{i=1}^{n} \frac{C_i}{r_i^2}}{\sum_{i=1}^{n} \frac{1}{r_i^2}} \tag{A.11}$$

where r_i is the distance from the position of particle i to evaluation point $\vec{x}$ and C_i the function value of particle i. In practice, distant tracers have a negligible influence on the value of $C(\vec{x})$. Therefore, it is not necessary to include particles, further away than

some radius around the interpolation point (which is called the Shepard radius r_{shep}) in the interpolation. To avoid the calculation of the distance between all particles and the interpolation point, only the particles from the help cells that lie (partly) within the Shepard radius) are used for the interpolation. This is visualized in Figure A.1.

The Particle-In-Cell (PIC) interpolation has a two-step interpolation scheme. First, bilinear weighting factors are used to interpolate from each particle to the four grid points of the help cell in which the tracer is positioned (Birdsall and Langdon, 1991). Grid points values are obtained by dividing the sum of contributions of all particles to a grid point by the number of contributions. A pseudo-code description of the algorithm is given in Figure A.2. The interpolation is also called area-weighted interpolation, due to its geometric interpretation (Birdsall and Langdon, 1991), as visualized in Figure A.3a. Second, a bilinear interpolation value f_{int} is obtained for a finite element nodal point or
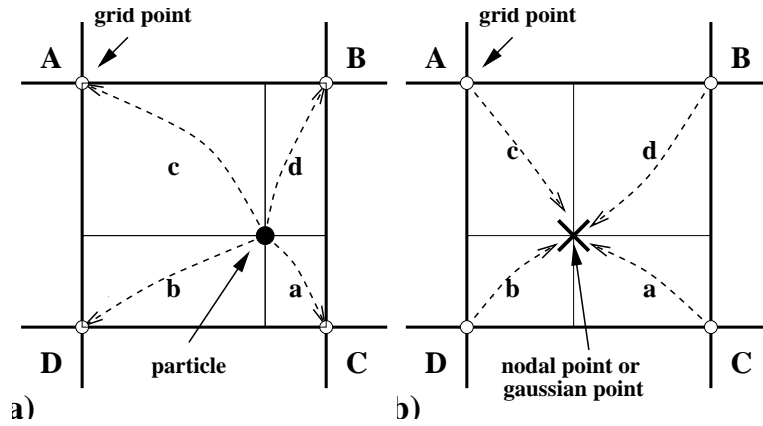

Figure A.3: *Visualization of both steps in the Particle-In-Cell interpolation, which use a bilinear weighting or area-weighting: a) the particle value is first distributed over grid points A, B, C and D with a weighting factor proportional to the areas a, b, c and d, respectively. b) Then, a second interpolation from the grid points to point X is performed, where again the concept of area weighting is applied.*

gaussian point at (x, y) from the four surrounding grid points A, B, C, and D:

$$
\begin{aligned}
f_{int} &= \left[(x_C - x)(y_C - y)f_A + (x - x_D)(y - y_D)f_B + \right. \\
&\quad \left. (x - x_A)(y_A - y)f_C + (x_B - x)(y_B - y)f_D \right] / (\Delta x \Delta y) \\
&= \left[a f_A + b f_B + c f_C + d f_D \right] / (\Delta x \Delta y)
\end{aligned}
\tag{A.12}
$$

where a, b, c and d are defined in Figure A.3b.

Samenvatting (Summary in Dutch)

Een essentieel onderdeel bij de beweging van de aardschollen, ook wel plaattectoniek genaamd, is subductie: waar twee platen samenkomen zal een van de twee onder de ander in de mantel verdwijnen. In het algemeen wordt dit subductieproces grotendeels aangedreven door het reeds gesubduceerde koude en zware deel van de plaat, dat in de mantel zakt en de rest van de plaat mee trekt. Dit proces wordt 'slab pull' genoemd. Toch geeft subductie bij Peru en Chili in Zuid Amerika aan, dat het proces iets ingewikkelder in elkaar steekt: het gesubduceerde deel van de oceanische Nazca plaat beweegt daar enkele honderden kilometers horizontaal, vlak onder het Zuid-Amerikaanse continent door, voordat het dieper de mantel inzakt. Ook komt subductie van gravitationeel stabiele lithosfeer van slechts enkele miljoenen jaren oud voor, waarbij 'slab pull' een minimale rol speelt. Diverse mechanismen voor ondiepe horizontale of jonge subductie zijn al voorgesteld, en enkelen daarvan zijn onderzocht in dit proefschrift met een numeriek thermo-chemisch convectie model. De fysica en numerieke aspecten daarvan zijn beschreven in hoofdstukken 2 en 3.

Een van deze voorgestelde mechanismen is lithosfeerverdubbeling, waarbij een oceanische, subducerende plaat actief wordt overreden door de niet-subducerende, continentale plaat. De beweging van het continent in de richting van de oceaan maakt subductie mogelijk zonder overige aandrijving. Dit proces is onderzocht in hoofdstuk 4, waarin gekeken wordt naar de fysische omstandigheden, waarin dit proces mogelijk is. Een van de voorwaarden blijkt een goede ontkoppeling van de naar elkaar toe bewegende platen door middel van een grootschalig breuken-systeem tussen de platen. Ook moet de (meestal ongeveer zeven kilometer dikke) oceanische korst vrij zacht zijn om de plaatconvergentie te smeren. De mantel onder de platen moet daarentegen vrij sterk zijn om een reactiekracht voor een overrijdende continent te kunnen verzorgen, en het snel zinken van de subducerende plaat te voorkomen. Lithosfeerverdubbeling dwingt mantelmateriaal onder de subductiezone door de vaste-stof faseovergangen op 400 en 670 km diepte. De resulterende latente warmte is van invloed op de dynamica van de horizontaal subducerende plaat erboven. Het remt het neergaande mantelmateriaal af en bevordert hiermee ondiepe subductie. Hoofdstuk 5 laat zien, dat het opnemen van latente warmte in het numerieke model een 300-400 km langere horizontale subductie tot gevolg kan hebben, en

123

dat het effect van de ondiepe faseovergang op 400 km diepte veel groter is dan die op 670 km diepte.

Een voorgesteld alternatief mechanisme is de subductie van zogenaamde oceanische plateaus. Deze plateaus zijn enkele honderden kilometers breed en lang, onderdeel van de oceanische lithosfeer, en bevatten een korst en onderliggende harzburgietlaag, die wel twee tot drie maal zo dik zijn als die van een normale oceanische lithosfeer. Hierdoor wordt de plaat veel lichter, zodat deze niet in de mantel wil zinken. Een voorwaarde bij dit model is dat het lichte korstmateriaal (basalt) niet al te snel via een faseovergang omgezet wordt in het veel zwaardere eclogiet gedurende subductie. In hoofdstuk 6 worden de benodigde fysische omstandigheden voor dit mechanisme bekeken. Een flinke vertraging in de omzetting van basalt naar eclogiet, een sterkte van de subducerende plaat van 600 MPa of minder, en een leeftijd van de plaat op het moment van subductie van minder dan 60 miljoen jaar blijken de voorwaarden te zijn om met dit mechanisme een plaat horizontaal over enkele honderden kilometers ondiep te kunnen laten subduceren. De horizontale subductie onder Peru is waarschijnlijk het effect van beide hierboven beschreven mechanismen: hier subduceert namelijk de Nazca Rug met een korstdikte van ongeveer 18 km onder het Zuid-Amerikaanse continent, welke op zijn beurt met 3 cm per jaar actief naar het westen, dus richting de oceaan beweegt. In hoofdstuk 7 is de relatieve bijdrage van beide mechanismen onderzocht. Een maximale bovenmantel viscositeit van 3.5×10^{20} Pa s en een vertraging van de eclogietvorming bij temperatuur-waarden onder 600 tot 800°C lijken noodzakelijk om de observaties te kunnen verklaren. Onder deze omstandigheden is het effect van lithosfeerverdubbeling één tot twee maal zo belangrijk als die van het subducerende plateau.

Tenslotte is in hoofdstuk 8 het hedendaagse subductieproces in een model van de vroegere aarde bekeken. Een hetere mantel veroorzaakte toen meer partieel smelten van mantelmateriaal, en resulteerde waarschijnlijk in een dikkere korst, vergelijkbaar met de huidige oceanische plateaus. Ondiepe horizontale subductie is daarom al eerder voorgesteld als dominante vorm van subductie in de vroege aarde. Modelberekeningen laten echter zien, dat voor een slechts bescheiden toename van de manteltemperatuur de mantel al te zacht wordt om ondiepe horizontale subductie te kunnen ondersteunen. Desalniettemin kan geforceerde subductie zoals voorgesteld voor lithosfeerverdubbeling een belangrijke rol hebben gespeeld bij de aanzet van subductie, omdat het eclogietvorming bevordert. Modelresultaten laten zien, dat het hedendaagse subductie proces mogelijk blijkt tot een mantel temperatuur van minstens 150 graden warmer dan tegenwoordig. Voor hogere manteltemperaturen verhinderen korst-delaminatie en het afbreken van de subducerende delen van de plaat de continuïteit van het subductieproces. Deze resultaten illustreren dat extrapolatie van het huidige proces van grootschalige plaattectoniek en bijbehorende lithosfeer subductie niet zondermeer kunnen worden geëxtrapoleerd naar een hetere jongere aarde.

Dankwoord (Acknowledgments)

Vele mensen hebben bijgedragen aan de totstandkoming van dit proefschrift, en ik zou graag een aantal van hen willen bedanken. Mijn promotor Prof.Dr. Vlaar ben ik zeer erkentelijk voor het opzetten van het project, dat voortbouwt op zijn vroegere werk op het terrein van de manteldynamica, en lithosfeerverdubbeling in het bijzonder. Zijn vele goede ideeën en zijn ruime wetenschappelijke ervaring maakte het ook mogelijk het project in een breder kader te plaatsen. Het onderzoek had veel baat bij de vele discussies met hem, die er verder ook toe hebben geleid, dat niet elk van mijn antwoorden meer met 'ja maar ...' begint. Daarnaast gaat mijn dank in de eerste plaats uit naar mijn co-promotor en directe begeleider Dr. Arie van den Berg. Niet alleen tijdens het promotieproject, maar ook al ruim daarvoor was het altijd zeer prettig om met hem samen te werken. Zijn grote betrokkenheid was zeer welkom en zijn enthousiasme werkte aanstekelijk. Daarnaast was hij op persoonlijk vlak ook altijd erg aangenaam gezelschap. Ik denk, dat zonder zijn ervaring, goede adviezen en begeleiding dit project heel anders zou zijn verlopen.

Prof.Dr. David Yuen is thanked for his everlasting enthousiasm, support and many literature hints, for a pleasant stay in Minneapolis, including the necessary computer resources and beers. Due to him the world of geophysicists seems to be much smaller.

Vele collega's hebben bijgedragen tot een goede werksfeer en de voortgang van het onderzoek. Ik wil Stan Schoofs heel hartelijk bedanken voor de vele steun tijdens mijn gevechten met het numerieke model, de zeer nuttige thesaurus die hij me ooit kado gaf, en de vele gezellige koffieuurtjes. Mijn (ex-)kamergenoot Jeroen de Smet zorgde altijd voor een aangename sfeer en een hoop werkplezier, en vele practische tips. Bedankt hiervoor. De samenwerking met Hana Čížková heb ik als zeer nuttig en leerzaam, maar bovenal als erg gezellig ervaren. Bertram Schott wil ik bedanken voor alle adviezen en suggesties in verband met het project, en voor de vele nuttige en nutteloze, maar altijd amusante gesprekken. Peter van Thienen en Gualbert Oude Essink wil ik bedanken voor hun gezelligheid en nuchtere kijk op veel zaken. Jan ter Heege, Bart Bos, Hans de Bresser, Chris Spiers, Arjen Dijkstra, Rob McDonnel, Martin Drury en Herman van Roermund wil ik bedanken, niet alleen voor de overload aan rheologische informatie, maar ook voor hun vrolijke aanwezigheid. Bernard de Jong (nogmaals bedankt voor de 'elements of style'), Volker Steinbach en Michel Jacobs wil ik bedanken voor hun diverse wetenschappelijke bijdragen, prettige samenwerking en alle lege bierflesjes. Rob van der Hilst en Bertram Schott wil graag ik bedanken voor hun nuttige correcties en suggesties bij enkele hoofdstukken in dit proefschrift.

Goede technische ondersteuning is onontbeerlijk gebleken en gelukkig heb ik daarover nauwelijks te klagen gehad. Joop Hoofd en Theo van Zessen wil ik heel hartelijk bedanken voor hun vele kostbare uren computerondersteuning, die ze me hebben laten roven. Rob Govers en Wim Spakman hebben veel problemen met het zo dankbaar gebruikte plotprogramma P weggenomen. Bovendien wil ik Rob bedanken voor de nuttige discussies en Wim voor de plot in hoofdstuk 1. Paul van Oudenallen was altijd even behulpzaam bij het printen van posters en andere grafische zaken, en Jesper Spetzler heeft me uit de brand geholpen bij het creëren van PDF's. De mensen bij SARA en metname Ron Trompert wil ik bedanken voor hun hulp bij het gebruik van hun computersystemen. Jan Jansen was altijd bijzonder behulpzaam tijdens mijn speurtochten door de bibliotheek. Tenslotte gaat speciale dank uit naar Guus Segal, allereerst voor de ontwikkeling van zijn software pakket SEPRAN, maar ook voor de snelle aanpassingen op verzoek en geboden hulp in het gebruik.

Verder hebben een groot aantal andere mensen erg bijgedragen tot een aangename werksfeer: Susanne Buiter, Marleen Nyst, Antonio Villaseñor, Edith Hafkenscheid, Menno van der Zedde, Paul Meijer, Harmen Bijwaard, Eugenio Carminati, Ildiko Csikos, Rinus Wortel, Annemarie Bos, Anne Bonis, Hayfaa Abdul Aziz, Joris Steenbrink, Siese de Meer, Arthur Schmidt, Andor Lips, Jan-berend Stuut, Hanneke Paulssen, Stephanie Godey, Caroline Beghein, Frederic Deschamps, Renate Hartog, Arie van Wettum, Rob Devilee, Kabir Roy-Chowdhury, Henk van der Meer, en de mensen op het fort: allemaal erg bedankt voor gezelligheid, wetenschappelijke en niet-wetenschappelijke discussies, en collegialiteit.

Gelukkig bestond mijn leven niet helemaal uit werken en heb ik veel plezier en steun gehad van familie en vrienden. Mijn ouders hebben me altijd volledig gesteund en aangemoedigd, op school, tijdens m'n studie, en zo ook tijdens dit project. Ik ben ze daarvoor enorm dankbaar. Ook de grote belangstelling van mijn opa heeft me altijd erg gestimuleerd. Verder wil ik Yvette en Michel, de rest van mijn familie en mijn schoonfamilie heel hartelijk bedanken voor alle interesse en steun. Jelle en Huub: hoe anders waren zaken gelopen, als Jimi Hendrix nooit had bestaan? Stan: blijf nog maar een tijdje om de hoek wonen. John: bedankt voor zo'n 15 jaar Rotterdams klaverjassen, enzo. Verder iedereen bedankt die mij menig aangenaam uurtje heeft bezorgd tijdens en na de wekelijkse partij basketbal, op de autosloperij, of gewoon thuis aan de wijn of port. Lieve Abir, heel hartelijk bedankt voor alle liefde, vrolijkheid en steun. Zonder jou was dit boekje er nooit gekomen.

Curriculum Vitae

Jeroen van Hunen werd geboren op 27 mei 1971 te Rotterdam. Hij volgde een middelbare school opleiding aan het het Marnix Gymnasium te Rotterdam, en behaalde daar het einddiploma in 1990. In datzelfde jaar begon hij aan een studie natuurkunde aan de universiteit Utrecht, maar besloot al snel, dat geofysica toch meer in zijn richting lag. Het afstudeeronderzoek betrof een numerieke modelstudie van smelt segregatie bij mid-oceanische ruggen. Het eindexamen geofysica werd behaald op 26 augustus 1996. Na een korte aanstelling als toegevoegd onderzoeker begon hij op 1 februari 1997 als assistent in opleiding (aio) aan een promotieonderzoek, waarvan dit proefschrift het resultaat is.